UiT
THE ARCTIC
UNIVERSITY
OF NORWAY

Faculty of Science and Technology

Department of Physics and Technology

Radar studies of plasma parameters in the polar cap and the auroral zone

—

Lindis Merete Bjoland

A dissertation for the degree of Philosophiae Doctor – January 2018

Abstract

This dissertation focuses on variations of plasma parameters in the polar cap and auroral zone ionosphere. Changes on long time scales, connected to the anthropogenic emissions of greenhouse gases, and on shorter time scales due to diurnal, seasonal and solar cycle variations are investigated, and the performance of the International Reference Ionosphere (IRI) model in reproducing the observed variations in the plasma parameters has been evaluated.

To do this investigation, we have used the accumulated dataset of ionospheric parameters from the **E**uropean **I**ncoherent **Scat**ter (EISCAT) radar system. This radar system consists of a monostatic UHF and a tristatic VHF radar located near Tromsø at geographic coordinates 69.58° N, 19.23° E and a third radar located at Svalbard at geographic coordinates 78.15° N, 16.02° E. The UHF radar started its operations in 1981, and the **E**ISCAT **S**valbard **R**adar (ESR) was inaugurated in 1996. This means that the EISCAT data cover more than one solar cycle in the polar cap and several solar cycles in the auroral zone. Information about electron density, ion and electron temperature and line-of-sight velocity can be obtained from the incoherent scatter spectrum, and many other plasma parameters can be derived.

This dissertation consists of three papers. In paper I (*Bjoland et al.*, 2016), we use data from the ESR and investigate how well the IRI model is able to reproduce the polar cap electron density as it varies with season, time of day, and solar cycle. In paper II (*Bjoland et al.*, 2017a) we derive the Hall conductivity using electron density data and search for trends in the peak height of the Hall conductivity and in the E-region ion temperature. In paper III (*Bjoland et al.*, 2017b), we focus on high-latitude depletion regions and investigate the dependence on geomagnetic activity.

The main results of this dissertation can be summarized as follows:

- In general, the IRI model is biased towards an underestimation of the F-region polar cap electron density. This underestimation is stronger at nighttime and during solar maximum. At altitudes around the peak height of the F-region, the agreement between the IRI model and the ESR electron density is better than at higher and lower altitudes (*Bjoland et al.*, 2016). The diurnal variations of the ion temperature, seen in the ESR data, are not as clear in the IRI model data (*Bjoland et al.*, 2017b).

- The Hall conductivity and its peak height show strong seasonal variations. At 110 km altitude, the difference between the Hall conductivity during summer and winter was shown to be approximately $2 \cdot 10^{-4}$S/m. For the peak height, the difference between summer and winter was approximately 6 km (*Bjoland et al.*, 2017a).

- No conclusive long-term trends were found in the peak height of the conductivity or in the ion temperature at 110 km altitude. In the peak height of the conductivity a very weak descent of -0.18±0.20 km/decade was seen, but this is within the error bars of the peak height. The ion temperature shows a cooling trend of -1.00±0.59 K/year. However, a better understanding of the observed ion temperature variations must be achieved before a conclusive trend can be obtained (*Bjoland et al.*, 2017a).

- A depletion region can be observed early morning in the ESR electron density data. This region expands with increasing geomagnetic activity. ESR ion temperature measurements show a heating at approximately the same time as the depletion region, suggesting that this depletion region might be connected to ion frictional heating (*Bjoland et al.*, 2017b).

- The IRI model is not able to reproduce the early morning depletion region observed in the F-region polar cap ionosphere (*Bjoland et al.*, 2017b).

Acknowledgements

I started my work as a PhD student at the University in Tromsø (UiT) in November 2012. The 5 years I have spent working on my dissertation have been extremely rewarding. I have learned a lot, not only about the ionosphere and incoherent scattering, but also personally. Through these years I have had many experiences which have left me with good memories. I have participated and presented my research at several conferences both nationally and internationally, which gave me the opportunity to have fruitful discussions with colleagues from all over the world. In total, I stayed over a year in Japan as a visiting student at the National Institute of Polar Research (NIPR) working on my dissertation. I have also been fortunate to be a student member of an International Space Science Institute (ISSI) team that is working on Climate Change in the Upper Atmosphere. As a PhD student I have met numerous people to whom I feel grateful for, who shared their experiences with me and encouraged me, and only a few of them will be named here.

First of all, I would like to thank my supervisors in Tromsø, Unni Pia Løvhaug and Cesar La Hoz for their guidance and support. I feel very lucky to have them as my supervisors as they have long experience in working with incoherent scattering in general and EISCAT data in particular. I truly appreciate all our discussions. I would especially like to thank Unni for all the encouragement and advice I have received during the final stage of my PhD. Thank you for reading the draft of my dissertation and discussing it with me. Then, I would like to thank Cesar for introducing me to several researchers in Ukraine, Japan and elsewhere, and for encouraging me to participate in international collaborations.

Acknowledgements

Part of my time as a PhD student was spent as a visiting student at NIPR in Japan. My first stay was funded by UiT and lasted for approximately 10 months starting in 2015. I would like to thank Hiroshi Miyaoka for inviting me and organizing my stay at NIPR. In 2017 I got the opportunity to return to Japan and stay there for 3 months starting in January. This time my stay was funded by NIPR as part of their internship program. I would like to thank students and staff at NIPR for their great hospitality, their support and for the discussions we had during my visits to Japan.

During both of my stays in Japan, Yasunobu Ogawa acted as my supervisor. I am tremendously grateful for all his help, guidance and advice. Not only during my stays at NIPR, but also after I returned to Tromsø he continued to give me his advice by e-mail, and we met to discuss several times when he visited the EISCAT site in Ramfjordmoen. Yasunobu Ogawa has many years of experience in working with long time-series of EISCAT data, and willingly shared this experience with me. His ideas and suggestions have been invaluable for this dissertation.

Furthermore, I would like to thank my fellow PhD students and the rest of the Space Physics group at UiT for providing such a supportive and inclusive environment, both socially and academically. Thank you to Henry Pinedo for his help and support and for being so welcoming when I first arrived in Tromsø. Vasyl Belyey gave me a lot of helpful advice during the first stage of my PhD project, of which I am very grateful. Njål Gulbrandsen takes amazing photographs and allowed me to use one of them for the front page of my dissertation. Another of his photos is found in chapter 3. Thanks to Njål for letting me use his photos. I would also like to thank Njål for letting me use his LaTeX code for my dissertation, and for helping me setting it up.

Finally, I would like to thank my family and friends for their support.

Lindis Merete Bjoland
Tromsø, 2018

Contents

Chapter 1

Introduction

The growing technological use of space makes it important to have a good knowledge of the physical processes and phenomena of the ionosphere. Services which include Earth observation, weather monitoring, navigation and communication makes it necessary to understand the variations of these processes on various time scales. Studies of ionospheric phenomena with short- and medium time-scales, such as plasma irregularities and space weather, have been published frequently in the last decades. Variations on longer time-scales, however, are less studied, as is also the case for very short time-scale phenomena. The planned EISCAT_3D radar is expected to lead to new insights on variations on the shortest time-scales by providing measurements with a time resolution beyond the present resolution of incoherent scatter radars of today. Studies on long-term variations and trends have in the recent years gained increasing focus and interest among scientists as it has been found that the increased emissions of climate gases lead to changes in the ionosphere (*Roble and Dickinson*, 1989). By now, incoherent scatter radars have been operational for several decades and it is therefore possible to use the accumulated databases of radar data to search for such features in the ionosphere. A good understanding of the natural variations that occur is necessary in order to reveal possible trends in the ionosphere which could be connected to global climate change.

The polar ionosphere is a dynamic region, strongly connected to the outer magnetosphere through the magnetic field lines. This connection makes the polar ionosphere prone to rapid changes controlled by transient changes in the solar wind and the interplanetary magnetic field. Particle precipitation, plasma convection, Joule heating, transient plasma flow events and plasma depletion are all examples of phenomena that are affected by the magnetosphere-ionosphere coupling. Such variations on short time scales makes the polar ionosphere notoriously difficult for models to reproduce. The ionosphere also changes on longer time-scales. Long-term changes in the ionosphere can be of natural origin such as long-term changes in the Earth's magnetic field or in solar activity, but it has also been proven that the ionosphere and upper atmosphere is changing as a result of anthropogenic emissions of climate gases (*Laštovička et al.*, 2006).

One of the most powerful tools to study the polar ionosphere is the incoherent scatter radar. Incoherent scatter radars have the capability to obtain information about several plasma parameters from a wide range of altitudes. Three of the radars located at polar latitudes are operated by the European Incoherent Scatter (EISCAT) Association. These consist of an UHF and a VHF system located outside Tromsø in the auroral zone, and a 500 MHz radar located on Svalbard covering the polar cap and cusp region. The Tromsø UHF radar is the oldest of the three EISCAT radars and started its operations in 1981, while the youngest system, the EISCAT Svalbard radar (ESR), made its first measurements in 1996. As a concequence, the available database of EISCAT measurements now cover more than one solar cycle in the polar cap and cusp, and several solar cycles in the auroral zone. These long time series of EISCAT data are useful for studying trends and long-term variations in the high-latitude ionosphere.

As the EISCAT radars by now have been operational for several decades, the accumulated database may be used to achieve a comprehensive view of the polar ionosphere. Part of the motivation behind this PhD project is to utilize the possibilities this unique data set gives us to study how the polar ionosphere changes both on short and long time scales, and how well the International Reference Ionosphere (IRI) model, the most widely used ionospheric model, is able to

reproduce these changes. This dissertation consists of three papers which all are connected to changes in the polar ionosphere. In these papers, we try to answer the following three key questions:

- How well does the IRI model reproduce diurnal, seasonal, solar and geomagnetic activity variations in the polar ionosphere? (Paper I and paper III)
- Is it possible to observe long-term trends connected to the anthropogenic emissions of climate gases in the E-region EISCAT data? (Paper II)
- How are high-latitude depletion regions affected by the level of geomagnetic activity? (Paper III)

1.1 List of papers

The following papers are included in this dissertation:

I Bjoland, L. M., V. Belyey, U.P. Løvhaug and C. La Hoz: An evaluation of International Reference Ionosphere electron density in the polar cap and cusp using EISCAT Svalbard radar measurements, Ann. Geophys., 34, 751-758, https://doi.org/10.5194/angeo-34-751-2016, 2016.

II Bjoland, L.M., Y. Ogawa, C. Hall, M. Rietveld, U.P. Løvhaug, C. La Hoz, H. Miyaoka, Long-term variations and trends in the polar E-region, J. Atmos. Sol. Terr. Phys., 163 , 85-89, ISSN 1364-6826, https://doi.org/10.1016/j.jastp.2017.02.007, 2017.

III Bjoland, L.M., Y. Ogawa, U.P. Løvhaug, High-latitude depletion regions and their dependence on geomagnetic activity, submitted to Journal of Geophys. Res. Space, 2017,

In addition, I have also contributed to the following papers not included in this dissertation:

A Vickers, H., M. J. Kosch, E. Sutton, L. Bjoland, Y. Ogawa, and C. La Hoz, A solar cycle of upper thermosphere density observations from the EISCAT Svalbard Radar, J. Geophys. Res. Space Physics, 119, 6833–6845, doi:10.1002/2014JA019885., 2014.

B Bjoland, L. M., X. Chen, Y. Jin, A. S. Reimer, Å. Skjæveland, M. R. Wessel, J. K. Burchill, L. B. N. Clausen, S. E. Haaland and K. A. McWilliams, Interplanetary magnetic field and solar cycle dependence of Northern Hemisphere F region joule heating. J. Geophys. Res. Space Physics, 120: 1478–1487. doi: 10.1002/2014JA020586, 2015.

1.2 Dissertation outline

The aim of chapter 2 is to give a brief, general introduction to the polar ionosphere and the phenomena which occur there. This chapter is based on introductory textbooks in space physics such as *Baumjohann and Treumann* (1996), *Brekke* (2013), *Hunsucker and Hargreaves* (2002) and *Kelley* (2009). Chapter 3 gives an introduction to the incoherent scatter technique and the EISCAT radars. The purpose of this chapter is to give a simplified description of the instruments which our data came from with its advantages and limitations. In chapter 4, the IRI model is introduced. Chapter 5 describes long-term trends in the ionosphere with special emphasis on studies from polar latitudes, or studies using incoherent scatter radars. In chapter 6, summaries of the papers included in this dissertation are presented, and a summary of the most important conclusions are listed in chapter 7. The papers included in this dissertation are found in chapter 8.

Chapter 2

The Polar Ionosphere

In 1901 Guglielmo Marconi managed to transmit signals wireless across the Atlantic Ocean for the first time in history. Thus, he indirectly discovered the **ionosphere**; An ionized part of Earth's upper atmosphere, stretching from about 60 to 1000 km altitude. The idea of the ionosphere was, however, older. Already in 1839 Carl Friedrich Gauss proposed that there might be a conducting layer in the atmosphere (e.g. *Glassmeier and Tsurutani*, 2014). Oliver Heaviside and Arthur Edwin Kennelly independently proposed that Marconi's successful transatlantic transmission of signals could be explained by an electric conducting layer in the atmosphere reflecting the radiowaves. In 1924 Edward Appleton and Miles Barnett finally proved the existence of the electric layer proposed by Heaviside and Kennelly, the Kennelly-Heaviside layer (*Appleton and Barnett*, 1925).

The purpose of this chapter is to give a brief introduction to the ionosphere in general and the polar ionosphere in particular; its production and loss, structure and phenomena which occur at high latitudes and are relevant for this thesis. The **polar ionosphere** is typically defined to be the region of the ionosphere above 60°-70° magnetic latitude. However, *Heelis* (1982) defines it already above 50°. The presentation of the phenomena described in this chapter is based on the books by *Baumjohann and Treumann* (1996), *Brekke* (2013), *Hunsucker and Hargreaves* (2002) and *Kelley* (2009). Interested readers are referred to these books for a more elaborate coverage of the topics introduced in this chapter.

2.1 An overview of the ionosphere and the atmosphere

The Kennelly-Heaviside layer is today better known as the ionospheric E-layer. It was denoted the E-layer by Appleton because of its reflection of electromagnetic waves. Shortly after, Appleton discovered two additional layers, one above and one below the E-layer (*Appleton*, 1927). These layers were called the D- and the F-layers. Figure 2.1 shows typical midlatitude electron densities and altitudes of the nighttime and daytime ionospheric layers during solar maximum and solar minimum. As the altitude of the ionospheric layers varies during different conditions such as time of day, season and solar activity, and since the boundaries between the different layers are not clear, it is common to refer to the different ionospheric layers as ionospheric regions. A brief overview of typical characteristics of the different ionospheric regions is given below:

D-region: The D-region is the lowermost ionospheric region, and is located at altitudes between about 60 and 90 km above Earth. Typical daytime electron densities are 10^8-10^{10} m^{-3}. At nighttime the D-region disappears. Negative ions are present, and due to high collision frequencies this region is mainly controlled by interactions with the neutral gas and its complex chemistry. As the D-region is not investigated in this dissertation, it will not be further discussed.

E-region: The E-region is the middle region, and lies between 90 and 150 km altitude. At daytime, electron densities are typical in the range 10^{10}-10^{11} m^{-3}. At nighttime, the electron density is reduced to approximately 10^9-10^{10} m^{-3}. Peak density occurs at about 110 km altitude. In this region electrons follow the $\mathbf{E}\times\mathbf{B}$ drift, while the ions are governed by collisions with the neutrals. As a consequence, strong currents exist, and the E-region is also referred to as the dynamo layer.

F-region: This is the uppermost ionospheric region, and where the ionization is highest. It is located between about 150 km and 500 km altitude. F-region electron densities are typically in the range 10^{10}-10^{12} m^{-3}. At daytime the F-region at mid- and low latitudes is split into the F1- and F2-region as shown i figure 2.1, but at nighttime this distinction disappears. In this region both the ions and the

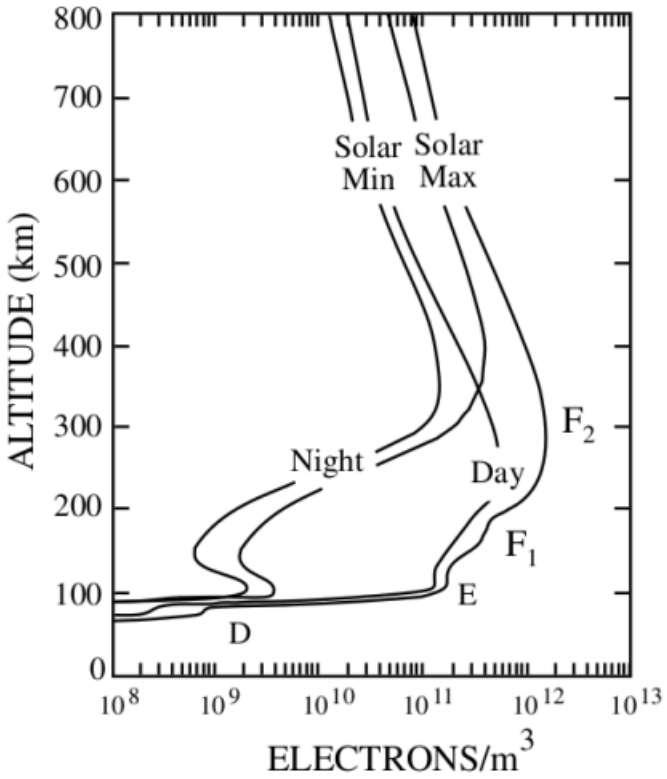

Figure 2.1: Typical nighttime and daytime electron density profiles from the midlatitude ionosphere during solar minimum and maximum conditions. From *Richmond* (1987). Reprinted with permission from Terra Scientific Publishing Company (TERRAPUB).

electrons follow the $\mathbf{E}\times\mathbf{B}$ drift.

The ionosphere is embedded in the neutral upper atmosphere, and only a tiny fraction (<<1%) of the atmospheric particles are ionized. Interactions between neutrals, ions and electrons play a major role in ionospheric dynamics. A brief overview of the atmospheric structure is therefore included here. Figure 2.2 shows vertical profiles of atmospheric temperature and mean molecular mass. These

profiles are commonly used to divide the atmosphere into different regions. By using the temperature profile, the atmosphere can be divided into 4 main layers. The lowest region, up to approximately 10 km altitude, is the **troposphere** where the temperature decreases. Above the troposphere lies the **stratosphere** where the temperature increases. Most of the ozone is located here, and the temperature increase is mainly caused by ozone absorbing solar UV radiation. From above 50 km altitude, the temperature again starts to decrease. This region is called the **mesosphere**, and the D-region is located here. The uppermost of the main regions is called the **thermosphere**, and is located above approximately 80 km altitude. Here the temperature increases due to the absorption of solar UV and EUV radiation. This is where the E-and F-regions are located. At altitudes above approximately 700 km, the temperature is more stable. This region is referred to as the exosphere.

As shown in figure 2.2, the atmosphere can also be divided into two different regions based on the mixing of atmospheric gases. The region below 100 km altitude is called the **homosphere**. In the homosphere, the atmospheric gases are fully mixed due to turbulence and the mean molecular mass is constant. The homosphere is composed of approximately 80% N_2 and 20% O_2. Above the homosphere lies the **heterosphere**, where the composition and mean molecular mass have large variations.

Altitude profiles of ion, electron and neutral temperatures between 100 and 600 km are shown in figure 2.3. The ionosphere is mainly heated due to absorption of solar UV radiation. Variations in ionospheric temperatures are large and can be caused by different processes including seasonal changes, diurnal changes and changes in solar activity. In the upper F-region, the electron temperature is higher than the ion and the neutral temperatures, and the ion temperature is higher than the neutral temperature. Thermal electrons are heated by the photoelectrons, and ions are heated by collisions with thermal electrons. Electrons have a larger heat conductivity than ions, and ions are significantly cooled via collisions with neutrals. As a result, the electron temperature is higher than the ion temperature. Below ~250-350 km, where the neutral density is higher, the ion temperature is nearly

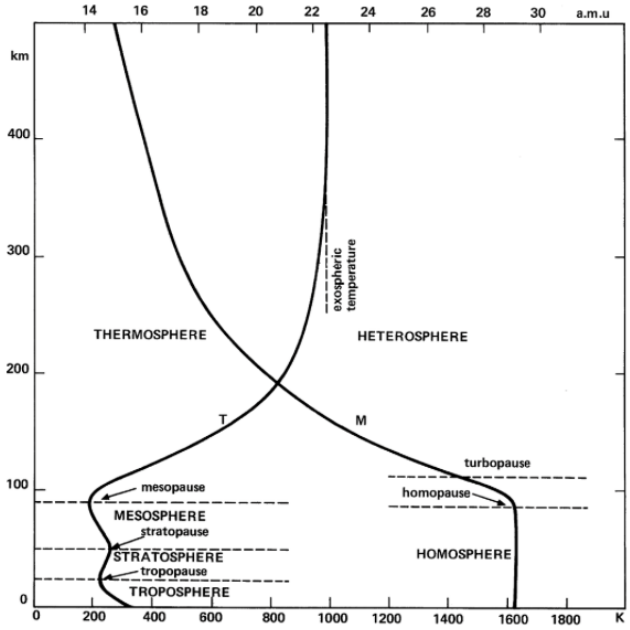

Figure 2.2: Typical structure of the atmosphere. Both the temperature profile and the profile of mean molecular mass are shown in the figure. Reprinted by permission from Springer Nature: Springer The Atmosphere and the Vertical Structure of the Ionospheric Plasma. In: Ionospheric Techniques and Phenomena by Giraud, A. and Petit, M. Copyright (1978).

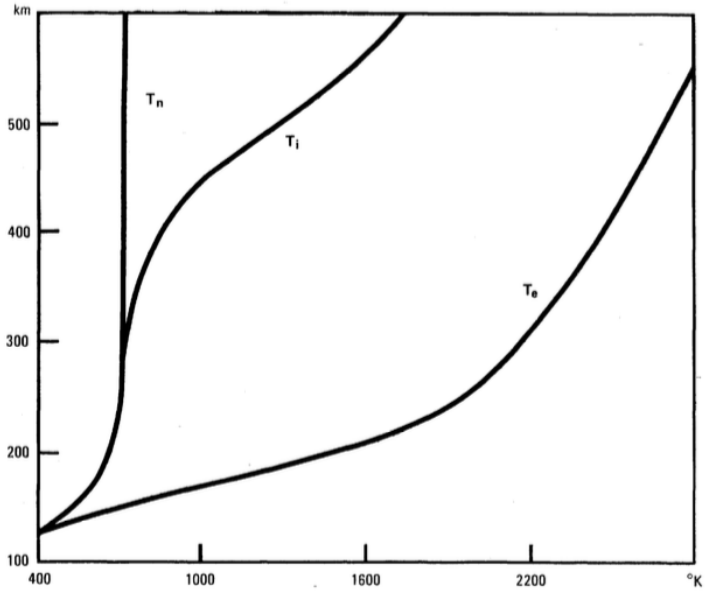

Figure 2.3: Altitude profiles of ion, electron and neutral temperatures. Reprinted by permission from Springer Nature: Springer The Atmosphere and the Vertical Structure of the Ionospheric Plasma. In: Ionospheric Techniques and Phenomena by Giraud, A. and Petit, M. Copyright (1978).

identical to the neutral temperature. Below ~120-140 km altitude, the atmosphere is very dense, and therefore also the electron temperature will approach the neutral and ion temperatures via collisions with the neutrals. At polar latitudes, E-region ion temperatures are sometimes larger than the electron temperatures due to Joule heating.

2.2 Formation of the ionosphere; Production and Loss mechanisms

Photoionization by solar radiation is the most dominant source of ionization in the ionosphere, but at polar latitudes, and particular in the auroral zone, particle precipitation also plays a major role. In this chapter we will focus on production by solar radiation. Production by particle precipitation will be treated in chapter

2.3. Loss of ionization is caused by recombination and attachment, and will also be treated in this chapter.

Chapman (1931) provided a simple model for plasma production in the ionosphere. This model is known as the Chapman production function and can be expressed by:

$$q(\chi, y) = q_{max}(0) \exp^{[1-y-\sec\chi \exp^{-y}]} \tag{2.1}$$

Here q is the photoionization rate as a function of solar zenith angle χ and reduced height y. The reduced height is given by

$$y = \frac{z - z_{max}}{H}$$

where z is the altitude, z_{max} is the height of maximum plasma production and H is the atmospheric scale height given by

$$H = \frac{k_B T}{mg}$$

Here k_B is the Boltzmann constant, T is the atmospheric temperature, m is the mass of the molecules and g is the acceleration of gravity. $q_{max}(\chi)$ is the maximum plasma production and is given by

$$q_{max}(\chi) = \frac{\eta I_{\infty\lambda} \cos(\chi)}{He} = q_{max}(0) \cos(\chi) \tag{2.2}$$

Here η is the ionization efficiency, the number of ion-electron pairs produced per absorbed photon. $I_{\infty\lambda}$ is the intensity of solar radiation outside the atmosphere at wavelength λ falling towards the atmosphere with a solar zenith angle χ. e is Euler's number. Figure 2.4 shows Chapman production profiles for different solar zenith angles. As the solar zenith angle increases, the height of the maximum production increases and the maximum production decreases. This means that the plasma production is significantly lower at nighttime than during daytime.

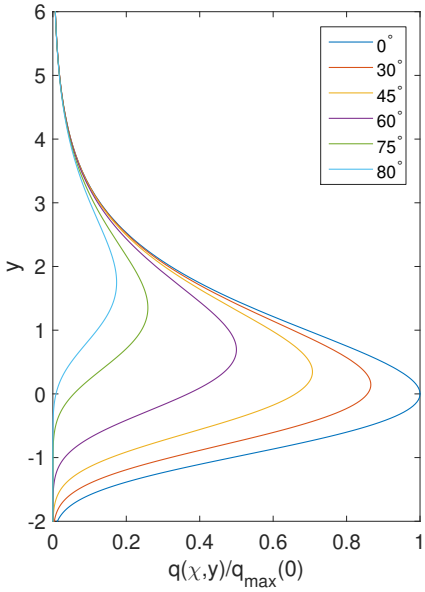

Figure 2.4: Chapman production profiles for different solar zenith angles (χ). The reduced height is given along the y-axis and the relation q(χ, y)/q$_{max}$(0) along the x-axis. The different colored lines correspond to different solar zenith angles (χ).

In the **E-region**, plasma production is primarily caused by photoionization by solar UV radiation with wavelengths in the range 100-150 nm and X-rays with wavelengths in the range 1-10 nm. The two dominant ion species are NO^+ and O_2^+. These are created by dissociation of O_2, N_2 and NO to O_2^+, N_2^+ and NO^+. N_2^+ disappears rapidly due to charge exchange with O_2 and O. In the upper E-region O^+ is also important. Loss of ionization in the E-region is usually due to dissociative recombination of a molecule, XY^+, to two atoms, X and Y:

$$XY^+ + e \rightarrow X + Y \tag{2.3}$$

Thus, NO^+ will recombine to N and O, while O_2^+ recombine to two oxygen atoms. Dissociative recombination is a fast reaction, and the plasma density is therefore

strongly reduced at nighttime when the photoionization rate drops.

The recombination rate is proportional to the product of the electron and ion densities. As the ionosphere is a **plasma**, that is; a gas of electric charges which contain about the same number of electron and ions, the recombination rate is given by $\alpha_{eff} N_e^2$. Here α_{eff} is the effective recombination coefficient and N_e is the electron density. The E-region can therefore be described as a **Chapman-α layer** with electron density given by the continuity equation:

$$\frac{dN_e}{dt} = q - \alpha_{eff} N_e^2 \tag{2.4}$$

By inserting equation 2.2 in equation 2.4, it can be shown that the maximum electron density is given by

$$N_{e,max} = \sqrt{\frac{q_{max}(0)}{\alpha_{eff}}} \cos(\chi)^{1/2}$$

In the **F-region**, O^+ is the dominant ion species. Below about 200 km altitude, NO^+ and O_2^+ are also abundant. F-region plasma production is mostly caused by photoionization by solar UV radiation with wavelengths in the range 17 nm to 91 nm. O^+ can be lost due to charge exchange with N_2 and O_2 resulting in O_2^+ and NO^+. Then O_2^+ and NO^+ are lost due to dissociative recombination following equation 2.3. Another possibility is loss of O^+ due to radiative recombination:

$$O^+ + e \rightarrow O + h\nu \tag{2.5}$$

Here an atomic oxygen ion and an electron recombines to an oxygen atom and a photon is emitted. The recombination rate is much higher for dissociative than for radiative recombination, and charge exchange followed by dissociative recombination is therefore the dominant loss process in the F-region.

In the lower F-region, the situation is similar to the E-region and the ionosphere could be described as a Chapman-α layer. At higher altitudes, where O^+ is dominating, the recombination rate is given by βN_e^2 where β is a height dependent recombination coefficient and the electron density is given by the continuity equation:

$$\frac{dN_e}{dt} = q - \beta N_e \tag{2.6}$$

This is called a Chapman-β layer, and the electron density varies as q/β.

2.3 Particle precipitation

Another source of ionospheric plasma is particle precipitation. This is especially important at auroral latitudes where the Earth's magnetic field connects with the interplanetary magnetic field. At these latitudes, energetic particle precipitation can cause a high E-region plasma density even at nighttime.

Most of the precipitating particles originate from the **magnetosphere**. The magnetosphere is the region dominated by the Earth's magnetic field, and charged particles gyrate around the magnetic field lines as they oscillate the two hemispheres. The point where the particle is reflected back towards the other hemisphere is called the **mirror point**. If this point is located too far down in the atmosphere, the particle will not be reflected. It will loose most of its energy through collisions with neutrals before it reaches the mirror point. The energy of the precipitating particles cause increased ionization, excitation and heating. Aurora is observed when the precipitating particles excite atoms and molecules. Typically, the aurora is visible in a belt around the geomagnetic poles. The area where the aurora is visible is called the **auroral oval**. Usually, the auroral oval is located at a latitude of about 70°. This area, where the auroral oval is most often located, is called the **auroral zone**.

Both ions and electrons can precipitate. However, ions have a lower ionization efficiency and therefore a higher stopping height than electrons of the same energy.

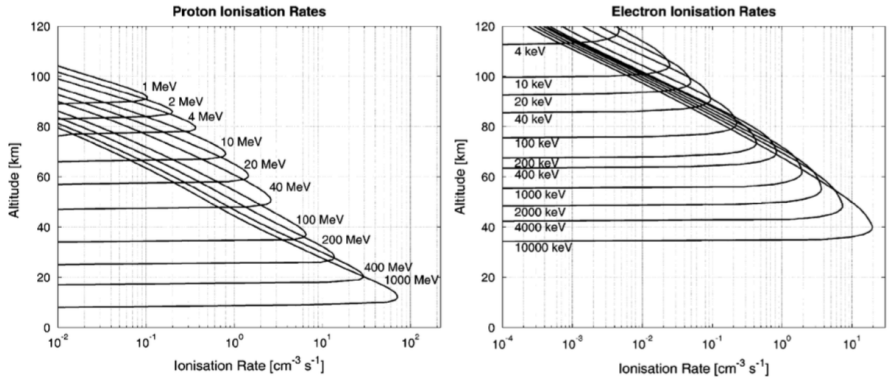

Figure 2.5: Ionization rates of protons (left) and electrons (right) for different levels of energy. Reprinted from Journal of Atmospheric and Solar-Terrestrial Physics, 71 (10), Turunen et al, Impact of different energies of precipitating particles on NOx generation in the middle and upper atmosphere during geomagnetic storms, 1176-1189, Copyright (2009), with permission from Elsevier.

Precipitating particles collides with neutrals as they penetrate the ionosphere and produce electron-ion pairs. The largest amount of energy is deposited at the precipitating particle's stopping height. More energetic particles are able to penetrate deeper into the ionosphere before their energy is lost, and thus have a lower stopping height. An illustration of how the stopping height of monoenergetic beams of protons (left) and electrons (right) varies according to the level of energy is shown in figure 2.5. An important difference between proton and electron precipitation is that precipitating protons can capture electrons and form neutral hydrogen atoms.Until the captured electron is lost again due to collisions, the particle will therefore move freely with respect to the magnetic field.

2.4 Plasma transportation

In addition to production and loss, the plasma concentration in a region is determined by plasma transport into and out of that region. At high latitudes, the plasma transport is primarily controlled by the magnetosphere-ionosphere coupling. Typical is the ionospheric two-cell convection pattern, driven by reconnection between

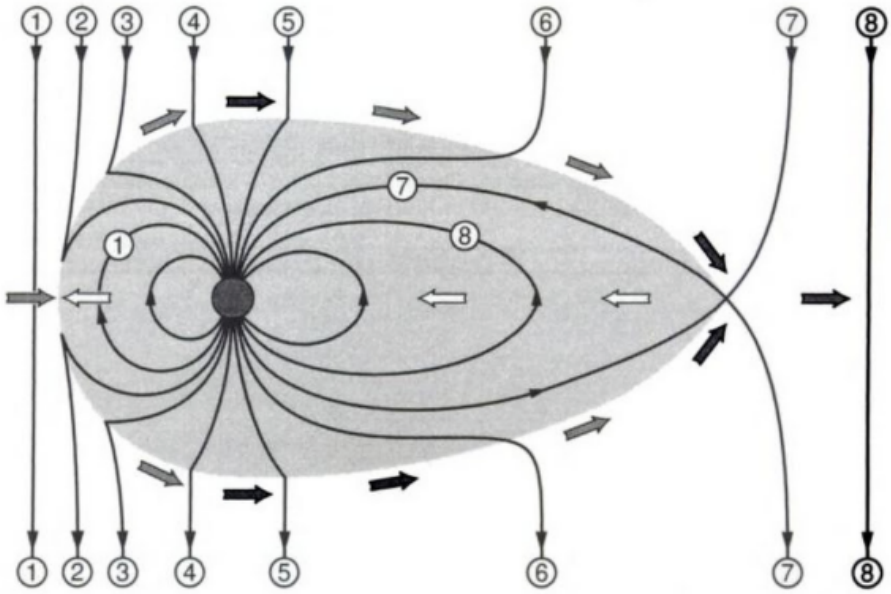

Figure 2.6: The Dungey cycle: Merging and reconnection. Reprinted from Basic Space Plasma Physics, Baumjohann and Treumann, Copyright (1996), Imperial College Press.

the interplanetary magnetic field (IMF) and the Earth's magnetosphere. This reconnection process is called the **Dungey cycle** (*Dungey*, 1961) and is shown in figure 2.6. When the IMF and the Earth's geomagnetic field are oriented in the opposite directions, the IMF field line will merge with the closed field line of the geomagnetic field as it encounters the magnetopause (line 1 in figure 2.6). The merged field lines are then split into two open field lines (line 2), which are convected tailwards across the polar cap by the solar wind (line 3-6). In the magnetotail, the open and stretched field lines meet again and are reconnected, meaning that the geomagnetic field line is again closed (line 7). The newly closed magnetic field line will relax and move towards Earth due to magnetic tension. The cycle is completed when the closed field line is transported back to the dayside magnetosphere, and can start a new cycle (*Baumjohann and Treumann*, 1996).

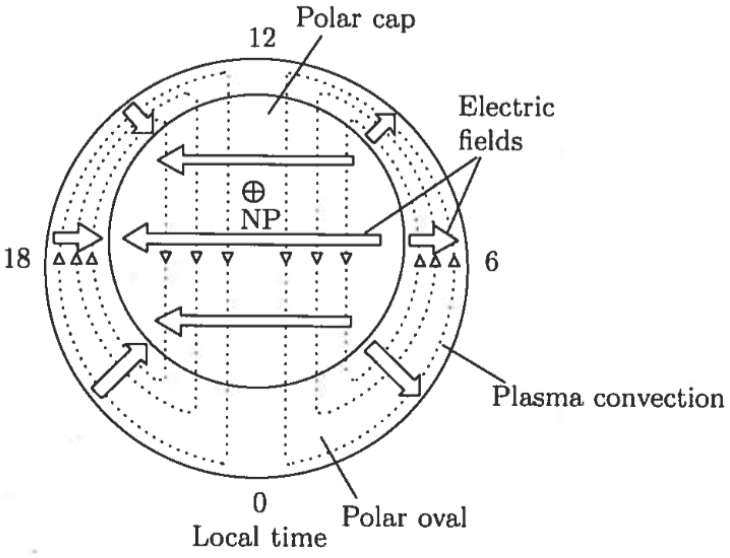

Figure 2.7: The ionospheric convection pattern and ionospheric electric fields. Republished with permission of Springer, from Physics of the Earth's Space Environment An Introduction by Prölss, Gerd W. Copyright (2004); permission conveyed through Copyright Clearance Center, Inc.

As the magnetic field lines have a footpoint in the ionosphere, the magnetospheric convection will cause motion in the ionosphere. From the Earth's reference frame, the electric field in the solar wind is given by $E = -v \times B$, where v is the velocity of the flux tubes and B is the magnetic field. Along the magnetic field lines the conductivity is high, and the electric field from the magnetosphere will therefore be mapped down to the ionosphere. If the IMF is directed southwards, the resulting ionospheric electric field will be directed from dawn to dusk in the polar cap. In the F-region the electric field causes $E \times B$ drift of plasma in the antisunward direction across the polar cap. In the auroral zone the electric field is directed from dusk to dawn. This electric field is connected to the closed magnetic field lines moving back to the dayside magnetosphere. As a result, a return flow of plasma occur in the F-region auroral zone. The F-region convection pattern and the associated electric fields are illustrated in figure 2.7. Due to the higher density of neutrals in the E-region, the transport of ions in the E-region is dominated by collisions

while electrons continue to be controlled by $E \times B$ drift. The ionospheric convection pattern depends strongly on the direction of the IMF. Figure 2.8 illustrates this, and shows how the convection pattern can vary depending on IMF orientation.

Sometimes regions of enhanced plasma density enter the convection pattern. During disturbed geomagnetic conditions, the midlatitude F-region plasma density can increase significantly. This high-density plasma can be transported into the polar cap where it forms a tongue of ionization which stretches from the dayside to the nightside (e.g. *Foster et al.*, 2005; *Liu et al.*, 2015). Frequently, the incoming plasma is segmented into polar cap patches; 100-1000 km sized islands of high plasma density (e.g *Lockwood and Carlson*, 1992; *Sojka et al.*, 1993). Polar cap patches can also be created by soft particle precipitation in the cusp region (e.g. *Walker et al.*, 1999; *Oksavik et al.*, 2006). The patches follow the convection pattern antisunward across the polar cap. When the patch exits the polar cap and enters the auroral zone it becomes a blob (e.g. *Tsunoda*, 1988; *Crowley et al.*, 2000).

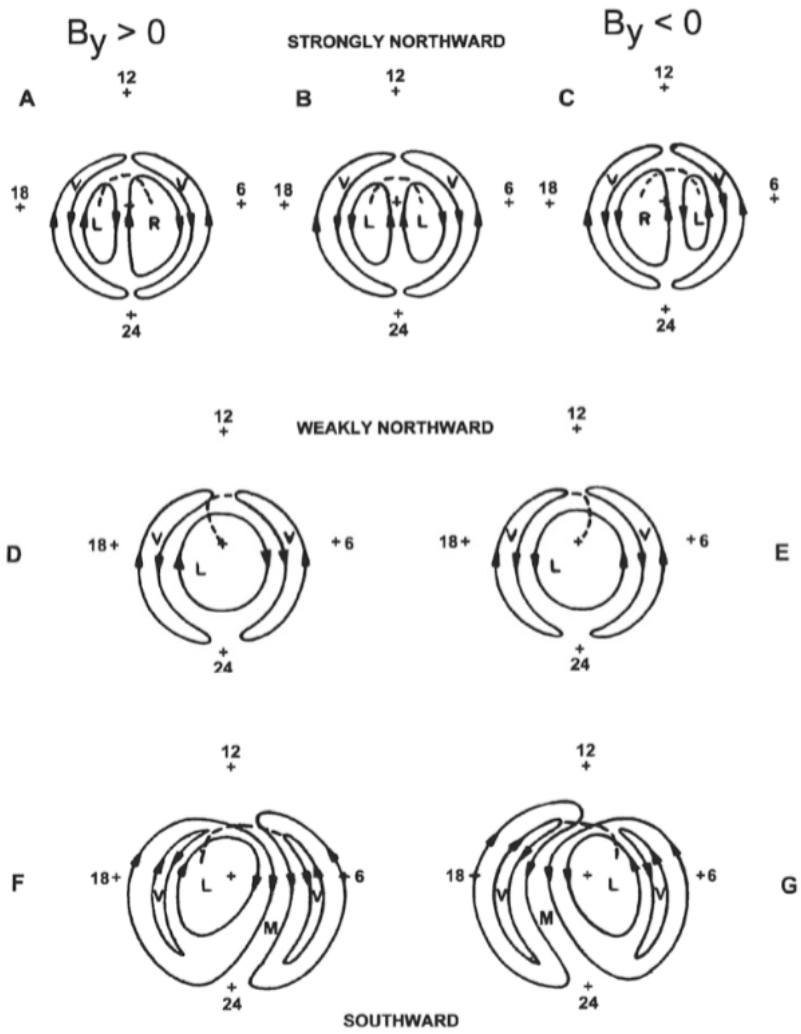

Figure 2.8: The ionospheric convection pattern for various IMF orientations in the northern polar cap. Figures A, D and F correspond to a positive B_y component, figure B to $B_y = 0$ and figures C, E and G to a negative B_y component. Figures A, B and C show the situation for strongly northward IMF (B_z >0), figures D and E for weakly northward IMF and figures F and G for southward IMF (B_z <0). Viscous cells are marked with a "V", merging cells are marked with an "M", lobe cells with "L" and the cells marked with an "R" are "reclosure" cells where the plasma flow sunward on closed field lines. From *Reiff and Burch* (1985). Copyright 1985 by the American Geophysical Union.

2.5 Troughs and depletion regions

As well as regions of enhanced plasma, as tongues, patches and blobs are examples of, there exists regions of electron density depletion. In this dissertation, the term depletion region is used as a general concept to describe large-scale regions of electron density depletion which occur in the ionospheric F region. One example of such depletion regions is the ionospheric trough. Ionospheric troughs are regions with significant plasma depletion, but the depth and the width of the trough is not clearly defined (*Moffett and Quegan*, 1983). In literature, there exist some ambiguity of the definition of depletion regions, and a clear distinction between the different types are sometimes lacking. However, troughs are often referred to as regions of electron density depletion elongated in the east-west direction, and holes are depletion regions without a clear spatial structure (e.g. *Hunsucker and Hargreaves*, 2002).

Two different mechanisms, both connected to plasma convection, are known to create ionospheric troughs. The first of these mechanisms is related to stagnation regions in the convection pattern. At high latitudes, a stagnation region is formed in the dusk sector due to corotation counteracting the sunward return flow seen in figure 2.7. As a consequence, convection through this region is slow and recombination can occur for a prolonged time period which will cause the formation of troughs (e.g. *Knudsen*, 1974; *Spiro et al.*, 1978; *Rodger et al.*, 1992). The second formation mechanism of such depletion regions is related to frictional heating (*Winser et al.*, 1986; *Rodger et al.*, 1992). Frictional heating leads to higher ion temperatures and upwelling of neutral nitrogen and oxygen from the E-region into the F-region. Both the higher ion temperature and the increased concentrations of nitrogen and oxygen result in a higher loss coefficient, and thereby an increased recombination rate. In addition, frictional heating may cause an upward field-aligned plasma flow. The field-aligned transport and/or increased recombination caused by frictional heating will lead to the formation of troughs.

Most studied is probably the mid-latitude trough, also referred to as the main trough. The mid-latitude trough was first discovered in data from the Alouette topside

sounder in the 1960s (*Muldrew*, 1965). Since then, investigations of the formation mechanisms, morphology and variations of the trough have been conducted, using primarily satellite (e.g. *Horvath and Essex*, 2003; *Lee et al.*, 2011) and incoherent scatter radar data (e.g. *Collis and Häggström*, 1988; *Voiculescu et al.*, 2016). It is usually located in the subauroral zone at invariant latitudes between 55° and 75°. Typically, it is between 5° and 10° degrees wide in latitude and extended in the longitudinal direction. It can be observed at any time of day, but has the highest occurrence at nighttime (e.g. *Moffett and Quegan*, 1983; *Ishida et al.*, 2014). Both time of day and geomagnetic activity will, however, affect the location of the mid-latitude trough. It is located at high latitudes during local noon and starts to move towards lower latitudes in the afternoon. Increasing geomagnetic activity also results in the trough moving to lower latitudes (e.g. *Werner and Prölss*, 1997; *Voiculescu et al.*, 2006).

Troughs that occur in the auroral zone or in the polar cap are called high-latitude troughs. In their review paper, *Rodger et al.* (1992) summarize the different trough categories at both mid-and high latitudes. In addition to troughs created due to increased recombination or upflow of plasma, they identify a category of apparent troughs in the polar cap. These are not real regions of density depletion, but the normal background ionosphere between two polar cap patches. For further information about various categories of high-latitude troughs and their locations, readers are referred to figure 19 in *Rodger et al.* (1992).

Although less studied than the mid-latitude trough, some studies also exist of high-latitude troughs. *Voiculescu et al.* (2016) investigated the properties of post-midnight troughs centered at about 70° in summer. They found that these troughs are most likely formed during a two-step process starting with a faster recombination due to energetic particle precipitation, and thereafter further depletion caused by frictional heating when the plasma enters a region with high eastward flow. *Zou et al.* (2013) investigated the electrodynamics of a high-latitude trough and found that this trough was associated with downward field-aligned currents. In paper III of this thesis we further investigate the properties of depletion regions occuring at high-latitudes. *Bjoland et al.* (2017b) show that a high-latitude

depletion region is located in the early morning sector, and that this depletion region expands in the polar cap as geomagnetic activity increases.

2.6 Currents in the ionosphere

The ionosphere is conductive, and carry electric currents. In the high-latitude ionosphere **Birkeland currents**, also known as field-aligned currents, flow along the magnetic field lines and are essential for the magnetosphere-ionosphere coupling. As can be seen in figure 2.9, Birkeland currents are distributed in two concentric rings located inside the auroral oval. The poleward ring is the region 1 currents, and the equatorward ring is the region 2 currents. Region 1 currents flow into the ionosphere in the morning local times and away from the ionosphere during the afternoon local times and connect the auroral oval to a region called the **magnetosheath**. The magnetosheath surrounds the magnetosphere and its plasma is dominated by particles originating from the solar wind. Region 2 currents flow away from the ionosphere during the morning hours and into the ionosphere during the afternoon. The region 2 currents connect the auroral oval with the inner magnetosphere.

Birkeland currents are primarily closed by **Pedersen currents** in the ionosphere. Pedersen currents flow perpendicular to the magnetic field and parallel to the electric field. In addition to Birkeland currents and Pedersen currents, there are **Hall currents** which flow perpendicular to both the electric and the magnetic field. Pedersen and Hall currents have their greatest intensity in the E-region (e.g. *Prölss*, 2004). These currents are driven by the electric fields described in chapter 2.4, and the Pedersen currents are therefore directed poleward in the afternoon sector and equatorward in the morning sector. The relation between the currents and the electric fields are given by Ohms law:

$$\mathbf{j} = \boldsymbol{\sigma} \cdot (\mathbf{E} + \mathbf{v_n} \times \mathbf{B}) \tag{2.7}$$

Here $\mathbf{j}$ is the current, $\boldsymbol{\sigma}$ is the conductivity, $\mathbf{E}$ is the electric field, $\mathbf{v_n}$ is the neutral wind and $\mathbf{B}$ is the magnetic field. In the auroral oval the $\mathbf{v_n} \times \mathbf{B}$ term is much

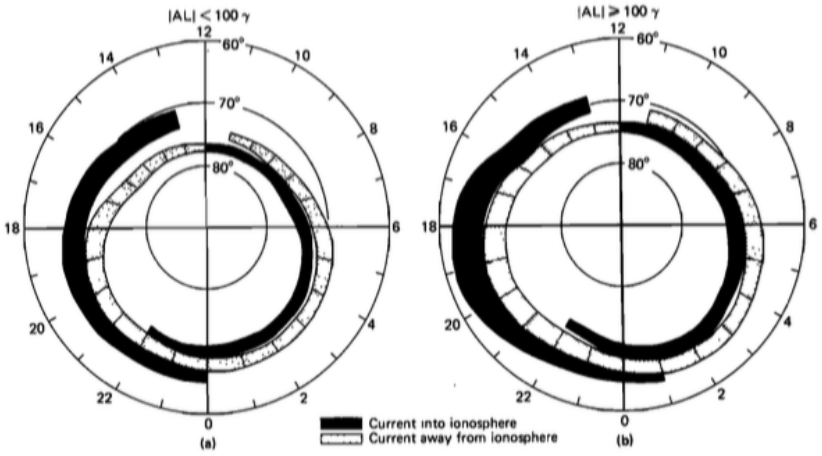

Figure 2.9: Birkeland currents into and away from the ionosphere during weak (a) and active (b) disturbances. From *Iijima and Potemra* (1978). Copyright 1978 by the American Geophysical Union.

smaller than the electric field term and can therefore be neglected.

The Pedersen conductivity (σ_P) and the Hall conductivity (σ_H) are given by the following expressions:

$$\sigma_P = \frac{n_e \cdot e}{B}\left(\frac{k_e}{1+k_e^2} + \frac{k_i}{1+k_i^2}\right) \tag{2.8}$$

and

$$\sigma_H = \frac{n_e \cdot e}{B}\left(\frac{k_e^2}{1+k_e^2} - \frac{k_i^2}{1+k_i^2}\right) \tag{2.9}$$

Here n_e is the electron density, e is the electron charge and k_e and k_i are the electron and ion mobility coefficients. The mobility coefficient are calculated from the following expressions:

$$k_i = \frac{\Omega_i}{\nu_{in}} \qquad \text{and} \qquad k_e = \frac{\Omega_e}{\nu_{en}}$$

Here Ω_i and Ω_e are the ion and electron gyrofrequencies, and ν_{in} and ν_{en} are the ion-neutral and the electron-neutral collision frequencies. The peak height of the Hall conductivity is strongly connected to the E-region peak height of the electron density profile, and is located at approximately 110 km altitude. The peak height of the Pedersen conductivity is found at a higher altitude, approximately 120 km, and is closer to the height where the ion gyrofrequency equals the ion-neutral collision frequency.

In paper II, we derive the Hall conductivity and its peak height using EISCAT data in order to investigate if there exist a long-term trend in the conductivity peak height.

Chapter 3

The EISCAT radars

Soon after its discovery, instruments were developed to further investigate the ionosphere. Already in 1925, *Breit and Tuve* (1925) invented an early version of the ionosonde. Basically, an ionosonde is a radar device that works by transmitting short radio pulses which are reflected in the ionosphere. Information about the peak heights and electron densities of the ionospheric layers can be obtained from this type of radar. Since the first ionosonde, there has been a continuous development of instrumentation used for ionospheric research. One major breakthrough came in 1958 when the theory behind incoherent scatter radars was developed (*Gordon*, 1958), and the first incoherent scatter measurements were performed (*Bowles*, 1958). Incoherent scatter radars are one of the most powerful tools to study the ionosphere as they provide information about several plasma parameters for a wide altitude range. Among the incoherent scatter radars that are operational today are the EISCAT radars which cover the ionosphere in the auroral zone, polar cap and cusp region. In addition to ionosondes and incoherent scatter radars, a multitude of different instruments, including passive ground-based instrumentation, coherent radars and instruments on satellites and rockets, are used for ionospheric research. Together they complement each other, and provide us great opportunities to learn about the near-Earth space.

The purpose of this chapter is to introduce the instruments and methods of obtaining data used in this dissertation. EISCAT radar data have been used in all

the included papers, and this chapter will therefore primarily focus on giving a brief introduction to incoherent scatter theory, the EISCAT radars, and how the data are analyzed. The chapter is based on the manuscript by *Farley and Hagfors* (lecture notes, UiT) and the book by *Nygrén* (1996), and interested readers are referred to these books for a more detailed introduction to incoherent scatter radar theory. Since ionosonde data were used to scale the EISCAT data in paper II, a brief introduction of the ionosonde is also included in section 3.3 at the end of this chapter.

3.1 Incoherent Scatter Radar Theory

Incoherent scattering refers to the weak backscatter by electrons hit by a high power radio pulse. The basic principle behind this mechanism is Thomson scattering. When a radio wave encounters free electrons, the electric field of the wave will cause the electrons to oscillate and thus emit radiation. However, electrons in the ionosphere are not free, but connected to the ions trough electrostatic forces. Each of the charged particles in a plasma will repel particles with the same charge and attract particles with the opposite charge. A shielding cloud will therefore appear around each charged particle. This is known as **Debye shielding**. The length over which the electric field is shielded is called the **Debye length** and the electron Debye length is given by

$$\lambda_D = \left(\frac{\epsilon_0 k_B T_e}{n_e e^2} \right)^{1/2} \tag{3.1}$$

Here ϵ_0 is the permittivity of free space, k_B is the Boltzmann constant, T_e is the electron temperature, n_e is the electron density and e is the electron charge. Incoherent scatter radars transmit with wave lengths larger than the Debye length, and as electrons follow the ions to shield the electric potential, the received signal is controlled by the ion motion.

Only a tiny fraction of the transmitted power is returned, so big antennas and sensitive receivers are needed. Typically, the transmitted power is approximately a megawatt, while the power of the received signal is less than a picowatt. The

autocorrelation function of the signal is estimated, and via Fourier transform, the power spectrum is found. Figure 3.1 shows the characteristic shape of a power density spectrum from the F-region.

The double-humped line in the middle of the figure is called the **ion line** and is due to the up- and downshifted ion acoustic waves. Its double-humped shape is caused by Landau damping of the ion acoustic waves. The dispersion relation of these waves is given by

$$\omega = kC_s \tag{3.2}$$

where k is the wavenumber and C_s is the ion-acoustic speed given by

$$C_s = \left(\frac{\gamma_e k_B T_e + \gamma_i k_B T_i}{m_i} \right)^{1/2} \tag{3.3}$$

Here γ_e and γ_i are the ratios of specific heats for electrons and ions, respectively. k_B is the Boltzmann constant, T_e is the electron temperature, T_i is the ion temperature and m_i is the ion mass. The two peaks of the ion line are located approximately where $\omega = \pm kC_s$. From the ion line, a significant amount of information about the ionosphere can be obtained. As it is electrons that scatter the transmitted radio wave, the power of the received signal is proportional to the electron density in the scattering volume. The received power is proportional to the integral of the ion line, and the electron density can therefore be derived from the ion line. From equations 3.2 and 3.3 we see that the width of the ion line depends on the temperatures and the ion mass, and the width increases with increasing temperatures. Furthermore, the peak-to-valley ratio of the ion line gives the temperature ratio T_e/T_i. Together, the width of the ion line and the peak-to-valley ratio can therefore be used to calculate the ion and electron temperatures. Line-of-sight velocity can be determined from the Doppler shift. These primary plasma parameters, which are derived directly from the ion line, can also be used to derive many other parameters. An example of this can be seen in paper II, where the Hall conductivity is derived using electron density from

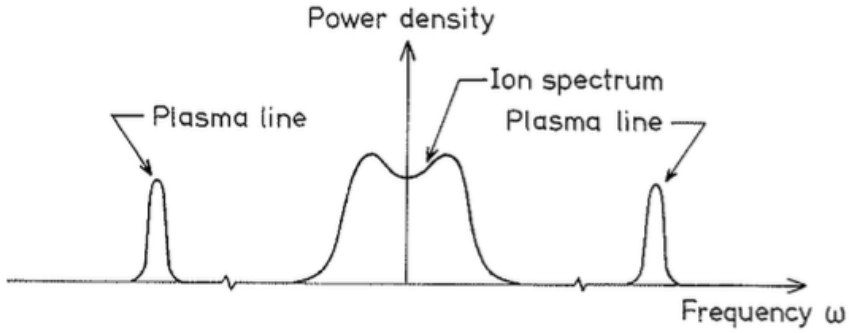

Figure 3.1: Typical F-region power density spectrum. From *Bjørnå* (2005).

incoherent scatter radar instruments.

The two other lines shown in figure 3.1 are called **plasma lines** and are due to electron-acoustic waves. These are shifted far away from the central ion line and are situated approximately at the plasma frequency. They are usually not visible since ion-acoustic waves dominate due to the high ion mass. However, when electron-acoustic waves are excited, for example by photoelectrons or during energetic particle precipitation events, they are visible and can be used to determine the electron density. When plasma lines are visible, they provide an independent measurement of the electron density, and are therefore an excellent tool to calibrate the received power from the ion line. It is necessary to calibrate the received signal because it can be affected by technical aspects of the experiment. Usually, the received power is calibrated using ionosonde data to avoid such errors in the measurements.

Random statistical errors will always occur in incoherent scatter radar data. Some of these errors are caused by the radar system itself. For example, thermal noise is generated by the receiver. Such noise is usually reduced by cooled preamplifiers. Other noise is of cosmic origin. In addition, clutter and interference can affect the received signal. Clutter refers to unwanted radar signals caused by reflections

from targets such as mountains, ocean waves, satellites, meteors or space debris. Due to the weak backscattered signal, the signal-to-noise ratio is usually less than 1. To improve the signal-to-noise ratio, separate measurements of the background is made and subtracted from the measurement of the signal. It is also possible to improve the signal-to-noise ratio by improving the signal strength. This can be done by increasing the length of the transmitted pulse, however, a larger pulse length will also result in poorer height resolution.

3.2 EISCAT

There are about 6 incoherent scatter radars located in the polar ionosphere. Poker Flat Incoherent Scatter Radar (PFISR) and the EISCAT UHF and VHF radars are located in the auroral zone, while Sondrestrom and ESR cover the cusp area. Resolute Bay Incoherent Scatter Radar (RISR) is located within the polar cap. Figure 3.2 shows the location of the EISCAT radars.

EISCAT Scientific Association was established in 1975 with the aim to build and run an incoherent scatter radar in the auroral zone. In 1981, the EISCAT UHF radar, located near Tromsø, could start its measurements. The EISCAT UHF radar transmits with a frequency of 930 MHz and the peak power of the transmitter is 2 MW. Its antenna is fully steerable in azimuth and elevation and has a diameter of 32 m. A picture of the antenna is seen in figure 3.3. Initially, the EISCAT UHF radar was operated as a tristatic radar. In addition to the receiver in Ramfjordmoen close to Tromsø, additional receivers are located in Kiruna, Sweden, and Sodankylä, Finland. A tristatic radar is able to provide estimates of the full velocity vector in the scattering volume. In 1985, the EISCAT VHF radar started its operation. This radar transmits with a frequency of 224 MHz and a peak power of 3 MW. The antenna is a parabolic sylinder. When the EISCAT UHF radar lost its tristatic capabilities due to interference from GSM mobile phone communication, the receivers in Kiruna and Sodankylä were converted to the frequency of the EISCAT VHF radar. Thus, the EISCAT VHF radar is now able to make tristatic measurements. In this dissertation, data from the EISCAT

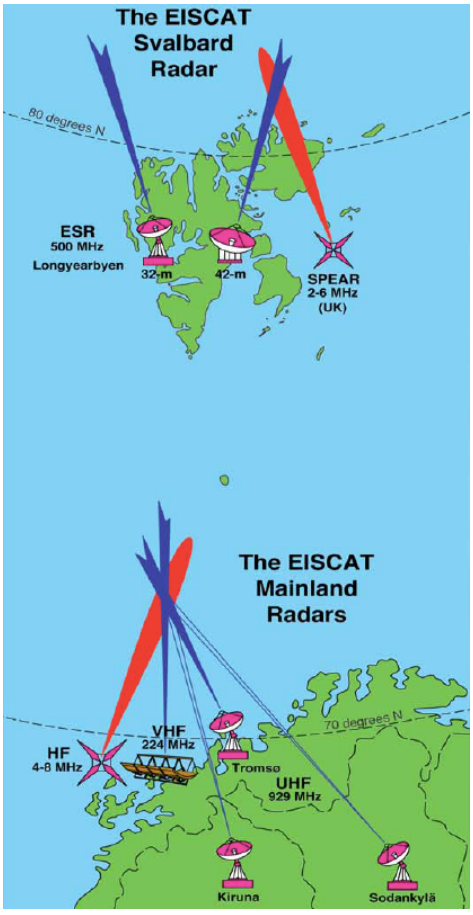

Figure 3.2: Map showing the locations of the EISCAT radars. Please note that the Spear radar does no longer exist.

Figure 3.3: The EISCAT UHF radar. Photo by Henry Pinedo.

Tromsø radars are used in paper II to search for long-term trends, and in paper III to investigate the properties of high-latitude depletion regions.

The EISCAT Svalbard radar (ESR) is located near Longyearbyen, Svalbard, at geographic coordinates 78°09′N and 16°01′E. ESR started its operations in 1996, and transmits with a frequency of 500 MHz and a peak power of 1 MW. It has two parabolic antennas; a 32 m fully steerable dish and a 42 m dish fixed in the direction of the geomagnetic field. A photo of the antennas can be seen in figure 3.4. In this dissertation data from the ESR are used in paper I to evaluate the IRI model, and in paper III to investigate properties of high-latitude depletion regions.

Figure 3.4: The ESR radar. Photo by Njål Gulbrandsen.

Several types of experiments exist for the EISCAT radars. Technical aspects of the EISCAT data such as range resolution, time resolution and which part of the ionosphere it is possible to obtain data from, depend on the chosen pulse code program. For example, as previously mentioned, long pulses will give a better signal-to-noise ratio, but a poorer range resolution. In addition, beam pointing direction and whether the radar should be in a fixed position or a scanning mode have to be determined before running an EISCAT experiment. This means that the technical parameters of the collected data varies considerably. Analysed data from all types of experiments are freely available trough Madrigal. Madrigal is a distributed online database which contains data from a range of different instruments for ionospheric and upper atmospheric research. This includes several incoherent scatter radars, MF radars and Fabry-Perot interferometers among others. In paper I, ESR data were downloaded from Madrigal.

In order to extract plasma parameters from the incoherent scatter radar spectrum, a theoretical spectrum is fitted to the measured spectrum. For EISCAT data, this is usually done using the Grand Unified Incoherent Scatter Design and Analysis

Package (GUISDAP) developed by *Lehtinen and Huuskonen* (1996). GUISDAP is a MATLAB software package designed to analyse incoherent scatter data. As incoherent scatter is a stochastic process, it is necessary to integrate over several radar pulses to obtain a sufficient signal-to-noise ratio. In Madrigal the integration time for the EISCAT data is mostly around 1 minute. In paper II, we used EISCAT data to search for long-term trends in the ionosphere connected to global climate change. As such trends are expected to be very small, a longer integration time was needed to improve the accuracy of the data. For paper II, we therefore used GUISDAP to analyse the raw data with 1 hour integration time. For paper III, we also used GUISDAP to analyse the data with 5 minutes integration time.

3.3 Ionosonde

The ionosonde technique was invented by *Breit and Tuve* (1925), and then further developed, in particular by Sir Edward Appleton, in the following decades. This type of radar works by transmitting short radio pulses into the ionosphere where they are reflected at the height where the plasma frequency equals the transmission frequency. The time between transmission and the return of the reflected signal at a nearby receiver is measured, and the height of the ionospheric layer estimated. As the plasma frequency is proportional to the square root of the electron density, the ionosonde can provide information about the ionsopheric electron density as a function of height.

The basic principle behind the operation of an ionosonde is the Appleton-Hartree equation. This equation describes the refractive index n of a radio wave propagating in an ionized medium and is given by:

$$n^2 = 1 - \frac{X}{1 - iZ - [\frac{Y_T^2}{2(1-X-iZ)}] \pm \sqrt{\frac{Y_T^4}{4(1-x-iZ)^2} + Y_L^2}} \tag{3.4}$$

where

$$X = \frac{\omega_p^2}{\omega^2} \qquad Y = \frac{\Omega_e}{\omega} \qquad Z = \frac{\nu_{en}}{\omega} \qquad \omega_p^2 = \frac{N_e e^2}{\epsilon_0 m_e}$$
$$\Omega_e = \frac{eB}{m_e} \qquad Y_T = \frac{eB_T}{m_e \omega} \qquad Y_L = \frac{eB_L}{m_e \omega}$$

ω_p is the plasma frequency, ω is the angular frequency of the propagating radio wave, Ω_e is the electron gyrofrequency, ν_{en} is the electron-neutral collision frequency, N_e is the electron density, e is the electron charge, ϵ_0 is the permittivity of free space, m_e is the electron mass, and B_T and B_L are the transverse and the longitudinal components of the magnetic field with respect to the direction of the propagation of the wave. If we ignore the Earth's magnetic field and the collisions between electrons and neutrals, equation 3.4 will simplify to:

$$n^2 = 1 - \frac{\omega_p^2}{\omega^2} \tag{3.5}$$

A radio wave transmitted vertically will be reflected when $n^2 = 0$. From equation 3.5 it can be seen that this occurs when the plasma frequency equals the transmission frequency. Typically, the transmission frequency of an ionosonde is swept from approximately 1 to 20 MHz. The time from the signal is transmitted to the signal is received is measured for different frequencies, and from the information contained in the received signal an **ionogram** is produced.

An example of an ionogram from Tromsø is shown in figure 3.5. In Tromsø, there have been ionosonde measurements since the 1930s (*Appleton et al.*, 1937), and the ionosonde at Ramfjordmoen is an important tool to calibrate EISCAT data. This is done by comparing the EISCAT peak density with the peak density from Tromsø ionograms.

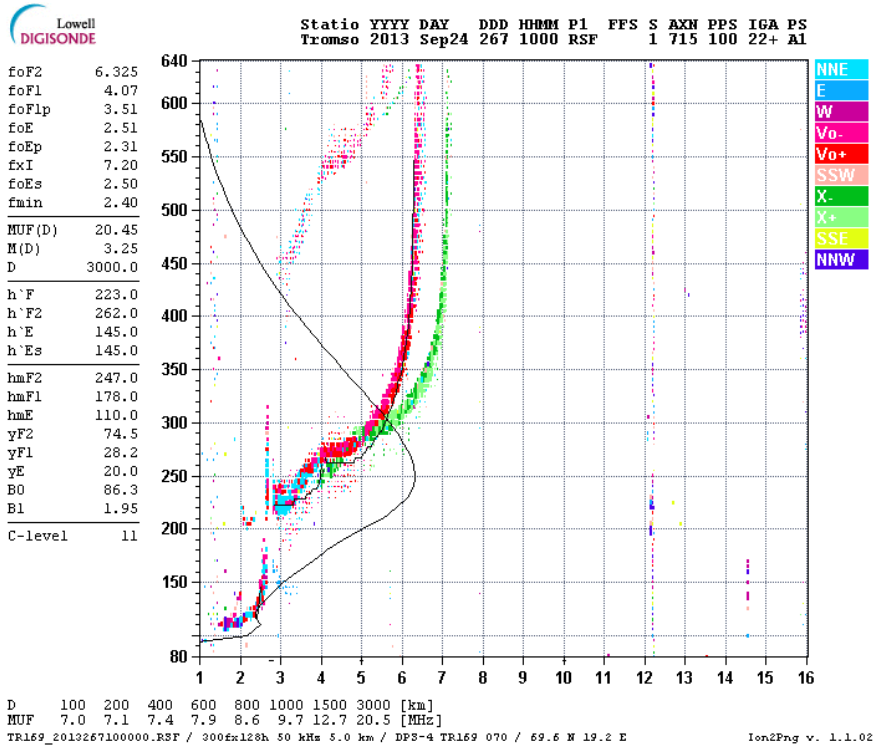

Figure 3.5: Ionogram from Tromsø from 24 September 2013. Virtual height is plotted along the y-axis and frequency along the x-axis.

Today, ionosondes remain an important tool, not only for calibration, but also for investigating the ionosphere. Some of the longest available time-series of ionospheric data come from ionosondes. However, ionosondes also have their limitations. Information about the ionosphere above the peak height of the F-region electron density can not be provided by the ionosonde as the transmitted radiowave is reflected when the plasma frequency is larger than the frequency of the transmitted radiowave. In addition, the ionosonde is not so suitable for D-region studies as low transmission frequencies are needed to get reflections from such low altitudes. During intense ionization in the E-region (sporadic E-layers), information from regions above the E-layer can not be obtained. Furthermore, in the auroral oval, strong absorption in the D-region during interesting events, such as substorms, could prevent the reflection of the signal and no information will be obtained.

Chapter 4

The IRI model

In addition to observations, models are very important for ionospheric studies. Sometimes there are no available measurements of the phenomena or of the region we wish to study, and in such cases models are essential. Models can also be used to perform simulations, which are beneficial for obtaining a better understanding of many plasma processes in the ionosphere. There are in general two main types of models; theoretical models and empirical models. Theoretical models calculate ionospheric parameters using basic plasma physics theory and knowledge about chemistry processes in the upper atmosphere/ionosphere. An example of a theoretical model is the National Center for Atmospheric Research (NCAR) Thermosphere-Ionosphere-Electrodynamics General Circulation Model (TIE-GCM) (e.g. *Qian et al.*, 2009, and references therein). Empirical models are built on observational results. The most widely used model for the ionosphere is the empirical International Reference Ionosphere (IRI) model (*Bilitza et al.*, 2017). In this dissertation we have used data from the EISCAT radars to evaluate the performance of the IRI model at high latitudes in paper I and paper III. The aim of this chapter is to give an introduction to the IRI model.

4.1 What is IRI?

The IRI model was initiated in the late 1960s as a joint project between the Committee on Space Research (COSPAR) and the International Union of Radio

Science (URSI), and today it is the most widely used ionospheric model. For a given location and time, the IRI model can provide information about several plasma parameters, including electron density, ion and electron temperatures and ion composition for altitudes between 60 and 1500 km. The primary data sources for the IRI model are the worldwide network of ionosondes, incoherent scatter radars, satellite and rocket measurements. An annual IRI workshop is held where updates to the model are discussed, and the model is updated as new data become available. By now, only monthly averages are provided, but by assimilation of more data the IRI model might progress into providing daily or hourly averages. An IRI Real-Time model, which will be able to provide real-time space weather information, is currently under development (e.g. *Bilitza et al.*, 2011, 2017).

4.2 The IRI model at polar latitudes

As ionosondes are one of the primary data sources, the IRI model is most accurate at midlatitudes where the station coverage is highest (e.g. *Bilitza and Reinisch*, 2008). At polar latitudes, there are fewer available data sources and the model is therefore not as well suited to represent the ionosphere above approximately 60° latitude. However, improving the representation of the polar ionosphere is an aim for developers of the IRI model. "Representation of the auroral and polar ionosphere in the International Reference Ionosphere" was the topic of the IRI workshop in 2010, which was held during the COSPAR Scientific Assembly (*Bilitza and Reinisch*, 2013). Also the 1994 IRI workshop was dedicated to discussions about the IRI model at high latitudes. Newer versions of the IRI model have improved the representation of the polar ionosphere by including auroral boundaries and storm effects in the auroral E-region (*Bilitza et al.*, 2014).

Some data sources do, however, exist also at polar latitudes. The EISCAT radars have, since the 1980s, provided information about the polar ionosphere. Data from the EISCAT UHF and VHF, together with rocket measurements, have been used to develop the Ionospheric Model for the Auroral Zone (IMAZ) (*McKinnell and Friedrich*, 2006, 2007). IMAZ is a model of the auroral zone D- and E-region, and was included as part of the IRI 2007 model (*Bilitza and Reinisch*, 2008).

Another source of information about the polar ionosphere is satellite data. Both the STORM-E model (*Mertens et al.*, 2013a,b), which describes auroral storm effects, and the model by *Zhang and Paxton* (2008), which is used to represent auroral boundaries, are based on data from satellites. These models were both included in the 2012 version of the IRI model.

4.3 Evaluation of the IRI model at polar latitudes

Although best suited for midlatitudes, the IRI model is also used by several researchers studying the high latitude ionosphere. It is therefore of interest to compare IRI model parameters with observational data from the polar ionosphere. This could help users to identify during which conditions, time of day and season the IRI model works well, and when the model is less accurate and should not be used. It would also be beneficial for developers of the IRI model for identifying areas where the model needs to be improved. In paper I, we therefore decided to compare the IRI model with the electron density from the accumulated database of ESR data, to evaluate the IRI model electron density in the polar cap and cusp region. Our results showed that the IRI model was slightly biased towards an underestimation of the polar cap electron density. Similar results were found when we also compared electron density data from the Tromsø radars with the IRI model. These results were, however, not published. In paper III, we compared both the IRI electron density and ion temperature with data from the ESR radar. We found that the IRI model was not able to reproduce an observed density depletion in the early morning polar cap. In addition, we found that the polar cap ion temperature shows higher diurnal variation than the IRI model ion temperature.

There are also other studies which have compared the IRI model to observational results at high latitudes. For example *Maltseva et al.* (2013) compared observed foF2 with IRI modeled foF2 at 4 high latitude stations and 2 midlatitude stations. They found similar results for the comparison at high latitudes as for the comparison at midlatitudes. *Oyeyemi et al.* (2010) compared hmF2 from 3 high latitude ionosonde stations with the IRI model and found both overestimation and underestimation at different times of day. *Themens and Jayachandran* (2016)

compared the IRI model total electron content (TEC) with measurements from 10 GPS receivers in the auroral zone and polar cap. They found that the IRI model underestimated TEC at high latitudes. From these studies, and from paper I and paper III, we see that the IRI model can both overestimate and underestimate ionospheric parameters in the polar ionosphere. It is therefore important to be careful when using the IRI model at these latitudes, and take into account that the model might overestimate or underestimate the ionosphere depending on time of day, season or solar activity.

Chapter 5

Long-term trends

Ionospheric parameters show significant variability on different time-scales depending on factors such as time of day, season, geomagnetic and solar activity. It is also known that long-term trends can occur in the ionosphere due to for example long-term changes in the geomagnetic field or long-term changes in solar activity (e.g. *Laštovička*, 2005). An important cause of long-term trends in the ionosphere is, however, the anthropogenic emissions of greenhouse gases (e.g. *Laštovička et al.*, 2012). As the EISCAT radars have been operational for several decades, the accumulated database can be used to search for such long-term changes in the ionosphere. One of the key topics and part of the motivation behind this dissertation has been to search for long-term trends in ionospheric parameters using EISCAT data. The purpose of this chapter is therefore to introduce previous research on the topic of ionospheric trends, and how they are connected to our results in paper II.

5.1 Global climate change and the ionosphere

Global climate change is often referred to as "one of the greatest challenges of our time". In their fourth assessment report, the intergovernmental panel on climate change (IPCC) reported an increase of the surface temperature of 0.74°C globally over the last 100 years, but in the Arctic the temperatures in the same time period are increasing almost twice as fast (*IPCC*, 2007). Already *Arrhenius* (1896) made

calculations showing how changes in the atmospheric concentrations of carbon dioxide would cause variations in the temperature of the Earth. Nevertheless, it was not until the 1950s one realized that anthropogenic emissions of CO_2 could become a problem (e.g. *Plass*, 1956). In addition to the increase in the surface temperature, temperatures are increasing in the troposphere, while there is a cooling in the stratosphere and the upper atmosphere (*IPCC*, 2007). *Manabe and Wetherald* (1967) was the first to show that there would be a cooling at altitudes above the troposphere. This cooling is due to increased infrared emissions caused by the increase in CO_2 concentration (*Manabe and Wetherald*, 1975).

Roble and Dickinson (1989) found that a doubling of the concentrations of CO_2 and CH_4 at 60 km altitude from the mean values in the 1950s would cause the mesosphere to cool by 10 K and the thermosphere to cool by 50 K. They also indicated that this upper atmospheric cooling would lead to changes in the ionospheric structure. *Rishbeth* (1990) estimated that a thermospheric cooling of 50 K would lower the F2-layer by 15-20 km and the E-layer by about 2 km. However, *Rishbeth* (1990) found no significant change in the peak electron densities. Further investigations of how global climate change will affect space were made by *Rishbeth and Roble* (1992) using the NCAR Thermosphere/Ionosphere General Circulation Model. They found that a doubling of the CO_2 and CH_4 concentrations would cause a cooling of 40 K in the upper thermosphere and 15-25 K in the lower thermosphere. Furthermore, they found that the neutral gas density will decrease by 20-40% and that the F2-layer will be lowered by about 15 km on average. Using satellite measurements, *Keating et al.* (2000) found that the thermospheric density had declined by approximately 10% over a time period of 20 years.

Shortly after the suggestion that global climate change would lead to ionospheric changes, ionosonde data were investigated to search for trends in the peak heights of the ionospheric layers. Ionosondes were considered important for such studies as they offer some of the longest time-series of ionospheric data available, and can therefore be used to search for long-term trends over several solar cycles. *Bremer* (1992) was the first to publish results after searching for trends in ionosonde data

from mid-latitudes. No significant changes in the peak densities were found, but the F-layer was lowered by about 0.24 km/year. Soon several other studies searching for trends in ionosonde data followed (e.g. *Ulich and Turunen*, 1997; *Bremer*, 1998; *Jarvis et al.*, 1998; *Hall and Cannon*, 2001). However, a lowering of the F-layer was not observed at all ionosonde stations. On the contrary, some ionosonde stations showed a positive trend in the peak height of the F2-layer (hmF2) (e.g. *Bremer*, 1998; *Upadhyay and Mahajan*, 1998). *Cnossen and Richmond* (2008) attributed the discrepancy in the observed trends to secular changes in the Earth's magnetic field. In regions were the changes are large, this will have a significant effect on the F-layer peak height and frequency.

5.2 Trends in incoherent scatter radar data

Ionosondes primarily provide information about peak heights and frequencies (densities), and data from other instruments are therefore needed to obtain a more complete picture of how global climate change affects space. Compared with ionosondes, many of which started their operations during the International Geophysical Year (1957-1958), incoherent scatter radars have shorter time-series available. Nevertheless, the oldest incoherent scatter radars have been operational for several solar cycles, and can provide extensive information about many primary plasma parameters (see chapter 3).

Ulich et al. (1999) were one of the first to investigate the possibility of using incoherent scatter radars to search for long-term trends in the ionosphere. They used 12 years of data from the EISCAT UHF radar to compare with the hmF2 trends they found in Finnish ionosonde data. Results from the EISCAT UHF radar and the Sodankylä ionosonde seemed to be in agreement, however, the relatively short time-series of EISCAT UHF data results in large statistical uncertainties in the trend estimates.

Most of the ionospheric trend studies using incoherent scatter radars have focused on the ion temperature parameter. At mid-latitudes, *Donaldson et al.* (2010) analyzed data from the Saint Santin incoherent scatter radar, covering the years

1966-1987. They found a cooling in the F-region ion temperature, but a warming in the E-region. This warming was explained by subsidence of an overlying warmer atmosphere. At Millstone Hill, *Zhang et al.* (2011) used more than three solar cycles of noontime incoherent scatter radar data and reported a cooling of the ion temperature above 200 km altitude, and a warming below 200 km. This study was extended by *Zhang and Holt* (2013) to also study trends at other local times than noon. At nighttime, they found that the cooling was very weak at altitudes above 350 km. Below 350 km altitude they found a warming trend. Like *Donaldson et al.* (2010), *Zhang et al.* (2011) and *Zhang and Holt* (2013) suggest that this apparent warming at lower altitudes could be caused by subsidence.

Zhang et al. (2016) investigated long-term trends at high-latitudes using data from the Sondrestrom incoherent scatter radar on Greenland and the Poker Flat incoherent scatter radar in Alaska. A cooling of the ion temperature was found above 200 km altitude. Results from Sondrestrom and Poker Flat were compared with results from Millstone Hill. The cooling trend was found to be similar for the three incoherent scatter radars at altitudes between 200 and 275 km. At higher altitudes, the cooling was stronger for higher magnetic latitudes. For Sondrestrom the cooling was reduced above 425 km altitude at daytime, and above 325 km at nighttime. Using EISCAT UHF from October 1981 until May 2013, *Ogawa et al.* (2014) found a cooling of the ion temperature between 200 and 380 km altitude. After removing the influence of solar activity, they found a trend of -0.5 to -1.5 K/year at these altitudes. Above 400 km altitude, they found that the cooling was reduced to near zero, and at the highest altitudes there appeared to be a warming trend. At these altitudes the estimated trend in ion temperature were -0.5 to 1 K/year.

Besides ion temperature, there are many other parameters that can be derived from EISCAT data and used for trend studies. *Vickers et al.* (2014) derived atmospheric oxygen density at 350 km altitude from 13 years of ESR data. The purpose of this study was to investigate how solar activity affects the polar cap neutral density. In addition, they checked if it was possible to use the ESR data to search for trends in the thermospheric density. They found an apparent decline of a few percent in the thermospheric density, but this was not statistical significant. To derive a

definitive trend, *Vickers et al.* (2014) concluded that a longer data set is needed. In paper II, *Bjoland et al.* (2017a) searched for trends in the peak height of the Hall conductivity and in the ion temperature at 110 km altitude using data from the EISCAT UHF radar. No significant trend in the peak height of the Hall conductivity was found. The ion temperature at 110 km altitude showed a cooling trend of -1 K/year after the removal of the influence of solar activity and solar zenith angle. However, the results indicated that other parameters than solar activity and solar zenith angle also cause significant variations in the ion temperature. An improved understanding of the causes of the observed variations in the ion temperature at 110 km altitude is therefore necessary to derive a conclusive trend.

5.3 Other examples of trend studies from polar latitudes

In addition to incoherent scatter radars, other instruments have been used to investigate high-latitude trends in the ionosphere and upper atmosphere. In this section, a few examples of studies from polar latitudes will be presented. Ionosondes have already been mentioned in section 5.1. *Hall et al.* (2011) searched for trends in the E-region peak height and critical frequency using data from the Tromsø ionosonde covering the years 1948-2011. They found a significant decrease in both parameters. *Roininen et al.* (2015) investigated the hmF2 trend using data from the Sodankylä ionosonde covering the years 1957-2014. They found that through the observation period, the F-layer have been lowered by almost 30 km. The F-layer was observed to decrease more rapidly during the most recent time period (1990-2010).

Holmen et al. (2014) studied the trend of the hydroxyl airglow winter temperature using a 30 year long (1983-2013) data set from a 1 m Ebert-Fastie spectrometer located on Svalbard. They measured the trend to be -0.2±0.5 K/decade. *Holmen et al.* (2016) investigated the neutral temperature trend at 90 km altitude above Tromsø using data from the Nippon/Norway Tromsø Meteor Radar covering the time period from November 2003 to October 2014. The overall temperature trend was found to be -2.2±1 K/decade. However, during winter the trend was shown to be much stronger than during summer (-11.6 K±4.1 K/decade for winter and -0.3 K±3.1 K/decade for summer). *Hall et al.* (2016) used medium frequency radars

in Tromsø and in Saskatoon to study trends in turbopause altitude from both polar and mid-latitudes. In Tromsø, data covering the time period from January 1999 until October 2015 were used to estimate the turbopause trend. They found a positive trend of 2.5±0.3 km/decade in the turbopause height during summer, but no significant change during winter months. Data from the mid-latitude station in Saskatoon did not show any trend in any season.

Both the studies using incoherent scatter radars and studies using other types of instruments show that there are several challenges when it comes to determining long-term trends at polar latitudes. These challenges include sparse data sets, high variability in the parameters studied and relatively low range resolution in the EISCAT data. In addition, the EISCAT F-region data from before 2001 have an even poorer range resolution because long pulse codes were used. The new radar facility, EISCAT_3D, which will be built in Skibotn, near Tromsø, is expected to be able to solve some of these problems. The new radar system will consist of a core site in Skibotn with both transmitter and receiver capabilities, as well as four additional receiver sites located in northern Norway, Sweden and Finland. Each of the sites will consist of a phased array antenna field, which will be able to provide measurements with much better range resolution compared with the current radar system. In addition, the new radar system will provide continuous measurements of the ionosphere with an improved time resolution.

Chapter 6

Summary of papers

Paper I

L. M. Bjoland, V. Belyey, U. P. Løvhaug, and C. La Hoz, **"An evaluation of International Reference Ionosphere electron density in the polar cap and cusp using EISCAT Svalbard radar measurements"**, *Annales Geophysicae*, **34**, 751-758, (2016), doi: 10.5194/angeo-34-751-2016.

The International Reference Ionosphere (IRI) model is an empirical model widely used for ionospheric research. Although the model is known to perform best at mid-latitudes, it is also much used at higher latitudes. In order to evaluate the IRI model at high latitudes during various conditions, we compared IRI electron density in the ionospheric F-region with measurements from the EISCAT Svalbard radar. Our results showed that the IRI model is biased towards an underestimation of the electron density in the polar cap region. This underestimation is clearest at nighttime and during solar maximum. In the phase where the solar activity declines towards solar minimum, the IRI model is overestimating the electron density. The IRI model was also found to overestimate the peak height of the F-layer during all parts of the solar cycle. By identifying conditions and altitudes when the IRI model has difficulties reproducing the high-latitude electron density, our results could be useful for further improvement of the IRI model.

Paper II

L. M. Bjoland, Y. Ogawa, C. Hall, M. Rietveld, U. P. Løvhaug, C. La Hoz and H. Miyaoka, **"Long-term variations and trends in the polar E-region"**, *Journal of Atmospheric and Solar-Terrestrial Physics*, **163**, 85-90, (2017), doi: 10.1016/j.jastp.2017.02.007.

Upper atmospheric cooling is expected to lead to changes in the ionosphere. To detect such changes, it is necessary to have a good understanding of how the ionosphere varies according to various factors such as geomagnetic and solar activity, season and time of day. More than 30 years of data from the EISCAT Tromsø radars were used to investigate the long-term variations of conductivity and ion temperature in the E-region around noon. The aim of this study was twofold: to contribute to the understanding of how these parameters vary during different conditions and to search for trends in these parameters. Results from this study confirm that both ion temperature and Hall conductivity depends strongly on solar zenith angle. A weak descent was observed in the peak height of the Hall conductivity, but this was, however, within the standard deviations of the averaged peak heights. The ion temperature showed signs of a cooling trend, but a better understanding of the factors affecting the ion temperature is necessary to derive a conclusive trend.

Paper III

L. M. Bjoland, Y. Ogawa, and U. P. Løvhaug, **"High-latitude depletion regions and their dependence on geomagnetic activity"**, submitted to *Journal of Geophysical Research Space Physics*, (2017).

In this work we used the EISCAT radars in Tromsø and in Longyearbyen, Svalbard to investigate electron density depletion regions at polar latitudes. In particular, we were interested in looking into how geomagnetic activity affects such depletion regions, and to compare the diurnal electron density variations in the polar cap

(Svalbard) and the auroral zone (Tromsø) ionosphere. We found that a depletion region existed in the morning sector of the polar cap, and that this depletion region expands as geomagnetic activity increases. This depletion region could not be seen in the Tromsø UHF data. An increase in the ion temperature occurs at the same time as the electron density depletion. This suggests that the formation of the electron density depletion might be connected to ion frictional heating. Furthermore, a comparison with the IRI model showed that the IRI model is not able to reproduce the observed depletion region, nor is it able to reproduce the diurnal variations observed in the ion temperature.

Chapter 7

Concluding remarks and future work

In this chapter, concluding remarks are given and future work is described. In section 7.1 we summarize the most important conclusions from each of the papers included in the dissertation. In section 7.2 some of the unanswered questions which we would like to work with in the future are presented.

7.1 Concluding remarks

The topic of this dissertation has been variations of plasma parameters in the polar ionosphere. Both natural changes, such as diurnal, seasonal and solar cycle variations, and long-term changes caused by anthropogenic emissions of greenhouse gases have been investigated. Primary plasma parameters obtained from the EISCAT radars, or parameters derived from them, have been studied to investigate how various kind of changes in the polar ionosphere have affected them. A comparison with the IRI model was done to evaluate the performance of the model during different conditions. A summary of the main conclusions of the papers are as follows:

- In paper I, the F-region electron density in the polar cap and cusp, obtained by the ESR, was studied. It was shown how the electron density varies

with time of day, season, and solar cycle. The purpose of this study was to investigate how well the IRI model reproduces the polar cap ionosphere during different conditions. The results of this comparison showed that the IRI model is biased towards an underestimation of the electron density in the polar cap and cusp. How well the IRI model is able to represent the polar ionosphere varies according to time of day, season and solar cycle. The model faces the greatest challenges at nighttime and during solar maximum.

- In paper II, the Hall conductivity was derived from the Tromsø UHF electron density. Variations in the E-region Hall conductivity and its peak height and ion temperature, according to solar activity and season, were studied. It was confirmed that these parameters show strong seasonal variations, and some weaker variations caused by solar activity. An attempt to derive long-term trends in the Hall conductivity peak height and the ion temperature at 110 km did not provide any conclusive trend. A weak descent of -0.18±0.20 km/decade was seen in the peak height, but this was within the error bars of the averaged peak heights. A cooling of -1.00±0.59 K/year was found in the ion temperature, but our results showed that a better understanding of the mechanisms behind the variations observed in the ion temperature is needed before a conclusive trend can be found.

- In paper III, depletion regions in the polar F-region were studied, using electron density and ion temperature data from the ESR and the UHF radars. A depletion region was seen in the early morning in the ESR data, and the variations of this depletion region with respect to geomagnetic activity were investigated. It was found that the observed depletion region expanded as the geomagnetic activity increased. Furthermore, the ion temperature measurements suggest that the mechanism behind this depletion region might be connected to ion frictional heating. A comparison between the EISCAT data and the IRI model revealed that the IRI model was not able to reproduce this depletion region.

7.2 Future work

In paper I, we compared the IRI model with ESR electron density measurements. As the IRI model is the most widely used model for ionospheric studies, it is important that it represents the ionospheric conditions as accurately as possible. In addition to electron density, the IRI model is also able to provide other ionospheric parameters, such as ion and electron temperatures and ion composition. A possible expansion of paper I could therefore be to include a comparison between the IRI model and other EISCAT parameters such as electron and ion temperatures. In addition, measurements from the EISCAT Tromsø site could be included to obtain a more comprehensive view of how the IRI model is able to reproduce the polar ionosphere.

In paper II, we found that in addition to solar activity and solar zenith angle, it is likely that also other parameters contribute to the observed ion temperature variations. To be able to find conclusive long-term ion temperature trends, an improved understanding of the mechanisms behind these variations must be achieved. One possible mechanism that could cause such variations is atmospheric gravity waves. It has been suggested that long-term changes in gravity wave activity may cause thermospheric cooling (*Oliver et al.*, 2013). Therefore, as a continuation of the work done in paper II, we would like to investigate how this wave activity affects upper atmospheric trends. Furthermore, we would like to compare the observational results from the EISCAT radars with results from simulations using the Ground-to-Topside Model of Atmosphere and Ionosphere for Aeronomy (GAIA) (*Jin et al.*, 2011). This could help us in identifying driving mechanisms behind the observed trends.

In paper III, high-latitude depletion regions were studied and a depletion region was observed in the early morning sector of the ESR data. Future studies are necessary as the scope and the physical mechanisms behind the formation of such depletion regions are not yet fully understood. A clear understanding of these depletion regions are important since our use of space is growing and space weather and electron density variations might affect satellites and their

signals. In a future study it would therefore be interesting to further explore the depletion region observed in paper III. For example, *Ishida et al.* (2014) investigated the occurrence rate of the ionospheric trough using the Tromsø UHF radar. It would be interesting to conduct a similar study using the ESR radar to obtain further information about the depletion region observed in this study.

The polar ionosphere is a dynamic system where changes occur on a multitude of time- scales. Lack of data sources from polar latitudes (compared with the amount of available data sources from midlatitudes) has been a challenge for obtaining a good understanding of the dynamics at these high latitudes. New technology and instrumentation make it possible to improve our understanding of this region. In June 2017, the EISCAT Scientific Association announced that they will start to build the new EISCAT_3D radar in Skibotn. EISCAT_3D will have the capability of making measurements of the high-latitude ionosphere with much better time and space resolution than provided by the present system. This would provide us with high-quality data which could be used to improve our understanding of the dynamic polar ionosphere.

Chapter 8

Publications

Paper I:
An evaluation of International Reference Ionosphere electron density in the polar cap and cusp using EISCAT Svalbard radar measurements

L. M. Bjoland, V. Belyey, U. P. Løvhaug, and C. La Hoz, *Annales Geophysicae*, **34**, 751-758, (2016), doi: 10.5194/angeo-34-751-2016.

Ann. Geophys., 34, 751–758, 2016
www.ann-geophys.net/34/751/2016/
doi:10.5194/angeo-34-751-2016

Annales Geophysicae
Open Access
EGU

An evaluation of International Reference Ionosphere electron density in the polar cap and cusp using EISCAT Svalbard radar measurements

Lindis Merete Bjoland, Vasyl Belyey, Unni Pia Løvhaug, and Cesar La Hoz

Department of Physics and Technology, University of Tromsø – The Arctic University of Norway, Tromsø, Norway

Correspondence to: Lindis Merete Bjoland (lindis.m.bjoland@uit.no)

Received: 22 June 2016 – Revised: 22 August 2016 – Accepted: 30 August 2016 – Published: 13 September 2016

Abstract. Incoherent scatter radar measurements are an important source for studies of ionospheric plasma parameters. In this paper the EISCAT Svalbard radar (ESR) long-term database is used to evaluate the International Reference Ionosphere (IRI) model. The ESR started operations in 1996, and the accumulated database up to 2012 thus covers 16 years, giving an overview of the ionosphere in the polar cap and cusp during more than one solar cycle. Data from ESR can be used to obtain information about primary plasma parameters: electron density, electron and ion temperature, and line-of-sight plasma velocity from an altitude of about 50 and up to 1600 km. Monthly averages of electron density and temperature and ion temperature and composition are also provided by the IRI model from an altitude of 50 to 2000 km. We have compared electron density data obtained from the ESR with the predicted electron density from the IRI-2016 model. Our results show that the IRI model in general fits the ESR data well around the F2 peak height. However, the model seems to underestimate the electron density at lower altitudes, particularly during winter months. During solar minimum the model is also less accurate at higher altitudes. The purpose of this study is to validate the IRI model at polar latitudes.

Keywords. Ionosphere (polar ionosphere)

1 Introduction

Electron density in the polar cap F-region ionosphere is produced by solar extreme ultraviolet radiation, transport of plasma density structures from lower latitudes and particle precipitation and is reduced by recombination and transport to lower latitudes. The solar wind has a significant influence on the dynamics of the high-latitude ionosphere as it controls the electrodynamics and therefore transport by $\boldsymbol{E} \times \boldsymbol{B}$ plasma drift and by particle precipitation. Thus the high-latitude ionosphere is a highly variable region where structures form, recombine and are transported in and out in response to transient changes in the solar wind and/or the interplanetary magnetic field.

Plasma density structures in the high-latitude F region are transported anti-sunward across the polar cap and sunward in the auroral zone due to electric convection (e.g., Cowley and Lockwood, 1992). This transport can increase the electron density in the nightside significantly when structures produced by solar extreme ultraviolet radiation in the sunlit ionosphere follow the convection lines into the polar cap. As an example, plasma originating at midlatitudes can be transported to high latitudes and into the polar cap in a form of a tongue of ionization which greatly enhances the plasma density in the polar cap, cusp and auroral zone (e.g., Foster et al., 2005). Tongues of ionization can also be segmented into 100–1000 km sized islands of enhanced electron density, called polar cap patches (e.g., Lockwood and Carlson, 1992; Zhang et al., 2013). The patches are transported over the polar cap following the convection pattern.

In addition to transport of solar-produced plasma from lower latitudes, soft particle precipitation is an important

source of F-region plasma density irregularities at high latitudes (e.g., Kelley et al., 1982). Soft particle precipitation in the cusp region where particles precipitate directly from the magnetosheath can produce polar cap patches that can be convected over the polar cap (e.g., Walker et al., 1999; Oksavik et al., 2006; Goodwin et al., 2015). As a result of plasma transport and particle precipitation, the high-latitude F region ionosphere is nonuniform and highly dynamic. This is a challenge for models aiming to accurately represent the high-latitude ionosphere.

The International Reference Ionosphere (IRI) model is widely used for ionospheric and magnetospheric research, also at high latitudes. IRI is an empirical model which provides monthly averages of ionospheric parameters from an altitude of 50 to 2000 km (Bilitza, 1990, 2001). Among the data sources used to build the IRI model are incoherent scatter radars (ISRs), the ISIS and Alouette topside sounders, rocket and satellite observations, as well as the worldwide network of ionosondes. As ionosondes are an essential data source for the IRI model, the IRI model is known to be less accurate at high and low latitudes, where the ionosonde coverage is lower compared to midlatitudes (e.g., Bilitza and Reinisch, 2008).

In the present study we use ISR data from the EISCAT Svalbard radar (ESR), covering the polar cap and cusp, to evaluate the IRI model-predicted electron density in the F region. As the radar started its operations in the 1990s, the accumulated database now contains data from more than one solar cycle. Long time series of ionospheric data are essential when the aim is to study the performance of the IRI model during different diurnal, seasonal and solar activity conditions. Using the ESR data allows us to evaluate the IRI model in the region where the model is known to be less accurate under various conditions.

Previous studies have also used observational data to evaluate the IRI model (e.g., Themens et al., 2014; Wichaipanich et al., 2013; Kim et al., 2011; Chuo and Lee, 2008; Lei et al., 2006; Zhang and Holt, 2004), but few of these have evaluated the model at latitudes as high as the auroral zone or the polar cap, or with long enough time series to evaluate the model at different parts of the solar cycle. Brum et al. (2011) and Lei et al. (2006) used data from ISRs in their studies. Brum et al. (2011) used Arecibo ISR data from experiments performed between 1985 and 2009, covering three different solar cycles, to evaluate the IRI-predicted F2 layer critical frequency (*fo*F2) and height (*hm*F2) at midlatitudes. They found an overestimation of *fo*F2 at day and an underestimation at night. For *hm*F2 they found an underestimation, especially during high solar activity. However, after applying a correction for solar activity, they found that the IRI model reproduced the seasonal variation well. Lei et al. (2006) compared ISR data from Millstone Hill, at midlatitudes, and ESR, in the polar cap, with the IRI-2001 model. They used the ISR data to evaluate the IRI electron density and plasma temperature profiles. As expected due to the poor data coverage at high latitudes, they found that the model performed best at midlatitudes. Lei et al. (2006) used 1-month-long data from October 2002 from Millstone Hill and the ESR and therefore did not study any solar cycle or seasonal variations.

Several studies have compared ionosonde data with the IRI model. At midlatitudes, Kim et al. (2011) compared 10 years of *Nm*F2 and *hm*F2 data from a digisonde located at the Korean Peninsula with the IRI-2007 model. They looked at different diurnal, seasonal, solar activity and geomagnetic conditions and found that although there was good agreement between the observed and IRI-predicted *Nm*F2, there were significant differences between the model and observed *hm*F2 during midnight, especially during high solar activity. At auroral latitudes, Oyeyemi et al. (2010) compared *hm*F2 observed at three different ionosonde stations with the *hm*F2 values predicted by IRI-2001 for three separate years at different parts of the solar cycle. They found the best agreement when the solar activity was high.

In a study by Themens et al. (2014) data from four ionosonde stations located within the polar cap were used to evaluate the *hm*F2, peak density (*Nm*F2), M(3000)F2 and the bottomside thickness parameter B0 predicted by the IRI-2007 model during the latest extended solar minimum from 2008 to 2010. In addition, data from the Resolute Advanced Modular ISR were used to evaluate the IRI-predicted topside thickness. They evaluated the IRI peak height and density, and topside and bottomside thickness and found differences which they attributed to errors in the modeling of the IRI M(3000)F2 factor and poor representation of diurnal and seasonal variability.

Although Lei et al. (2006), Oyeyemi et al. (2010) and Themens et al. (2014) have compared the IRI model with high-latitude data, such comparisons have mainly been made at midlatitudes. It is therefore highly relevant to evaluate the IRI model for the high-latitude region, and in this study we compare the IRI model with the ESR data from the polar cap and cusp.

2 Data and methodology

The EISCAT Svalbard radar, located at 78.15° N, 16.02° E (geographic coordinates) and 75.43° N, 110.68° E (geomagnetic coordinates), is one of three incoherent scatter radar systems operated by the EISCAT Scientific Association. In addition to the ESR, an ultra-high-frequency system and a very-high-frequency system are located near Tromsø, Norway, with additional receiver systems in Kiruna, Sweden, and Sodankylä, Finland. The radars are usually operated in a campaign mode, and the data are therefore not continuous. Typically, ESR operates around 1000–2000 h a year, but as part of an IPY-ICESTAR project the ESR was operated nearly continuously from March 2007 to February 2008. Data from ESR can be used to obtain information about primary plasma parameters: electron density, electron and ion temperature, and line-of-sight plasma velocity (many other

parameters can be derived from them) from an altitude of about 50 and up to 1600 km. The complete data set therefore provides a comprehensive overview of the ionosphere in the polar cap and cusp during a range of different diurnal, seasonal, geomagnetic and solar activity conditions.

To get access to the complete ESR data set, we have used the Madrigal database, which is an archive of data from a range of different upper atmosphere instruments. Nearly all the experiments since the EISCAT radars were put into operation are available through Madrigal. All ESR data used in this study have been retrieved from the EISCAT Madrigal database.

The Madrigal data have been collected from different experiment modes with different time and altitude resolution and altitude span. As the ESR measurements are not continuous and have different time and altitude resolution, the data have been integrated in 3 h daily intervals for 3-month seasonal periods in each 20 km altitude bin as shown in Fig. 1. The seasonal binning is based on the equinoxes and solstices. This means that spring includes February, March and April, summer includes May, June and July, autumn includes August, September and October and winter is November, December and January (consecutive months). Erroneous data that sometimes appear in Madrigal were filtered out of the integration. The filtering excluded records with electron densities lower than 10^8 m^{-3} and records with electron densities higher than 10^{12} m^{-3}. An exception was made for the upper electron density limit during solar maximum years 1999, 2000, 2001 and 2002. Due to the higher solar activity the filtering during these years only excluded records with electron densities higher than 10^{13} m^{-3}.

The ESR results were compared with the IRI-2016 model. ESR has two parabolic antennas: a 42 m diameter antenna fixed in the field-aligned direction and a fully steerable antenna with a diameter of 32 m. In order to make the comparison between the IRI model with the ESR data as accurate as possible , ESR data were only used if the elevation angle was larger than 75°. The IRI model is updated as new data become available, and in this study the latest IRI-2016 model is used. Standard options were used for the IRI model. An IRI profile was generated for each unique time where an ESR profile were used. The IRI profile covered altitudes between 200 and 500 km with a step size of 20 km. Each IRI profile therefore had one value in each 20 km altitude bin. Since seasonal averages were used for the ESR data, and not monthly averages as produced by IRI, the IRI-produced electron densities were also binned and averaged according to season and 3 h daily intervals.

To further investigate the observed difference in the electron densities from ESR measurements and IRI-produced electron densities, the total electron content (TEC) and *hm*F2 parameters were also estimated. The TEC calculation was done by integrating the electron density over each altitude bin. ESR TEC was only calculated for seasons and daily time intervals when there were data in each altitude bin to ensure that ESR TEC and IRI TEC could be compared.

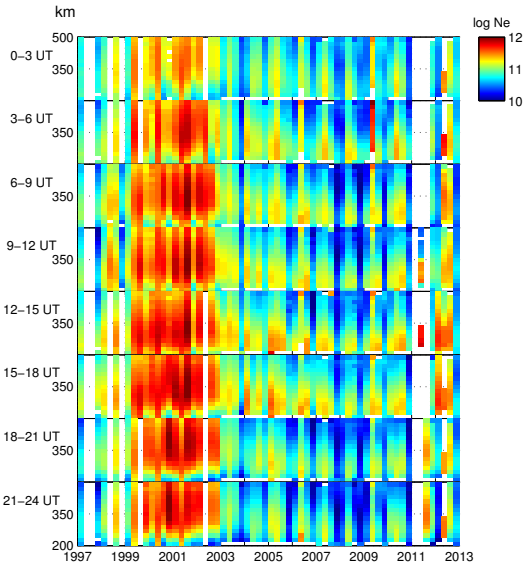

Figure 1. Altitude profiles of electron density (log10 N_e, m^{-3}) measured by ESR and integrated over 3 h in a day for 3 months (spring, summer, autumn, winter). Panels correspond to the 3 h integration intervals.

ESR *hm*F2 was estimated for each profile in a way similar to Vickers et al. (2014). Cubic spline interpolation was used to set a fixed distance of 10 km between each point in the profile. The maximum electron density was then found in each interpolated profile, and a second-degree polynomial was fitted to five points in the peak area centered around the maximum. The maximum of the fitted polynomial was then used as an estimate of the *hm*F2. To ensure a sufficient number of interpolation points around the maximum, we searched for *hm*F2 in the altitude range 180 to 500 km. Profiles from which it was difficult to extract any clear maximum were excluded. This filtering excluded ESR profiles in which the maximum was found in the lowest or highest range gate and profiles in which the electron density doubled between two adjacent points (possible outliers). All the estimated *hm*F2s were then categorized by season and 3 h time intervals, and the average *hm*F2 in each bin was found.

3 Results and discussion

3.1 Comparison of the ratio ESR / IRI

Figure 2 shows a histogram of how all the ESR data compare with the IRI model. This is the distribution of the en-

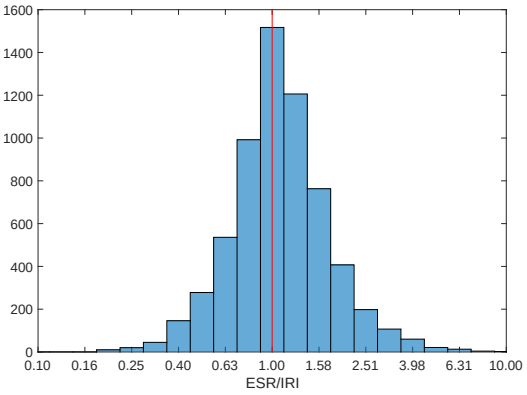

Figure 2. Histogram showing the distribution of all the data without binning. The x axis shows the ratio between ESR data and the IRI model, the y axis the number of data points.

tire database without binning, but after the electron densities outside the range 10^8 to 10^{12} m^{-3} have been excluded. If the IRI model had been a perfect fit to the ESR data, all the data would have been located in the bar where the ratio is 1, as indicated by the red line. From Fig. 2, it is apparent that the model both overestimates and underestimates the electron density as measured by the radar; however, the model is significantly biased towards an underestimation.

Figure 3 shows the ratio between the ESR-measured electron density and electron density produced by IRI in each bin. As for Fig. 1, the eight top panels each represent a 3 h integration interval. The bottom panel displays the sunspot number, which shows the solar cycle variation. The four columns in each year represent the seasons in the order of spring, summer, autumn and winter.

During solar maximum (1999–2002), the red color in Fig. 3 shows that the IRI model clearly underestimates the electron density for altitudes below the F2 peak. The underestimation is visible in all seasons and at any time of the day, but largest at nighttime and during winter. For example, during winter in 2001 and 2002, the ratio of ESR to IRI electron density is 2.5 or above for all altitudes between 200 and 500 km in the time interval 18:00–21:00 UT. During summer, in the same time interval, the agreement is much better between the IRI model and the ESR data. There is still some underestimation, but this is mainly concentrated to below 260 km altitude, and the ratio of ESR to IRI electron density is 2 or less. Also at higher altitudes, above the F2 peak, the IRI model underestimates the electron density. However, the ratio is less for this high-altitude underestimation and it usually covers a smaller altitude range than the underestimation below the F2 peak.

As the solar activity declines towards solar minimum, the situation changes. Compared to the solar maximum, there is

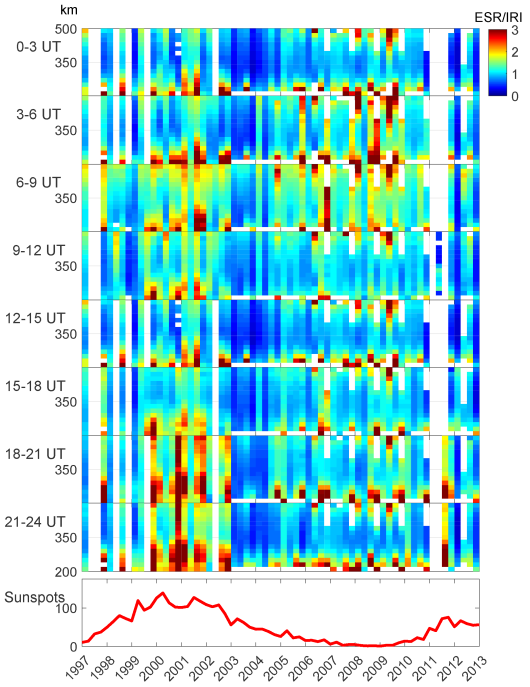

Figure 3. Altitude profiles of the ratio between ESR and IRI electron densities. The eight top panels correspond to the different 3 h integration intervals. The last panel shows the 3-month averaged sunspot number. The four columns for each year represent the seasons in the order of spring, summer, autumn and winter.

better agreement between the IRI model and the ESR data at the altitudes below and above the F2 peak area during the years 2003–2004. However, the dark blue color in Fig. 3 shows that for these years the IRI model overestimates the electron density in the area around the peak density.

During the extended solar minimum (2006–2010) the situation becomes more similar to the solar maximum years. The IRI model fits the ESR data best in the area around the peak height but underestimates the electron density below ∼ 260 km and above ∼ 440 km altitude. At altitudes above ∼ 440 the underestimation is slightly stronger during solar minimum than during solar maximum. On the other hand, below the peak height the altitude range where the model underestimates the electron density is smaller than during solar maximum, particularly at nighttime.

High electron density gives a larger signal-to-noise ratio in the radar measurements. We therefore expect more outliers when the electron density is low. To ensure that the larger number of outliers does not affect the results, the electron density distribution at different parts of the solar cycle was examined. Based on this examination, the lower limit on

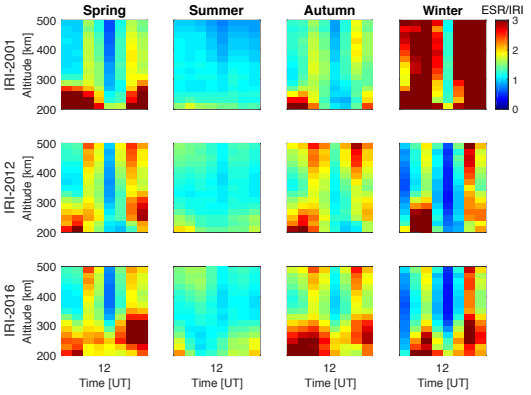

Figure 4. Altitude profiles of the ratio between ESR and IRI electron densities for three different versions of the IRI model (IRI-2001, IRI-2012 and IRI-2016) in 2001. The data have been binned according to season, as indicated, and as daily 3 h averages. The rows show how the IRI-2001, IRI-2012 and IRI-2016 models reproduce the polar ionosphere during 2001 respectively.

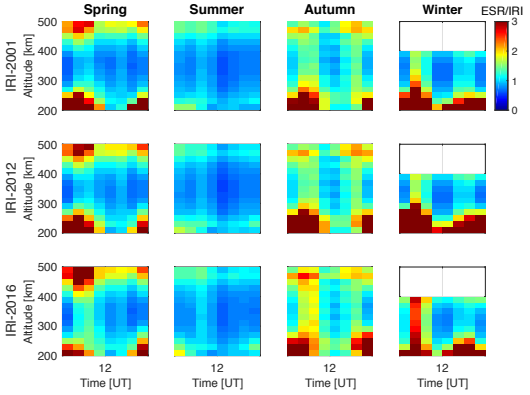

Figure 5. Same as Fig. 4, but for 2008, in the extended solar minimum, instead of 2001.

electron density was set to $10^8\,\mathrm{m}^{-3}$ and the upper limit to $10^{13}\,\mathrm{m}^{-3}$ during solar maximum and $10^{12}\,\mathrm{m}^{-3}$ during other parts of the solar cycle. Also, at higher altitudes the electron density is lower, increasing the risk of erroneous data entering the analysis due to the lower signal-to-noise ratio. Therefore, it was decided to only use EISCAT data from below 500 km where the signal-to-noise ratio is in general sufficient. An exception is winter data during solar minimum, where data above 400 km can be unreliable. These data have therefore been removed from Figs. 2–5.

3.1.1 Comparison with previous versions of the IRI model

A new topside model, the NeQuick model (e.g., Radicella, 2009), has been used as the standard option by the IRI model since IRI-2007. Coïsson et al. (2006) compared the NeQuick and the IRI topside model with topside profiles from the ISIS-2 satellite and found that the NeQuick topside model provides a better representation of the topside ionosphere than the IRI topside model. IRI-2012 also introduced a new model for bottomside thickness, ABT-2009 (Altadill et al., 2009), which has since been used as the standard option (Bilitza et al., 2014). As the IRI model offers several options to choose from, including those used as standard options in the previous versions of the IRI model, it is of interest to investigate whether another choice of options would give a better agreement with the ESR electron density. Therefore, we have chosen to also compare earlier versions of the IRI model with the ESR electron density to check whether a different set of standard options would give a better representation of the electron density in the high-latitude ionosphere.

Figure 4 shows the ratio ESR electron density over IRI, for the IRI-2001, IRI-2012 and IRI-2016 during 2001 (solar maximum). Above ∼ 440 km the IRI-2001 model represents the polar cap ionosphere during spring and summer slightly better than the IRI-2012 and IRI-2016 model. The median ratio over the spring and summer plots for altitudes 440–500 km is ∼ 1.35 and ∼ 1.37 for the IRI-2012 and IRI-2016 models, respectively, but only ∼ 0.97 for the IRI-2001 model. A different situation is seen during winter where IRI-2012 and IRI-2016 clearly perform better than the IRI-2001 model. In general, the performance of the IRI-2012 and IRI-2016 is similar, but some differences can be observed. For example, both models underestimate the electron density below 300 km, but the underestimation is stronger for the new IRI-2016 model, particularly around the equinoxes where the median ratios are ∼ 1.81 and ∼ 2.29 for the IRI-2012 and IRI-2016 model, respectively.

Figure 5 is similar to Fig. 4 but compares the performance during a year in the extended solar minimum (2008). Here, all three versions of the IRI model show similar behavior. However, in contrast to the situation during solar maximum, the IRI-2016 model is slightly better at reproducing the ionosphere below 300 km during the extended solar minimum than IRI-2012. Below 300 km the median ratio over all seasons is ∼ 1.39 for IRI-2012 and ∼ 1.31 for IRI-2016. Also the mean ratio over the plot for bins below 300 km confirms that the underestimation is stronger for the IRI-2012 model than for IRI-2016. The mean ratio is ∼ 3.12 for IRI-2012 and ∼ 1.87 for IRI-2016.

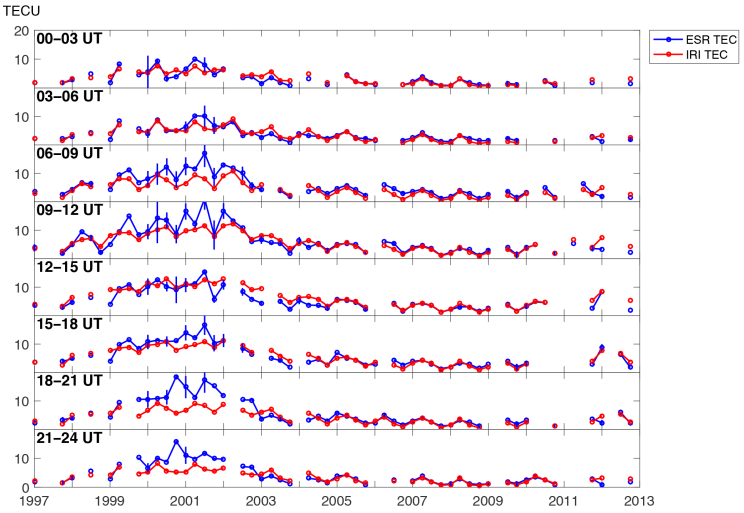

Figure 6. Total electron content from ESR (blue) and IRI model (red) given in TEC units (TECU). Each panel corresponds to a 3 h integration bin, and each year contains four seasonal bins (spring, summer, autumn and winter).

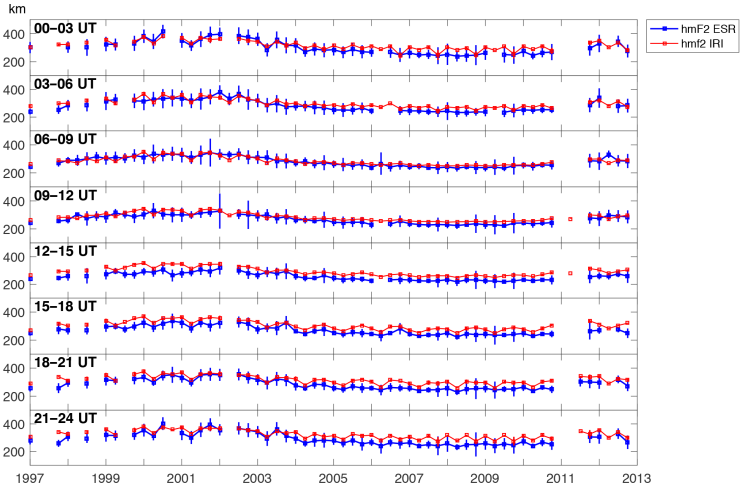

Figure 7. The height of the F2 peak from ESR (blue) and IRI model (red). Each panel corresponds to a 3 h integration bin, and each year contains four seasonal bins (spring, summer, autumn and winter). Error bars correspond to 1 standard deviation.

3.2 Comparison of the total electron content (TEC)

From the binned ESR data the TEC between 200 and 500 km was also calculated and a comparison between ESR TEC and IRI TEC is shown in Fig. 6, where TEC is given in TEC units ($1\,\mathrm{TECU} = 10^{16}$ electrons m^{-2}). Figure 6 shows that the TEC is best reproduced during the solar minimum and that the IRI model underestimates the TEC during the solar maximum. The IRI model reproduces TEC well during the extended solar minimum but underestimates the TEC during solar maximum. Although the general tendency is that IRI-TEC underestimates the ESR-TEC, there are also examples of IRI overestimating the electron density. For example in spring 1999, one can observe an overestimation of TEC in Fig. 6, consistent with the overestimation of the electron density at altitudes around the peak height and above, as seen in

Fig. 3. The underestimation observed during the solar maximum 2001–2002 is consistent with the results Themens and Jayachandran (2016) found using Canadian GPS-TEC data during the most recent solar maximum. They attributed this underestimation to the topside thickness parameterization in the IRI model.

3.3 Comparison of the height of the maximum density in the F2 layer

Also the heights of the F2 layer peak (*hm*F2) as given from the IRI model were compared with *hm*F2 calculated from the ESR data. Both the estimated ESR *hm*F2s and the *hm*F2s from the IRI model were binned according to season and time of day, and the median in each bin was found. For the IRI model, we obtained the *hm*F2 from all the times an ESR profile was available. The results are seen in Fig. 7, where the blue line represents the estimated ESR *hm*F2s and the red line the IRI *hm*F2s. As shown, the general tendency seems to be that the agreement is best during solar maximum, while the IRI model overestimates the *hm*F2 during solar minimum. The IRI model seems to reproduce the *hm*F2 measured by the ESR best in the time intervals 03:00–12:00 UT. Figure 7 shows that the IRI *hm*F2 has greater seasonal variation than the ESR *hm*F2, especially at nighttime.

4 Conclusions

Electron density from the IRI-2016 model has been compared with data from the EISCAT Svalbard radar covering more than one solar cycle. The results of this comparison could be useful for users and developers of the IRI model, since it is possible from our study to identify the time periods and altitude ranges where the model might need improvement. Also, an inclusion of the entire ESR data set might contribute to improving the performance of the IRI model at high latitudes. The most important results are summarized as follows:

- The IRI model is found to be biased towards an underestimation of the electron density in the polar cap and cusp. This underestimation is most severe at nighttime and during solar maximum. A large discrepancy between the IRI TEC and ESR TEC during the solar maximum (1999–2002) is consistent with the findings of Themens et al. (2014) from the latest solar maximum.

- Also previous versions of the IRI model have been compared with the ESR electron density. Comparisons with the IRI-2001 and the IRI-2012 model show that there are no major differences in the performance of the IRI-2016 model and of previous versions. There are, however, some small differences. Most noticeably, the IRI-2012 and IRI-2016 model reproduce the electron density during winter 2001 significantly better than the IRI-2001 model. During solar minimum, the IRI-2016 model seems to be slightly improved for altitudes below the *hm*F2 compared with the IRI-2012 model.

- An overestimation of the *hm*F2 occurs both during solar minimum and solar maximum, but it seems to be slightly stronger during nighttime than during daytime. At nighttime the IRI model *hm*F2 has clear seasonal variations, while the *hm*F2 observed with the ESR radar has very little seasonal variation.

- Finally, the comparison shows that the IRI model performs best at altitudes close to the *hm*F2. At these altitudes (around 350 km during solar maximum and 260 km solar minimum), the IRI model reproduces the electron density more accurately than at higher or lower altitudes.

Data availability

The EISCAT Svalbard radar data were retrieved from the Madrigal database (CEDAR Archival Madrigal Database, 2016) and are freely available from http://madrigal.haystack.mit.edu. Fortran code for the various versions of the IRI model (International Reference Ionosphere, 2016) used can all be downloaded from http://irimodel.org.

Acknowledgements. EISCAT is an international association supported by research organizations in China (CRIRP), Finland (SA), Japan (NIPR and STEL), Norway (NFR), Sweden (VR) and the United Kingdom (NERC). The authors wish to thank the IRI working group for providing the models used in this paper.

The topical editor, S. Milan, thanks D. Bilitza and one anonymous referee for help in evaluating this paper.

References

Altadill, D., Torta, J., and Blanch, E.: Proposal of new models of the bottom-side B0 and B1 parameters for IRI, Adv. Space Res., 43, 1825–1834, doi:10.1016/j.asr.2008.08.014, 2009.

Bilitza, D.: The International Reference Ionosphere 1990, National Space Science Data Center, NSDCC/WDC-A-R&S Reports 90-22, 1990.

Bilitza, D.: International Reference Ionosphere 2000, Radio Sci., 36, 261–275, doi:10.1029/2000RS002432, 2001.

Bilitza, D. and Reinisch, B. W.: International Reference Ionosphere 2007: Improvements and new parameters, Adv. Space Res., 42, 599–609, doi:10.1016/j.asr.2007.07.048, 2008.

Bilitza, D., Altadill, D., Zhang, Y., Mertens, C., Truhlik, V., Richards, P., McKinnell, L.-A., and Reinisch, B.: The International Reference Ionosphere 2012 – a model of international collaboration, J. Space Weather Space Clim., 4, A07, doi:10.1051/swsc/2014004, 2014.

Brum, C. G. M., Rodrigues, F. D. S., Dos Santos, P. T., Matta, A. C., Aponte, N., Gonzalez, S. A., and Robles, E.: A modeling study of

f_oF_2 and h_mF_2 parameters measured by the Arecibo incoherent scatter radar and comparison with IRI model predictions for solar cycles 21, 22, and 23, J. Geophys. Res.-Space, 116, A03324, doi:10.1029/2010JA015727, 2011.

CEDAR Archival Madrigal Database: EISCAT Svalbard radar data, available at: http://madrigal.haystack.mit.edu, last access: 12 September 2016.

Chuo, Y. and Lee, C.: Ionospheric variability at Taiwan low latitude station: Comparison between observations and IRI-2001 model, Adv. Space Res., 42, 673–681, doi:10.1016/j.asr.2007.04.078, 2008.

Coïsson, P., Radicella, S., Leitinger, R., and Nava, B.: Topside electron density in IRI and NeQuick: Features and limitations, Adv. Space Res., 37, 937–942, doi:10.1016/j.asr.2005.09.015, 2006.

Cowley, S. W. H. and Lockwood, M.: Excitation and decay of solar wind–driven flows in the magnetosphere–ionosphere system, Ann. Geophys., 10, 103–115, 1992.

Foster, J. C., Coster, A. J., Erickson, P. J., Holt, J. M., Lind, F. D., Rideout, W., McCready, M., van Eyken, A., Barnes, R. J., Greenwald, R. A., and Rich, F. J.: Multiradar observations of the polar tongue of ionization, J. Geophys. Res.-Space, 110, A09S31, doi:10.1029/2004JA010928, 2005.

Goodwin, L., Iserhienrhien, B., Miles, D. M., Patra, S., van der Meeren, C., Buchert, S. C., Burchill, J., Clausen, L. B. N., Knudsen, D. J., McWilliams, K. A., and Moen, J.: Swarm in situ observations of F-region polar cap patches created by cusp precipitation, Geophys. Res. Lett., 42, 996–1003, doi:10.1002/2014GL062610, 2015.

International Reference Ionosphere (IRI): Fortran code for various versions of the IRI model, available at: http://irimodel.org, last access: 12 September 2016.

Kelley, M. C., Vickrey, J. F., Carlson, C. W., and Torbert, R.: On the origin and spatial extent of high-latitude F region irregularities, J. Geophys. Res.-Space, 87, 4469–4475, doi:10.1029/JA087iA06p04469, 1982.

Kim, E., Chung, J.-K., Kim, Y. H., Jee, G., Hong, S.-H., and Cho, J.-H.: A climatology study on ionospheric F_2 peak over Anyang, Korea, Earth Planets Space, 63, 335–349, doi:10.5047/eps.2011.03.011, 2011.

Lei, J., Liu, L., Wan, W., Zhang, S.-R., and van Eyken, A. P.: Comparison of the first long-duration IS experiment measurements over Millstone Hill and EISCAT Svalbard radar with IRI2001, Adv. Space Res., 37, 1102–1107, doi:10.1016/j.asr.2005.01.061, 2006.

Lockwood, M. and Carlson, H. C.: Production of polar cap electron density patches by transient magnetopause reconnection, Geophys. Res. Lett., 19, 1731–1734, doi:10.1029/92GL01993, 1992.

Oksavik, K., Ruohoniemi, J. M., Greenwald, R. A., Baker, J. B. H., Moen, J., Carlson, H. C., Yeoman, T. K., and Lester, M.: Observations of isolated polar cap patches by the European Incoherent Scatter (EISCAT) Svalbard and Super Dual Auroral Radar Network (SuperDARN) Finland radars, J. Geophys. Res.-Space, 111, A05310, doi:10.1029/2005JA011400, 2006.

Oyeyemi, E., Adewale, A., Adeloye, A., and Akala, A.: Comparison between IRI-2001 predictions and observed measurements of hmF2 over three high latitude stations during different solar activity periods, J. Atmos. Terr. Phys., 72, 676–684, doi:10.1016/j.jastp.2010.03.009, 2010.

Radicella, S.: The NeQuick model genesis, uses and evolution, Ann. Geophys.-Italy, 52, 417–422, doi:10.4401/ag-4597, 2009.

Themens, D. R. and Jayachandran, P.: Solar Activity Variability in the IRI at high latitudes: Comparisons with GPS Total Electron Content, J. Geophys. Res.-Space, 121, 3793–3807, doi:10.1002/2016JA022664, 2016.

Themens, D. R., Jayachandran, P. T., Nicolls, M. J., and MacDougall, J. W.: A top to bottom evaluation of IRI 2007 within the polar cap, J. Geophys. Res.-Space, 119, 6689–6703, doi:10.1002/2014JA020052, 2014.

Vickers, H., Kosch, M. J., Sutton, E., Bjoland, L., Ogawa, Y., and La Hoz, C.: A solar cycle of upper thermosphere density observations from the EISCAT Svalbard Radar, J. Geophys. Res.-Space, 119, 6833–6845, doi:10.1002/2014JA019885, 2014.

Walker, I. K., Moen, J., Kersley, L., and Lorentzen, D. A.: On the possible role of cusp/cleft precipitation in the formation of polar-cap patches, Ann. Geophys., 17, 1298–1305, doi:10.1007/s00585-999-1298-4, 1999.

Wichaipanich, N., Supnithi, P., Tsugawa, T., Maruyama, T., and Nagatsuma, T.: Comparison of ionosphere characteristic parameters obtained by ionosonde with IRI-2007 model over Southeast Asia, Adv. Space Res., 52, 1748–1755, doi:10.1016/j.asr.2012.06.018, 2013.

Zhang, Q.-H., Zhang, B.-C., Moen, J., Lockwood, M., McCrea, I. W., Yang, H.-G., Hu, H.-Q., Liu, R.-Y., Zhang, S.-R., and Lester, M.: Polar cap patch segmentation of the tongue of ionization in the morning convection cell, Geophys. Res. Lett., 40, 2918–2922, doi:10.1002/grl.50616, 2013.

Zhang, S.-R. and Holt, J. M.: Ionospheric plasma temperatures during 1976–2001 over Millstone Hill, Adv. Space Res., 33, 963–969, doi:10.1016/j.asr.2003.07.012, 2004.

Note on paper I

Recently, I found an error in the code I used to obtain the IRI data and produce the plots using IRI data. This would affect figures 2-7 in paper I, but the difference between the original figures and the corrected figures is small, and does not affect the results, discussion or conclusions in the original paper. The corrected figures are provided in this section for completeness. Only in the plot showing the comparison between IRI-2001 and the EISCAT data during winter in the solar maximum, shown in figure 4 of the paper, we see a clear difference from the corrected version of the plot shown in figure 8.3. For the ratios given in chapter 3.1.1. of the paper, the updated values are as follows: The median ratio over the spring and summer plots for altitudes 440-500 km in figure 8.3 is 0.98, 1.42 and 1.39 for the IRI-2001, IRI-2012 and IRI-2016 model, respectively. During the equinoxes, the median ratio below 300 km is 1.37 for the IRI-2012 model and 2.13 for the IRI-2016 model. In figure 8.4, the median ratio below 300 km altitude for all seasons is 1.37 for the IRI-2012 model and 1.34 for the IRI-2016 model. The mean ratio below 300 km altitude is 3.40 and 2.01 for the IRI-2012 and IRI-2016 model, respectively.

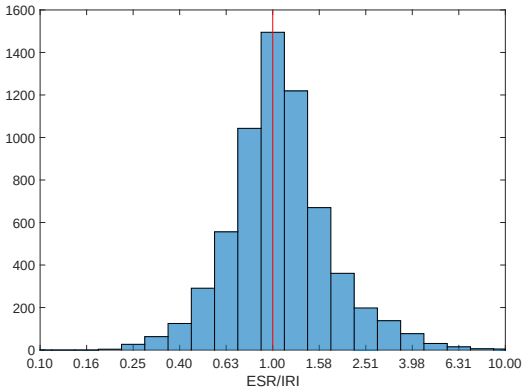

Figure 8.1: Histogram showing the distribution of all the data without binning. The x-axis show the ratio between ESR data and the IRI model, the y-axis the number of data points.

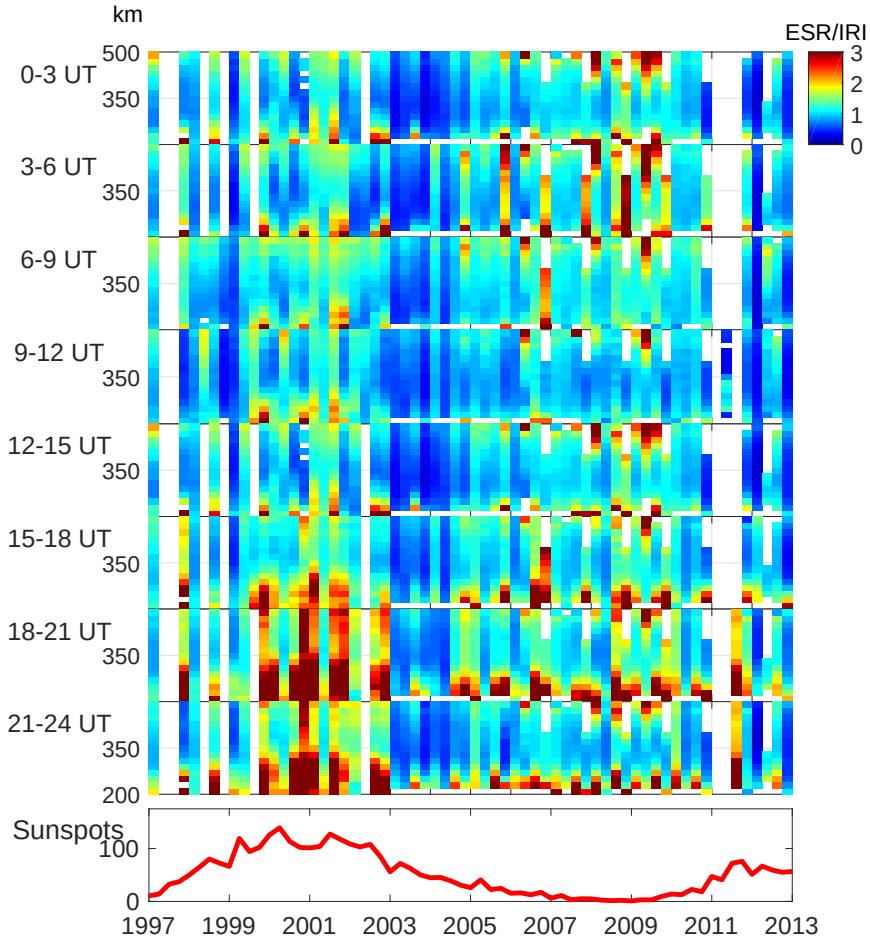

Figure 8.2: Altitude profiles of the ratio between ESR and IRI electron densities. The 8 top panels correspond to the different three hour integration intervals. The last panel shows the 3-month averaged sunspot number. The four columns for each year represent the seasons in the order of spring, summer, autumn and winter.

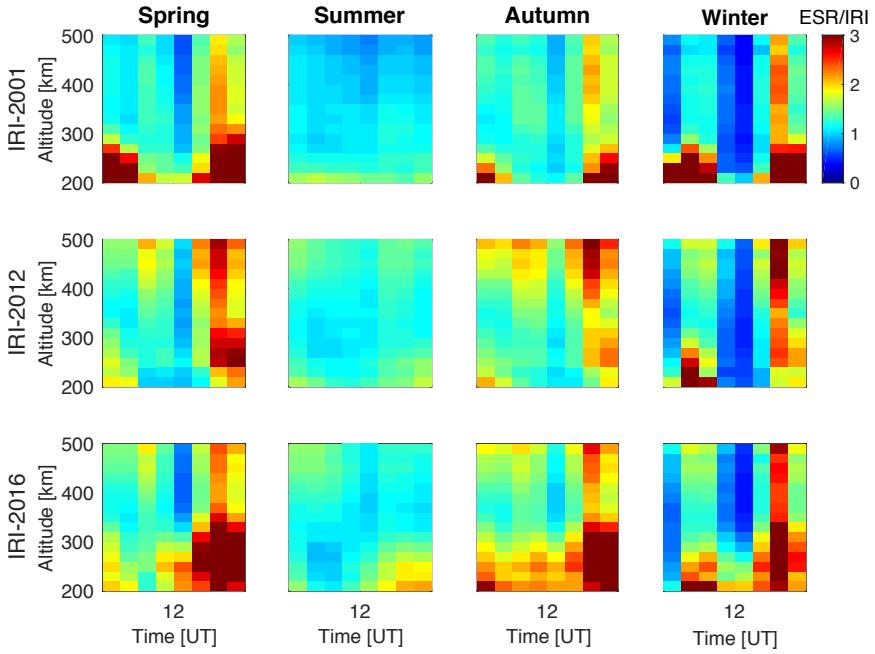

Figure 8.3: Altitude profiles of the ratio between ESR and IRI electron densities for three different versions of the IRI model (IRI-2001, IRI-2012 and IRI-2016) in 2001. The data have been binned according to season, as indicated, and as daily three hour averages. The rows show how the IRI-2001, IRI-2012 and IRI-2016 models reproduce the polar ionosphere during 2001 respectively.

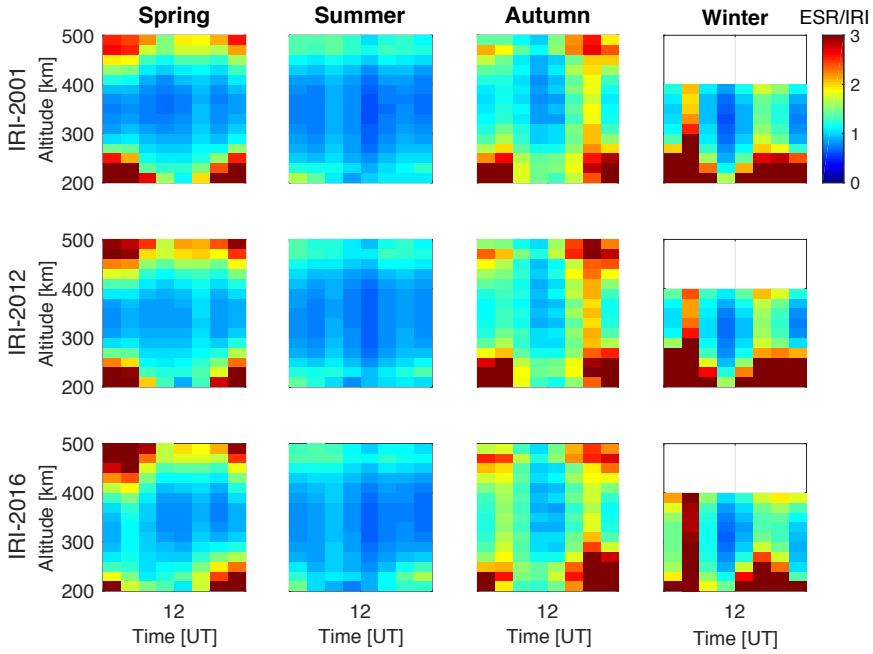

Figure 8.4: Same as Fig. 8.3, but for 2008, in the extended solar minimum, instead of 2001.

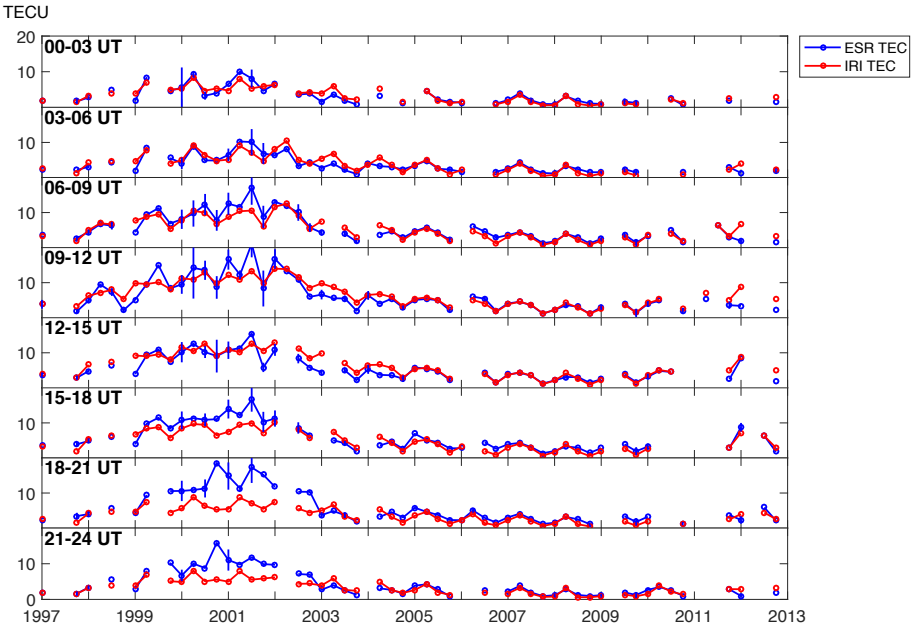

Figure 8.5: Total electron content from ESR (blue) and IRI model (red) given in TEC Units (TECU). Each panel correspond to a three hour integration bin, and each year contain 4 seasonal bins (spring, summer, autumn and winter).

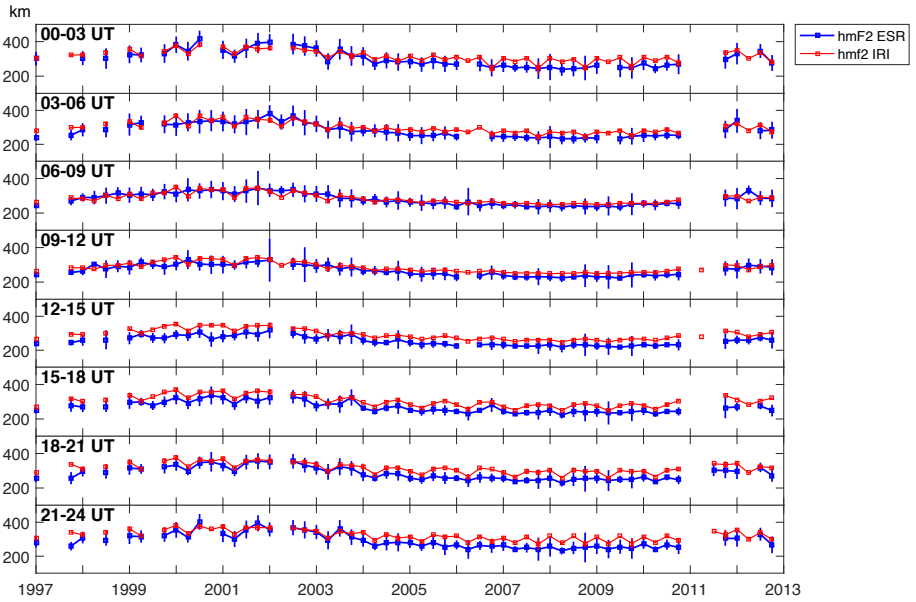

Figure 8.6: The height of the F2 peak from ESR (blue) and IRI model (red). Each panel correspond to a three hour integration bin, and each year contain 4 seasonal bins (spring, summer, autumn and winter). Error bars correspond to one standard deviation.

Paper II:
Long-term variations and trends in the polar E-region

L. M. Bjoland, Y. Ogawa, C. Hall, M. Rietveld, U. P. Løvhaug, C. La Hoz and H. Miyaoka, *Journal of Atmospheric and Solar-Terrestrial Physics*, **163**, 85-90, (2017), doi: 10.1016/j.jastp.2017.02.007.

Journal of Atmospheric and Solar-Terrestrial Physics 163 (2017) 85–90

Contents lists available at ScienceDirect

Journal of Atmospheric and Solar-Terrestrial Physics

journal homepage: www.elsevier.com/locate/jastp

Long-term variations and trends in the polar E-region

L.M. Bjoland [a,*], Y. Ogawa [b], C. Hall [c], M. Rietveld [a,d], U.P. Løvhaug [a], C. La Hoz [a], H. Miyaoka [b]

[a] Department of Physics and Technology, University of Tromsø–The Arctic University of Norway, Tromsø, Norway
[b] National Institute of Polar Research, Tokyo, Japan
[c] Tromsø Geophysical Observatory, University of Tromsø–The Arctic University of Norway, Tromsø, Norway
[d] EISCAT Scientific Association, Ramfjordmoen, Norway

ARTICLE INFO

Keywords:
Polar ionosphere
Long-term trends
Hall conductivity
Ion temperature

ABSTRACT

As the EISCAT UHF radar system in Northern Scandinavia started its operations in the early 1980s, the collected data cover about three solar cycles. These long time-series provide us the opportunity to study long-term variations and trends of ionospheric parameters in the high latitude region.

In the present study we have used the EISCAT Tromsø UHF data to investigate variations of the Hall conductivity and ion temperatures in the E-region around noon. Both the ion temperature and the peak altitude of the Hall conductivity are confirmed to depend strongly on solar zenith angle. However, the dependence on solar activity seems to be weak.

In order to search for trends in these parameters, the ion temperature and peak altitude of the Hall conductivity data were adjusted for their seasonal and solar cycle dependence. A very weak descent (~0.2 km/ decade) was seen in the peak altitude of the Hall conductivity. The ion temperature at 110 km shows a cooling trend (~10 K/ decade). However, other parameters than solar zenith angle and solar activity seem to affect the ion temperature at this altitude, and a better understanding of these parameters is necessary to derive a conclusive trend.

In this paper, we discuss what may cause the characteristics of the variations in the electric conductivities and ion temperatures in the high latitude region.

1. Introduction

At high latitudes, the magnetic field lines are nearly vertical and couple the polar ionosphere to the outer magnetosphere. Field-aligned currents play an important role in this coupling as they transfer energy and momentum between the magnetosphere and the polar ionosphere. These currents are mainly closed by Pedersen currents in the ionosphere, and energy is dissipated as Joule heating. This effect is strongest in the ionospheric E-region (90–150 km) where the conductivities are highest.

The conductivity is determined by the plasma density, geomagnetic field and the collision frequencies. In the E-region the electrons are governed by the $\mathbf{E} \times \mathbf{B}$ drift, while the ions are controlled by collisions with neutrals. As a result, this is the region where the velocity difference between the ions and the electrons are largest, and the currents therefore largest. The Hall and Pedersen conductivities both have their peak heights in this region. The Hall conductivity (perpendicular to both the electric and the magnetic field) peaks at about 110 km, whereas the Pedersen conductivity (parallel to the electric field) peaks at approximately 120 km altitude. At polar latitudes, these conductivities can be significantly enhanced due to energetic particle precipitation which affects the electron density and temperature.

Although solar UV and X-ray radiation are the main heating sources, Joule heating and energetic particle precipitation can also cause significant heating in the polar ionosphere. In addition, gravity wave activity can affect the upper atmospheric temperature, and below the turbopause turbulent energy dissipation heats the upper atmosphere, in particular during summer. Heat loss mainly occurs due to infrared radiation by climate gases such as carbon dioxide (CO_2) and methane (CH_4). Increased concentrations of climate gases due to anthropogenic emissions will therefore lead to a cooling of the upper atmosphere. This is expected to lead to changes also in the ionosphere (Roble and Dickinson, 1989).

In this study the characteristics of the polar E-region ion temperature and Hall conductivity are investigated using more than 30 years of data from the EISCAT Tromsø radar. The height profile of the Pedersen conductivity strongly depends on the modeled values (MSIS neutral densities and IGRF geomagnetic field), so we focused on investigation of the Hall conductivity in this study. Previous studies have also derived conductivity data from EISCAT radars. These studies have mostly investigated

* Corresponding author.
E-mail address: lindis.m.bjoland@uit.no (L.M. Bjoland).

https://doi.org/10.1016/j.jastp.2017.02.007
Received 15 December 2016; Received in revised form 14 February 2017; Accepted 17 February 2017
Available online 20 February 2017

the height-integrated conductivity and its dependence on various parameters such as solar flux, geomagnetic activity and solar zenith angle (e.g. (Moen and Brekke, 1993; Sugino et al., 2002; Ieda et al., 2014)). In the present study we focus on the peak height of the Hall conductivity and the ion temperature at 110 km altitude.

A cooling of the F region ionosphere has previously been found using EISCAT data (Ogawa et al., 2014). Similar observations of F region ionospheric cooling are also reported from studies of incoherent scatter radar (ISR) data from other latitudes (e.g. (Zhang et al., 2016)). Ionosonde measurements show decreasing trends in the F region peak height and critical frequency, consistent with a cooling of the upper atmosphere due to the greenhouse effect (Mielich and Bremer, 2013). In the high latitude E-region, there are no results from ISR measurements because of the lack of a systematic dataset. However, ionosonde studies indicate that there are trends in the peak height and critical frequency. For example, Hall et al. (2011) found a decrease of the E-region height of −1 km/decade using 63 years of data from the Tromsø ionosonde. A decreasing trend can therefore be expected in the peak height of the Hall conductivity.

Previous studies of long-term trends in the temperature have found that the trend is altitude-dependent. Studies have shown a cooling in the mesosphere (e.g. (Golitsyn et al., 1996)) and no trend (e.g. (Beig, 2003)) or a cooling trend (e.g. (Holmen et al., 2016)) in the mesopause. From higher altitudes, there are not much available neutral temperature data (Laštovička et al., 2012). There are, however, also previous studies investigating trends in the ion temperature. Below 300 km the ion temperature can be used as a proxy for the neutral temperature, as they are very similar at these altitudes. Results from midlatitude incoherent scatter radars show that there is a cooling between 200 km and 550 km and a heating below 200 km altitude at Millstone Hill (Zhang et al., 2011). Donaldson et al. (2010) measured heating between ~ 110 km and 170 km using ISR measurements from Saint Santin. However, when correcting the temperature profile for subsidence of overlaying warmer atmosphere, Donaldson et al. (2010) found that a cooling exists for all altitudes below 500 km. At high latitudes, Ogawa et al. (2014) reported a cooling of the ion temperature between 200 and 380 km altitude and no trend or warming between 400 km and 470 km altitude. In the present study we investigate if it is possible to detect any trends in the E-region peak height and ion temperature.

2. Method

The EISCAT Tromsø radar is located at geographic coordinates 69.58°N and 19.23°E, and has been operational since the beginning of the 1980s. From the radar data, it is possible to obtain information about primary plasma parameters such as; electron density, ion and electron temperatures and line-of-sight ion velocity. These parameters are determined by fitting a theoretical autocorrelation function derived from plasma theory to the measured autocorrelation function. Only the raw electron density is obtained directly from the backscattered power profile. In the present study we have derived the Hall conductivity from the EISCAT electron density data.

Raw data in the form of an autocorrelation function from the EISCAT Tromsø radar between 1981 and 2015 were analyzed using a 1-h integration interval. The whole data set was analyzed using the Grand Unified Incoherent Scatter Design and Analysis Package (GUISDAP) software (Lehtinen and Huuskonen, 1996). Only measurements from around noon (start time of integration 10–11 UT) and when the elevation angle of the radar was larger than 70° have been used. Data from experiments during which the EISCAT heating facility were used have been removed from the data set.

Electron density measured by EISCAT was used to calculate the E-region conductivity. Due to systematical offsets that sometimes occur in the EISCAT electron density, the data need to be calibrated. To calibrate the EISCAT electron density profiles, the F2 peak density (NmF2) was found for each EISCAT profile and used to calculate the F2 plasma frequency (foF2). Ratios between EISCAT foF2 and foF2 measured by the Tromsø ionosonde and dynasonde were calculated, and these ratios were used to calibrate the electron density and conductivity profiles. As the peak height of the conductivity does not change when the profile is calibrated, uncalibrated data were also used for the investigation of the peak height. This allows the use of a larger data set, since available ionosonde/dynasonde data are required to do a calibration. Erroneous electron density/ conductivity profiles that sometimes occur were removed from the data set. Profiles from times with solar zenith angles larger than 85° were mostly erroneous, and the peak altitudes were scattered over a large altitude range. Data with solar zenith angles larger than 85° were therefore not included in the analysis of the conductivity.

In addition, data with range resolution larger than 10 km were removed from the data set. For the remaining data, the average range resolution was 8.3 km before 1984. After 1984 the average range resolution for the data used was 2.7 km. Both fitted and power profile data were used for the study of conductivities. The gate separation was frequently smaller for power profile data than for the fitted data, and sometimes power profile data are also available from lower altitudes. In these cases, power profile data were usually used instead of the fitted data. However, for the study of ion temperatures only fitted data have been used.

The following equation was used to calculate the Hall conductivity:

$$\sigma_H = \frac{n_e e}{B}\left(\frac{k_e^2}{1+k_e^2} - \frac{k_i^2}{1+k_i^2}\right) \quad (1)$$

where n_e is the electron density from the EISCAT measurements, e is the electron charge, B is the magnetic field strength calculated by using the IGRF model and k_i and k_e are the ion and electron mobility coefficients defined by $k_i = \Omega_i/\nu_{in}$ and $k_e = \Omega_e/\nu_{en}$. ν_{in} and ν_{en} are the ion-neutral and the electron-neutral collision frequencies, and the gyrofrequencies are given by $\Omega_i = eB/m_i$ and $\Omega_e = eB/m_e$. Neutral density and electron temperature are needed to calculate the collision frequencies, and estimates for these parameters were found with the MSIS model. The F10.7 and ap indices were used as input for the MSIS model. At E-region altitudes ion and neutral temperatures are comparable, and the MSIS neutral temperature was therefore used as an estimate for the ion temperature when calculating the collision frequencies.

3. Results

3.1. Hall conductivity

Fig. 1 provides an overview of the Hall conductivity in the E-region during the entire period since the EISCAT UHF radar started its operations in the beginning of the 1980s. Each column corresponds to two-month averages, and the black cross in each column indicates the peak height where the Hall conductivity maximises. The peak height is seen to be near to 110 km altitude, although it shows large variations. This is in contrast to the Pedersen conductivity (not shown), which has a much more constant peak height around 120 km.

Fig. 2 shows average profiles of Hall conductivity (left) and electron density (right) for winter and summer. Here summer is defined as the time period for which 45° < solar zenith angle (SZA) < 55° and winter as the time period for which 75° < SZA < 85°. The length of the error bars equals one standard deviation. Both the Hall conductivity profile and the electron density profile have strong seasonal variations. The absolute values of the Hall conductivity and electron density are higher during summer than during winter as expected. During summer the E region Hall conductivity and electron density are about twice as large as during winter. Also the shape of the profile varies with season. The Hall conductivity profile has a broader peak area in summer, and the peak height is about 5 km lower than during winter.

Hall conductivity at 110 km altitude vs SZA is shown in Fig. 3 for three different levels of solar activity, F10.7 < 100 solar flux units (sfu),

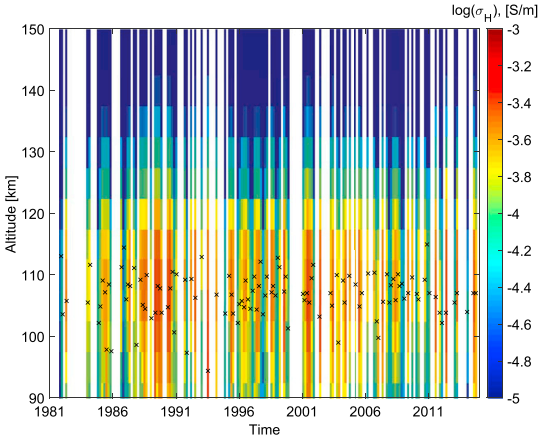

Fig. 1. Hall conductivity in the E-region between 90 and 150 km altitude vs time. Each column represents a two-month average. Black crosses indicate the peak height of the conductivity.

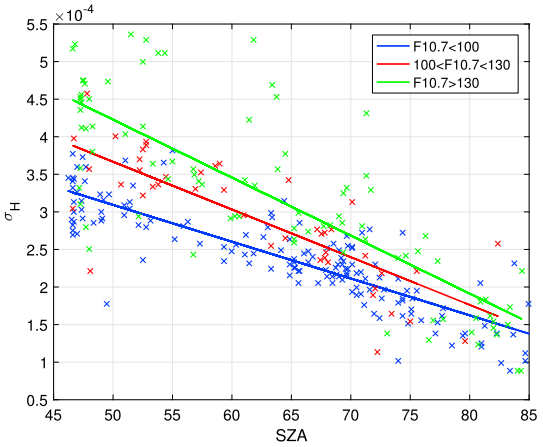

Fig. 3. Hall conductivity at 110 km vs solar zenith angle for three different levels of the F10.7 index.

100 sfu < F10.7 < 130 sfu and F10.7 > 130 sfu. Fitted regression lines for each level of solar activity are also shown in Fig. 3. The regression lines are given by:

$$\sigma_H = 5.5 * 10^{-4} - 4.9 * 10^{-6} * SZA \ (\text{for F10.7} < 100) \quad (2)$$

$$\sigma_H = 6.8 * 10^{-4} - 6.3 * 10^{-6} * SZA \ (\text{for } 100 < \text{F10.7} < 130) \quad (3)$$

$$\sigma_H = 8.1 * 10^{-4} - 7.7 * 10^{-6} * SZA \ (\text{for } 130 < \text{F10.7}) \quad (4)$$

These equations show that, at this altitude, the Hall conductivity is decreasing as the solar zenith angle increases, and that there is a clear dependence on the level of solar activity. The variations caused by the dependence of solar zenith angle are approximately $2 * 10^{-4}$ S/m and variations due to solar activity are found to be approximately $8 * 10^{-5}$ S/m. When the solar activity is high, the conductivity close to the peak height is also high. In addition, the higher the level of solar activity the more rapidly the Hall conductivity will decrease with an increase in solar zenith angle. On the other hand, the solar activity dependence of the Hall conductivity peak height is very weak. Solar zenith angle (season) seems to be the most important factor for determining the peak height. As the solar zenith angle decreases, the peak height will also decrease.

The upper panel of Fig. 4 shows the measured peak heights vs solar zenith angle. A line was fitted to the data to find a relation between the solar zenith angle and Hall peak height and this line is also shown in the figure. The following equation was obtained from the fit:

$$h\prime = 0.163 * SZA + 98.247 \quad (5)$$

Here $h\prime$ is the estimated peak height of the Hall conductivity as a function of *SZA*. Variations of the peak height due to solar zenith angle are found to be approximately 6 km. Variations caused by solar activity (F10.7) are shown in Fig. 5. These variations were found to be weak, approximately 0.1 km, and the F10.7 dependency is therefore not included in (5).

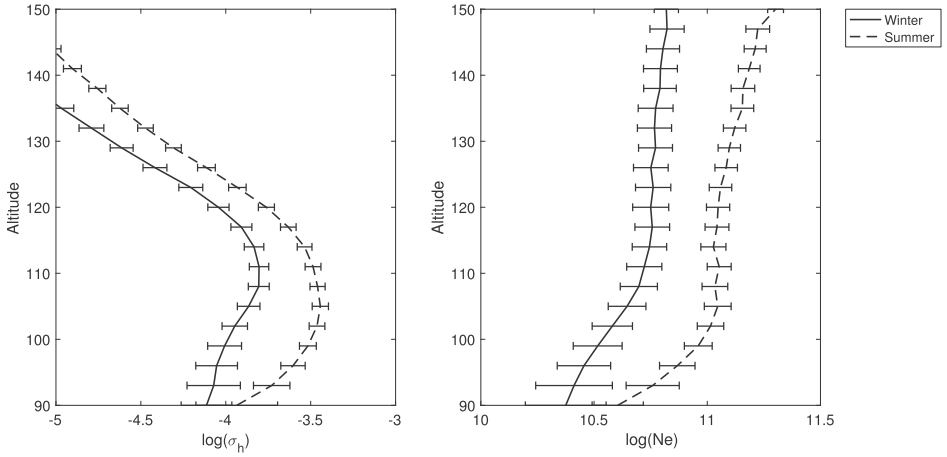

Fig. 2. Average profiles of Hall conductivity (left) and electron density (right) in the E-region between 90 and 150 km altitude for winter (solid line) and summer (dashed line). Winter refers to days with solar zenith angles between 75° and 85° and summer to days with solar zenith angles between 45° and 55°. The length of the error bars is equal to one standard deviation.

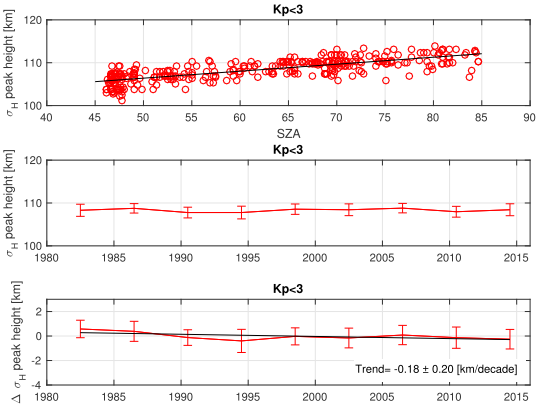

Fig. 4. Upper panel: Hall conductivity peak height vs solar zenith angle. Middle panel: 4-year averages of Hall conductivity peak height vs time. Lower panel: 4-year averages of the Hall conductivity peak height vs time. The peak height has been adjusted for solar zenith angle. Error bars correspond to one standard deviation.

The estimated peak height was subtracted from the measured peak height in order to obtain a delta peak height independent of solar zenith angle. Fig. 4 shows the 4-year average of the measured peak height (middle panel) and the delta peak height (lower panel) vs time. Error bars correspond to one standard deviation. Only data with Kp-index lower than 3 are included in the figure, in order to reduce the effect of geomagnetic activity. A very weak descent of the peak height is observed in the lower panel. The size of this descent is -0.18 ± 0.20 km/decade, where 0.20 is the 95% confidence interval. This trend is, however, within the standard deviations of the averaged peak heights.

3.2. Ion temperature

In addition to the conductivity, the ion temperature at 110 km altitude was investigated. Fig. 6 shows the dependence of the ion temperature on solar zenith angle and solar activity. In the upper panel ion temperature is plotted vs solar zenith angle. The F10.7 index is used as an indicator of solar activity, and the lower panel of the figure shows ion temperature vs F10.7 It is evident that the ion temperature depends

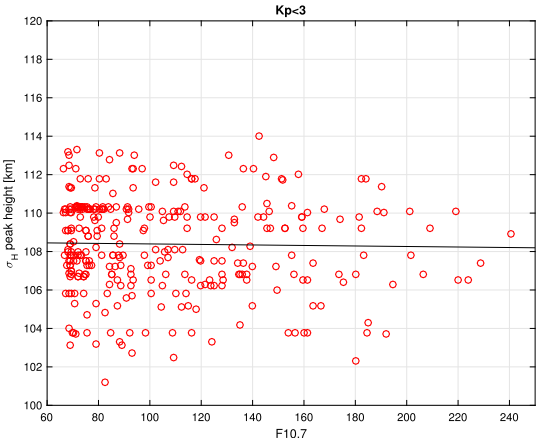

Fig. 5. Hall conductivity peak height vs solar activity (F10.7). The figure illustrates that variations caused by solar activity are weak.

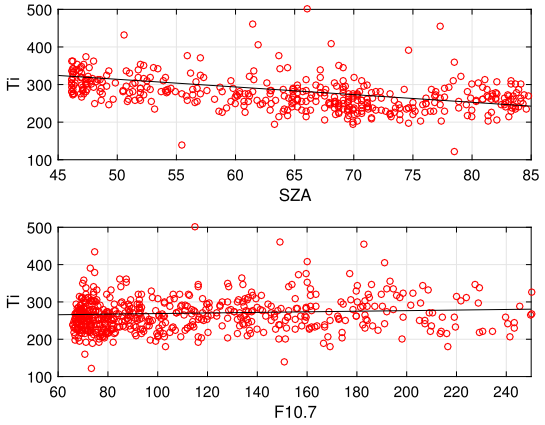

Fig. 6. Upper panel: Ion temperature at 110 km vs solar zenith angle. Lower panel: Ion temperature at 110 km vs the F10.7 index.

strongly on solar zenith angle, and that the dependence on solar zenith angle is much stronger than the dependence on solar activity at this altitude. For low solar zenith angles (summer), ion temperature is usually between 250 and 350 K. For higher solar zenith angles (winter) the ion temperature is usually between 200 and 300 K.

Ion temperature at 110 km altitude are shown in Fig. 7. The F10.7 index was used as a proxy for solar activity, and the following equation was used to adjust for the solar zenith angle and solar activity:

$$Ti_{sol,F10.7} = A + B * SZA + C * F10.7 + D * F10.7^2 \quad (6)$$

In this equation $Ti_{sol,F10.7}$ is the estimated ion temperature as a function of *SZA* and the F10.7 index. A quadratic term of F10.7 is included in the equation to take into account the saturation of ion temperature at high levels of F10.7 found in previous studies (e.g. (Holt and Zhang, 2008)). The constants *A*, *B*, *C* and *D* were found to be 340.68, −1.43, 0.32 and −0.0009, respectively. From these results, it is estimated that a change between high (~85°) and low (~ 45°) solar zenith angles causes a

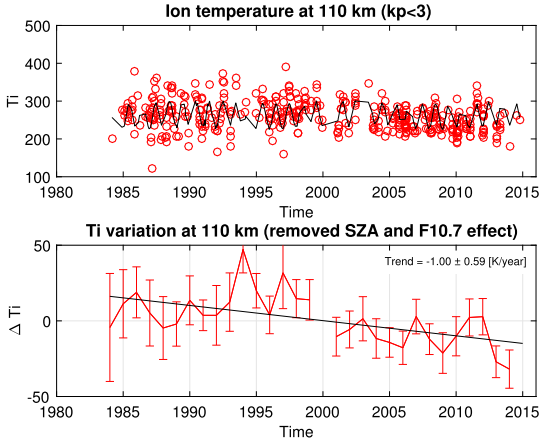

Fig. 7. Upper panel: Scatter plot of ion temperature at 110 km vs time. The black line is the fitted variation due to solar radiation (SZA) and solar activity (F10.7). Lower panel: Yearly averages of ion temperature at 110 km, adjusted for solar zenith angle, vs time. The length of the error bars correspond to one standard deviation. A black line is fitted to the data and indicates the observed trend.

variation in ion temperature of approximately 60 K. Likewise, the level of solar activity can cause variations in ion temperature of approximately 10 K.

A scatter plot of the ion temperatures vs time is shown together with the estimated $Ti_{sol,F10.7}$ variation in the upper panel of Fig. 7. In the lower panel of the figure, the estimated $Ti_{sol,F10.7}$ is subtracted from the measured T_i and the residual ΔT_i is plotted as annual averages vs time. Error bars correspond to one standard deviation, and the median size of the standard deviations are about 26 K. The fitted trend line indicate a decreasing trend of −1.00±0.59 K/year in the time period 1984–2015. However, it is possible that this result is influenced by the choice of Eq. (6) to estimate the ion temperature. A further discussion of this issue is found in chapter 4.2.

4. Discussion

4.1. Conductivity

From Eq. (1), it is seen that the Hall conductivity depends on the electron density, magnetic field strength and the mobility coefficients. The shape of the conductivity profile and location of the peak height are therefore determined by the electron density profile and the mobility coefficients. Fig. 2 shows that the electron density decrease sharply below ~110 km during winter. In summer this decrease of electron density starts at a lower altitude. This difference between the shapes of the summer and winter electron density profiles results in a broader peak area in the Hall conductivity and a lower peak height during summer.

The expected trend in the peak height of the electron density in the E-region (hmE) is low. Rishbeth (1990) estimated that a doubling of the concentrations of CO_2 and CH_4 in the mesosphere would cause the hmE to decrease by only 2.5 km. Data from the Tromsø ionosonde shows a decrease in hmE of 1.5 km/decade after 1968 (Hall et al., 2011). A decreasing trend is therefore expected to occur also in the conductivity peak height since the Hall conductivity peak height depends on the shape of the electron density profile. If the trend in the peak height of the conductivity is similar to the trend observed in hmE by Hall et al. (2011), the peak height would decrease by 4–5 km over the more than 30 year long data series of EISCAT data. However, no conclusive trend was observed in the peak height of the Hall conductivity. The observed descent of about ~0.6 km/30 years, is significantly lower than the trend observed by Hall et al. (2011). They also showed that the trend was different for the time periods 1948–2011 and 1968–2011 with −1 km/decade and −1.5 km/decade, respectively. Investigations show that using the same ionosonde data, the trend becomes smaller for the time period 1984–2015 (updated information after Hall et al. (2011)). This time period is closer to the time period of the EISCAT data, and it is therefore clear that the different time ranges used in our study and the study of Hall et al. (2011) can explain at least part of the discrepancies between our results.

Long term changes in the Earth's magnetic field will contribute to changes in the absolute value of the conductivity and could also affect the peak height. The IGRF model shows an increase in the magnetic field at Tromsø of about 600 nT (~1% of the total magnetic field) during the last 30 years. As the IGRF magnetic field was used to calculate the Hall conductivity, the effect of this increase on the long-term changes in Hall conductivity peak height was investigated. The change in the peak height due to the magnetic field change was found to be less than 0.01 km.

To reduce the effect of geomagnetic activity, data are only used when the Kp-index is lower than 3. To check if this limit sufficiently reduced the effect of geomagnetic activity, we also checked the results using only data with Kp-index lower than 2, and using all data regardless of Kp-index. Only small differences were found between the three options. When using all data regardless of Kp index, the trend in the peak height was −0.016±0.027 km/year, and when using only data with Kp less than 2 the trend was found to be −0.012±0.016 km/year. At daytime Tromsø is located in the subauroral zone. Only data from around noon have been used, and the effect of particle precipitation should therefore be low.

From these results it is clear that if there is a trend in the peak height of the Hall conductivity this trend is very weak, and it is therefore not possible to make a significant detection of it with the current EISCAT data set. A possible descent could perhaps be caused by a descent in the mobility coefficients.

4.2. Temperature

In the upper panel of Fig. 7, the original ion temperature samples are plotted together with the fitted results from Eq. (6). Several differences between the fitted result and the original samples can be seen, and the correlation coefficient between the fitted and the original results is only approximately 0.6. This suggests that also other parameters than solar zenith angle and solar activity might affect the variation in ion temperature. The effect of neutral wind and wave activity (e.g., tides and planetary waves) could possibly explain part of the difference between the fitted results and the original samples. Wave activity would lead to changes in the neutral temperature, and via collisions the ion temperature will approach the neutral temperature when the electric field is small. Hall et al. (2016) found a positive trend in the Tromsø summer turbopause. This trend indicates that heating is increasing in the lower E-region. As turbulence is partly attributable to gravity wave breaking, the trend found in the turbopause suggests that there might be a trend in the gravity wave activity. Hall et al. (2016) also estimated that during the time period 1999–2015 the trend in neutral temperature at 90 km altitude was 0.8±2.9 K/decade for summer and 8.1±2.5 K/decade for winter.

A better understanding of how wave activity, neutral wind and other parameters affect the ion temperature would likely lead to a modification of Eq. (6). In the present study, Eq. (6) was used to estimate that the ion temperature at 110 km altitude is sinking by −1.00±0.59 K/year. At this altitude the electron and ion temperature are close and as expected a similar trend was also found for the electron temperature (not shown). However, since the trend in ion temperature was calculated after subtracting Eq. (6) from the measured data, a modification of this equation could possibly affect the observed trend. An improved understanding of the ion temperature variations seen in the upper panel of Fig. 7 is therefore necessary to derive a conclusive trend.

The ion and electron temperatures are derived from incoherent scatter spectrum fitting and a modeled ion-neutral collision frequency is used (e.g. (Lehtinen and Huuskonen, 1996)). MSIS neutral density is used for the modeled ion-neutral collision frequency and will therefore affect the results. Maeda et al. (2005) estimated that the ion temperature measured by the EISCAT UHF radar at 108–110 km altitude changes from 284 to 278 K when the collision frequency changes from 100% to 150%. The difference of 6 K is, however, small compared to the standard deviations in the lower part of Fig. 7.

Seasonal variations were found to have a significantly larger effect on the E-region ion temperature than the effect of solar activity. In contrast, solar activity plays the dominant role for variations of the ion temperature at F-region altitudes (Ogawa et al., 2014). In the F-region variations of ion temperature due to solar activity are approximately 400 K, while seasonal variations are approximately 200 K. The difference is because absorption of highly energetic solar radiation effectively works above 120 km altitude.

5. Summary

More than 30 years of data from the EISCAT Tromsø radar have been used to investigate the characteristics and trends of the E-region ion temperature and the peak height of the Hall conductivity. Variations depending on solar activity and solar zenith angle were determined, and these dependencies were subtracted from the data to search for long-term variations. Results from this study are summarized as follows:

- Seasonal variations of the Hall conductivity and its peak height are strong. The Hall conductivity at 110 km altitude was found to have seasonal variations of approximately $2 * 10^{-4}$ S/m, and the peak height have seasonal variations of approximately 6 km. Solar activity is also confirmed to affect the absolute value of the Hall conductivity. These variations are $\sim 8 * 10^{-5}$ S/m at 110 km altitude. On the other hand, the solar activity dependence of the peak height is weak. Variations in the peak height due to solar activity are only about 0.1 km.
- It is confirmed that also the ion temperature at 110 km altitude has clear seasonal variations of ~60 K. Variations due to solar activity are approximately 10 K, considerably lower than at higher altitudes where the solar activity dependence is usually stronger than the seasonal dependence.
- No significant long-term trend was found in the peak height of the Hall conductivity. A very weak descent of the peak height is seen (-0.18 ± 0.20 km/decade), but this descent is within the error bars of the averaged peak heights (see Fig. 4).
- A cooling trend of -1.00 ± 0.59 K/year at 110 km altitude was found in this study, although our attempt to estimate the ion temperature by using solar activity and solar zenith angle suggests that also other parameters might contribute significantly to the variations observed at 110 km altitude. A conclusive trend can be derived from the ion temperature if better understanding of the causes of ion temperature variations is achieved. Most previous studies report no significant cooling at this altitude (e.g. (Donaldson et al., 2010; Qian et al., 2011)).

Acknowledgements

EISCAT is an international association supported by research organisations in China (CRIRP), Finland (SA), Japan (NIPR and STEL), Norway (NFR), Sweden (VR), and the United Kingdom (NERC).

References

Beig, G., 2003. Review of mesospheric temperature trends. Rev. Geophys. 41, 4. http://dx.doi.org/10.1029/2010JA015346.

Donaldson, J.K., Wellman, T.J., Oliver, W.L., 2010. Long-term change in thermospheric temperature above saint santin. J. Geophys. Res. Space Phys. 115 (A11), A11305. http://dx.doi.org/10.1029/2010JA015346.

Golitsyn, G., Semenov, A., Shefov, N., Fishkova, L., Lysenko, E., Perov, S., 1996. Long-term temperature trends in the middle and upper atmosphere. Geophys. Res. Lett. 23 (14), 1741–1744. http://dx.doi.org/10.1029/96GL03720.

Hall, C.M., Holmen, S.E., Meek, C.E., Manson, A.H., Nozawa, S., 2016. Change in turbopause altitude at 52 and 70°N. Atmos. Chem. Phys. 16 (4), 2299–2308. http://dx.doi.org/10.5194/acp-16-2299-2016.

Hall, C.M., Rypdal, K., Rypdal, M., 2011. The e region at 69°N, 19°E: trends, significances, and detectability. J. Geophys. Res. Space Phys. 116 (A5), A05309. http://dx.doi.org/10.1029/2011JA016431.

Holmen, S.E., Hall, C.M., Tsutsumi, M., 2016. Neutral atmosphere temperaturetrends and variability at 90 km, 70°N, 19°E, 2003–2014. Atmos. Chem. Phys. 16 (12), 7853–7866. URL http://dx.doi.org/10.5194/acp-16-7853-2016.

Holt, J.M., Zhang, S.R., 2008. Long-term temperature trends in the ionosphere above Millstone Hill. Geophys. Res. Lett. 35 (5), L05813. http://dx.doi.org/10.1029/2007GL031148.

Ieda, A., Oyama, S., Vanhamäki, H., 2014. Approximate forms of daytime ionospheric conductance. J. Geophys. Res. Space Phys. 119, 10397–10415. http://dx.doi.org/10.1002/2014JA020665.

Laštovička, J., Solomon, S.C., Qian, L., 2012. Trends in the neutral and ionized upper atmosphere. Space Sci. Rev. 168 (1), 113–145. http://dx.doi.org/10.1007/s11214-011-9799-3.

Lehtinen, M.S., Huuskonen, A., 1996. General incoherent scatter analysis and GUISDAP. J. Atmos. Terr. Phys. 58 (1–4), 435–452. http://dx.doi.org/10.1016/0021-9169(95)00047-X.

Maeda, S., Nozawa, S., Ogawa, Y., Fujiwara, H., 2005. Comparative study of the high-latitude E region ion and neutral temperatures in the polar cap and the auroral region derived from the eiscat radar observations. J. Geophys. Res. Space Phys. 110 (A8), A08301. http://dx.doi.org/10.1029/2004JA010893.

Mielich, J., Bremer, J., 2013. Long-term trends in the ionospheric F2 region with different solar activity indices. Ann. Geophys. 31 (2), 291–303. http://dx.doi.org/10.5194/angeo-3-1 ((http://www.ann-geophys.net/31/291/2013/).

Moen, J., Brekke, A., 1993. The solar flux influence on quiet time conductances in the auroral ionosphere. Geophys. Res. Lett. 20 (10), 971–974. http://dx.doi.org/10.1029/92GL02109.

Ogawa, Y., Motoba, T., Buchert, S.C., Häggström, I., Nozawa, S., 2014. Upper atmosphere cooling over the past 33 years. Geophys. Res. Lett. 5629–5635. http://dx.doi.org/10.1002/2014GL060591.

Qian, L., Laštovička, J., Roble, R.G., Solomon, S.C., 2011. Progress in observations and simulations of global change in the upper atmosphere. J. Geophys. Res. Space Phys. (A2), 116. http://dx.doi.org/10.1029/2010JA016317.

Rishbeth, H., 1990. A greenhouse effect in the ionosphere? Planet. Space Sci. 38 (7), 945–948. http://dx.doi.org/10.1016/0032-0633(90)90061-T.

Roble, R., Dickinson, R., 1989. How will changes in carbon dioxide and methane modify the mean structure of the mesosphere and thermosphere? Geophys. Res. Lett. 16 (12), 1441–1444. http://dx.doi.org/10.1029/GL016i012p01441.

Sugino, M., Fujii, R., Nozawa, S., Buchert, S.C., Opgenoorth, H.J., Brekke, A., 2002. Relative contribution of ionospheric conductivity and electric field to ionospheric current. J. Geophys. Res. Space Phys. 107 (A10), 1330. http://dx.doi.org/10.1029/2001JA007545. SIA 20-1-SIA 20-15.

Zhang, S.-R., Holt, J.M., Erickson, P.J., Goncharenko, L.P., Nicolls, M.J., McCready, M., Kelly, J., 2016. Ionospheric ion temperature climate and upper atmospheric long-term cooling. J. Geophys. Res. Space Phys. A0 http://dx.doi.org/10.1002/2016JA022971 (2016J22971).

Zhang, S.-R., Holt, J.M., Kurdzo, J., 2011. Millstone Hill ISR observations of upper atmospheric long-term changes: height dependency. J. Geophys. Res. Space Phys. 116 (A2), A00H05. http://dx.doi.org/10.1029/2010JA016414.

Paper III:
High-latitude depletion regions and their dependence on geomagnetic activity

L. M. Bjoland, Y. Ogawa, and U. P. Løvhaug, submitted to *Journal of Geophysical Research Space Physics*, (2017).

High-latitude depletion regions and their dependence on geomagnetic activity

L. M. Bjoland[1], **Y. Ogawa**[2], **U. P. Løvhaug**[1]

[1]University of Tromsø - The Arctic university of Norway

[2]National Institute of Polar Research

Key Points:

- An early morning electron density depletion region is observed by the EISCAT Svalbard radar in the F-region polar cap ionosphere.
- As geomagnetic activity increases, the depletion region seems to expand in the polar cap.
- The IRI model does not reproduce the observed electron density depletion in the early morning.

Corresponding author: Lindis Merete Bjoland, lindis.m.bjoland@uit.no

Abstract

Ionospheric parameters are known to vary strongly during different conditions such as season, time of day, solar and geomagnetic activity. Data from the EISCAT radar systems in both Northern Scandinavia and Svalbard now cover several decades, and it is therefore suitable for studying variations of parameters in the high latitude ionosphere. In this work, the focus has been to investigate depletion regions at high-latitudes by presenting the main characteristics of the EISCAT electron density and ion temperature. Measurements by the EISCAT Svalbard Radar (ESR) indicates that such a depletion region is located in the polar cap early morning sector. This depletion region is co-located with an increase in ion temperature suggesting that ion frictional heating is important for its formation. As geomagnetic activity increases, the depletion region expands. This is likely due to the expansion of the polar cap and enhanced ion frictional heating during high geomagnetic activity. Comparisons with the International Reference Ionosphere (IRI) model indicate that the early morning depletion region is not included in the model. Also, the diurnal variations of the ion temperature, both in the polar cap and the auroral zone, are significantly stronger than predicted by the IRI model.

1 Introduction

The high-latitude F region ionosphere is a highly dynamic system where many different types of plasma density structures can form. Among these structures are regions where there is a depletion in the plasma density. In the present paper the term "depletion region" is used to describe large scale areas where the electron density is clearly less than in the surrounding areas. At high-latitudes, such depletion regions exist in several shapes and sizes and they can be caused by different types of formation mechanisms. The purpose of this study is to investigate the geomagnetic activity dependence of high-latitude electron density depletion regions in the F region.

Ionospheric troughs, polar holes and auroral cavities are examples of plasma depletion phenomena occurring in the high latitude F-region. Auroral cavities have a narrow, field-aligned shape and are located on the nightside, poleward of the auroral oval. Typically, the width of the cavities is less than 100 km and the density is 20-70% less than the surrounding background plasma [*Doe et al.*, 1993]. The formation of auroral cavities is connected to downward field aligned currents [e.g. *Doe et al.*, 1993; *Aikio et al.*, 2004]. Polar holes are large-scale depletion regions, and were first observed by *Brinton et al.*

[1978] in satellite data from the southern hemisphere. They can be found on the nightside between 70° and 80° latitude, co-located with the auroral cavities [e.g. *Benson and Grebowsky*, 2001]. During quiet geomagnetic conditions, polar holes form as a result of slow anti-sunward convection across the dark polar cap [*Brinton et al.*, 1978; *Sojka et al.*, 1981].

High-latitude troughs are located in the auroral zone and polar cap ionosphere. Their formation is mostly connected to frictional heating [*Rodger et al.*, 1992]. High ion temperatures lead to changes in the recombination rates and, as a consequence, an increase in the dissociative recombination process [e.g. *Schunk et al.*, 1976; *Rodger et al.*, 1992]. In addition, frictional heating also cause upflow of neutral nitrogen and oxygen into the F region. The enhanced concentrations of oxygen and nitrogen also contribute to an increased recombination [e.g. *Williams and Jain*, 1986; *Winser et al.*, 1986].

Troughs can also be formed in stagnation regions occurring in the convection pattern. If these stagnation regions are located in darkness, the plasma will be depleted due to recombination over a prolonged time period. At high latitudes, plasma usually follow a two-cell convection pattern with antisunward flow over the polar cap and return flow in the auroral zone [*Cowley*, 2000]. In the dusk sector the westward return flow is counteracted by corotation and a region with stagnated plasma convection is formed. As the plasma will stay in the stagnation region for a long time, troughs can form due to recombination at the nightside [e.g. *Knudsen*, 1974; *Spiro et al.*, 1978]. This formation mechanism is considered to be the most common for the nighttime mid-latitude trough [e.g. *Rodger et al.*, 1992; *Nilsson et al.*, 2005]. When the interplanetary magnetic field (IMF) is northward, and the IMF B_z component is larger than the IMF B_y component, a 3- or 4-cell structure will form instead of the 2-cell convection pattern [e.g. *Förster et al.*, 2008]. During winter, the additional convection cells will usually be located in darkness, and depletion regions, in this case called polar holes, will therefore form in these cells [*Sojka and Schunk*, 1987].

Since its discovery in the 1960s [*Muldrew*, 1965], several aspects of the mid-latitude trough has been investigated [*Moffett and Quegan*, 1983]. Mid-latitude troughs can be observed in any season and at both daytime and nighttime [e.g. *Voiculescu et al.*, 2006; *Lee et al.*, 2011]. It is usually located at highest latitudes around magnetic local noon, and moves to lower latitudes in the afternoon/evening. It reaches its lowest latitudinal position

around 2 magnetic local time (MLT), before it moves back towards higher latitudes [e.g. *Werner and Prölss*, 1997; *Voiculescu et al.*, 2006]. The location of the mid-latitude trough also strongly depends on geomagnetic activity, with the trough moving towards lower latitudes with increasing geomagnetic activity [e.g. *Köhnlein and Raitt*, 1977]. *Ishida et al.* [2014] investigated the solar activity dependence of the trough. During summer and equinox, they found that the depth of the trough increased with the F10.7 index. Furthermore, they found that during winter and equinox the occurrence rate of the trough is also affected by the level of solar activity.

Compared to the mid-latitude trough, less is known about troughs at higher latitudes. Some important investigations of high-latitude troughs do, however, exist, and early studies of high-latitude troughs were reviewed by *Rodger et al.* [1992]. In more recent years, *Ma et al.* [2000] investigated a case where a trough occurred close to the polar cap boundary during the recovery of a geomagnetic storm. *Zou et al.* [2013] studied the electrodynamics of an observed high-latitude trough, and *Voiculescu et al.* [2016] used the EISCAT radars to investigate the formation mechanism of the high-latitude post-midnight trough in summer.

In addition to regions of plasma depletion, there exist regions of plasma enhancement. Polar cap patches are an example of such regions of enhanced plasma density. They usually have a size between 100 and 1000 km, and are transported across the polar cap following the convection pattern [e.g. *Buchau et al.*, 1983; *Carlson et al.*, 2002; *Oksavik et al.*, 2006]. The region between patches may therefore be confused as a depletion region, whereas it in reality is the normal background ionosphere between two enhancements.

In the present study we aim to further expand the knowledge of high- latitude depletion regions. The long-term data base from the EISCAT radars in both Tromsø (geographic coordinates: 69.58° N, 19.23° E, geomagnetic coordinates: 66.73° N, 102.18°) and Longyearbyen (geographic coordinates: 78.15° N, 16.02° E, geomagnetic coordinates: 75.43° N, 110.68° E) were used to study high-latitude depletion regions in the polar cap and auroral zone ionosphere. The main part of our study focuses on investigating the seasonal variations and geomagnetic activity dependence of high-latitude depletion regions, and conducting a comparison between the polar cap and auroral zone ionosphere. In addition, we compare the results with the International Reference Ionosphere (IRI) 2016 model [*Bilitza et al.*, 2017].

2 Data and Method

The EISCAT Scientific Association operates three incoherent scatter radars in northern Scandinavia. Two of these radars, the UHF (930 MHz) and the VHF (224 MHz) system, are located near Tromsø, Norway and have been operational since the beginning of the 1980s. The EISCAT Svalbard radar (ESR), with a transmission frequency of 500 MHz, is located near Longyearbyen, Svalbard and started its operations in 1996. The radars provide range profiles of several primary plasma parameters. In this study we have investigated the electron density and ion temperature at F region altitudes between 200 and 500 km, using all available data from the radars started to operate until 2016.

An assumed ion mass is necessary to derive the ion temperature from the ion acoustic lines measured by incoherent scatter radars. In the transition region where the ion composition changes from molecular to atomic ions, the ion mass is highly variable and thus difficult to estimate accurately [e.g. *Blelly et al.*, 2010]. Ion temperature estimates from between 150 and 250 km altitude are therefore less precise, and as a consequence, ion temperature data were only used for altitudes above 250 km in this study. We use the accumulated EISCAT database from 1981, for the Tromsø UHF radar, and from 1996 for the ESR until 2016. The data were analysed using 5-minute integration intervals in the Grand Unified Incoherent Scatter Design and Analysis Package (GUISDAP) software [*Lehtinen and Huuskonen*, 1996]. Data were only used when the elevation angle of the radar beam was larger than 70°.

To remove erroneous data which sometimes occur, several filtering criteria were implemented on the analyzed data set. Data were only used when the electron density was between $10^{10}/m^3$ and $10^{12}/m^3$. Electron densities larger than $10^{12}/m^3$ are usually caused by special events, or by the radar beam hitting a hard target. Lower densities than $10^{10}/m^3$ are difficult to measure by the EISCAT radars. The power of the received signal depends on the electron density, and low electron densities will therefore cause a low signal-to-noise ratio. In addition, data were only used when the estimated ion temperature was less than 2000 K. Above 300 km altitude data were also removed when the electron density was lower than $3 \times 10^{10}/m^3$. The altitude of the maximum electron density (hmF2) in the F-region varies with season, time of day and solar activity [e.g. *Vickers et al.*, 2014], but is normally located around 200-300 km altitude. Electron density profiles were removed when the electron density increased with altitude above 350 km during solar maximum

years (before 1984, 1988-1993, 1998-2003 and 2011-2015) or above 300 km altitude during solar minimum years. Furthermore, data were removed when the uncertainty in the electron density exceeded 50%.

Electron density and ion temperature data from EISCAT were compared with modeled data from the 2016 version of the IRI model. The IRI model is an empirical model based on data from ionosondes, satellites, rocket experiments and incoherent scatter radars. Although there exist ionosondes also at high latitudes, including a few in the polar cap region, the IRI model is known to perform best at mid-latitudes where the station coverage is highest [e.g. *Bilitza and Reinisch*, 2008]. The model was first established in the 1960s as a joint project between the Committee on Space Research (COSPAR) and the International Union of Radio Science (URSI), and is updated when new data are available. It provides monthly averages of primary plasma parameters in the altitude range 50 to 2000 km [e.g. *Bilitza et al.*, 2017]. Standard options of the IRI model were used to produce the modeled electron density and ion temperature profiles. Modeled profiles were generated for the location of the Tromsø and the Svalbard radars for days when EISCAT data exist for the particular radar site. For such days hourly IRI electron density and ion temperature profiles were generated in the altitude range 200-500 km with a step size of 20 km.

3 Results

Figure 1 shows the averaged electron density at altitudes between 200 and 480 km vs month of year for low, medium and high solar activity. Here, low solar activity is defined as conditions where the F10.7 index is less than 100 solar flux units (sfu), medium solar activity is when 100 sfu$\leq$F10.7$<$150 sfu and high solar activity is when F10.7$\geq$150 sfu. Both ESR (top row) and UHF (bottom row) electron densities are shown. Only data from about local noon (10-12 UT) and for low geomagnetic activity (Kp$\leq$3) were used to make this figure. Bins with no data are shown as white.

Seasonal variations in the electron density, as seen in figure 1, are mainly due to changes in the solar zenith angle and in the thermospheric composition [*Rishbeth*, 1998]. For low solar activity, the ESR data show annual variations with highest electron density during summer. This is due to the variation of the solar zenith angle, which results in the single maximum during summer [*Zhang et al.*, 2005]. For medium and high solar activity, the ESR data show semiannual variation in the electron density with the highest densi-

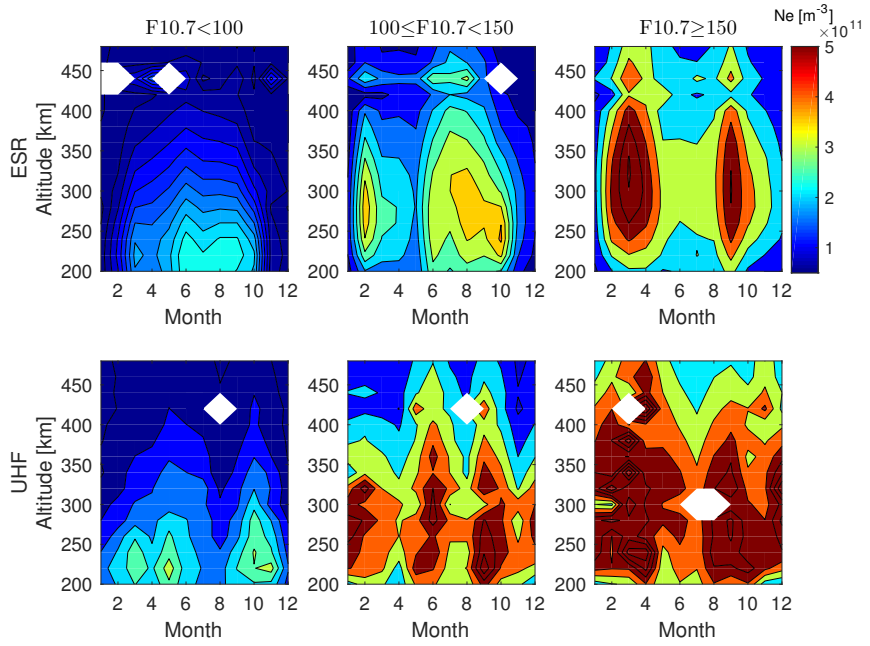

159 **Figure 1.** Contour plot of electron density from ESR (top row) and Tromsø UHF radar (bottom row) for
160 three different levels of solar activity. Altitudes from 200 km to 480 km are given along the y-axes, and month
161 of year on the x-axes.

175 ties close to equinox. *Qian et al.* [2016] found that the summer-to-winter gradient of the
176 O/N_2 ratio is large when the solar activity is high, and small for low solar activity. As a
177 result, the O/N_2 ratio will play a larger role in determining the electron density as the so-
178 lar activity increases, and this could explain why ESR observe semiannual variations in
179 the electron density for medium and high solar activity. Further south, the UHF data show
180 semiannual variations with peak densities close to equinox. As expected, the electron den-
181 sity increases with increasing solar activity. Also, for higher solar activity, the areas of
182 maximum electron density are seen to stretch over a larger altitude range. The UHF data
183 have three maximums during medium solar activity with peak densities near January, June
184 and September. This structure with three maximums could be due to the combined effects
185 of the summer-to-winter gradient of the O/N_2 ratio and the solar zenith angle. For high
186 solar activity, the UHF data show semiannual variations, but the peak density region is ex-

panded both in altitude and in number of months compared with the situation during low solar activity.

From figure 1 we notice that the electron density dependence on season and solar activity is strong. We therefore chose to divide the data into different categories according to season and solar activity when studying the geomagnetic dependence. Three different seasonal categories were used; summer consisting of the months May, June, July and August, winter which includes the months November, December, January and February and equinox which includes March, April, September and October. In addition, two different categories were used for the level of solar activity; low solar activity refers to data when the F10.7 index is less than 120 sfu and high solar activity refers to solar activity higher than 120 sfu. Approximately 30% of the ESR data and 40% of the UHF data belong to the high solar activity category.

Figure 2 shows the ESR electron density at altitudes between 250 and 420 km vs time of day (UT) for equinox. In order to investigate how geomagnetic activity affects depletion regions occurring in the high-latitude ionosphere, the data were separated into three different categories based on Kp-index. The three columns in figure 2 correspond to these three categories: low (Kp<2), medium (2≤Kp<4) and high (Kp≥4) geomagnetic activity. The top row shows electron densities during low solar activity (F10.7<120) and the bottom row shows the electron densities when the solar activity is high (F10.7≥120). In addition to the diurnal variations in figure 2, we observe that there is a clear depletion region located early morning at around 1-5 UT. As the difference between magnetic local time (MLT) and UT in Longyearbyen is approximately 3 hours, this corresponds to 4-8 MLT. Solar local time at Longyearbyen is UT+1. The depletion region is primarily observed in the high solar activity data. It can be seen for all altitudes between 250 and 420 km, however it is most pronounced at altitudes above 300 km. As the geomagnetic activity increases, the depletion region is observed for a longer time period. For low geomagnetic activity and high solar activity, the depletion region is observed from about 1-3 UT. For medium geomagnetic activity and high solar activity, this depletion region is best seen from 3-5 UT. When the geomagnetic activity is high, the observed depletion region expands and is visible from about 0-6 UT.

A line plot of the logarithm of electron density at 300 km altitude vs time of day is shown in figure 3. The same division of data according to geomagnetic and solar activ-

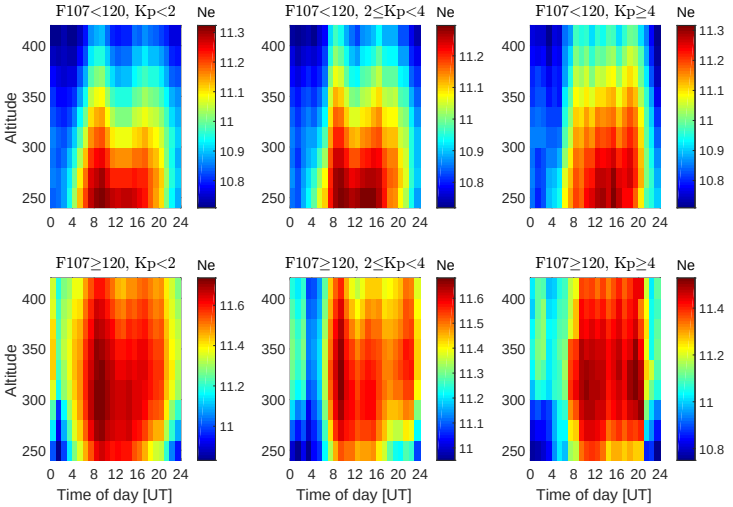

Figure 2. Color plots of ESR electron density during equinox at altitudes between 250 and 420 km vs time of day. The panels correspond to different combinations of solar and geomagnetic activity.

ity as used in figure 2 is also used in figures 3-8. The three columns correspond to low (panels **a**, **d** and **g**), moderate (panels **b**, **e** and **h**) and high (panels **c**, **f** and **i**) geomagnetic activity, while the rows show data from equinox (panels **a**, **b** and **c**), summer (panels **d**, **e** and **f**) and winter (panels **g**, **h** and **i**). To compare the results with the IRI model, the IRI modeled electron density is also plotted together with the ESR data. Each panel shows the ESR and IRI electron density during high and low solar activity. The green lines show the ESR electron density during low solar activity, and the purple lines the IRI electron density during low solar activity. Red and blue lines correspond to ESR and IRI electron densities during high solar activity, respectively. Due to lack of data, electron density is only shown for low solar activity during summer and winter when the geomagnetic activity is high. The error bars correspond to one standard deviation. Figure 3a shows that for high solar activity (red line), the depletion region in equinox is located around 1-2 UT when the geomagnetic activity is low. For moderate geomagnetic activity, the depletion region is expanded and slightly shifted towards later time of day. Figure 3b shows that in this case the depletion region can be observed from about 3-5 UT. For high geomagnetic activity the depletion region is further expanded and can be seen from 0-6 UT (figure 3c). An early morning depletion region can be observed for all seasons. During summer and

winter, this depletion region is best seen for high solar and moderate geomagnetic activity (figure 3e and 3h, red lines). It is observed from about 1-7 UT during summer, and from about 2-3 UT during winter. In addition, figure 3 shows that the IRI model is not able to reproduce the early-morning depletion region observed by the ESR. Similar as *Moen et al.* [2008], we also observe that the ESR electron density often show a double peak which is not reproduced by the IRI model. During winter and high solar activity, we observe the peaks at the same time of day as *Moen et al.* [2008]: A daytime peak located at about 9 UT and a nighttime peak at about 20 UT. The daytime peak can also be seen around 9 UT during equinox, but the nighttime peak occur a few hours earlier, around 16-17 UT, in our data set. During summer, the double peak structure is less clear than during the other seasons. *Moen et al.* [2008] explains the double peak structure by intake of high density plasma in the cusp region and transport across the polar cap to the nightside. *Pryse et al.* [1998] observed the dayside trough around noon at high latitudes using tomography and EISCAT UHF data. Their observed daytime trough coincides with the decrease in electron density between the two peaks in our ESR electron density. *Moen et al.* [2008] also compared their results with the IRI model. They concluded that the IRI model does not take the cross-polar transport into account and that this is the cause of the discrepancy between the IRI model and the ESR data.

Figure 4 shows the ion temperature for the same times, altitudes and conditions as in figure 3. An increase in the ion temperature is observed in the early morning in all panels except for figure 4**g**. This enhancement is observed for all categories of solar activity during equinox and summer. During winter it is seen for high and low solar activity during moderate geomagnetic activity (figure 4h and 4i), but not during low geomagnetic activity (figure 4g). In figure 4a, 4b, 4d and 4e, two peaks are observed in the ion temperature during low solar activity. This pattern with two peaks were also observed by *Yamazaki et al.* [2016] in the ESR ion temperature during low and moderate geomagnetic activity in 2007-2008. By comparing their results with the TIE-GCM model, they concluded that these diurnal variations in the ion temperature could be explained by ion frictional heating. *Ogawa et al.* [2011] observed a similar pattern with two peaks in the occurence frequency of ion upflow. When the geomagnetic activity is relatively low during low solar activity, the ESR will cross the auroral oval with high convection twice, in the pre-noon and post-noon, due to the contraction of the polar cap. This is likely the cause of the two peaks that are observed in the ion temperature.

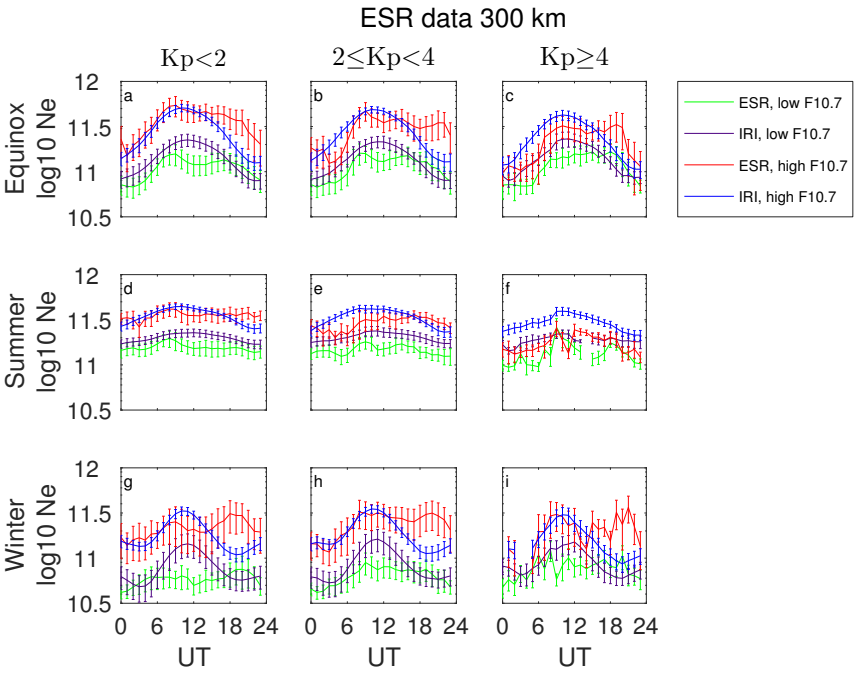

Figure 3. ESR and IRI electron density at 300 km altitude vs time of day. The columns correspond to different levels of geomagnetic activity, while the rows show different seasons. Each panel shows ESR and IRI electron density for both high and low solar activity.

Comparing figure 3 and 4, we observe that the ion temperature enhancement occurs at approximately the same time as the observed depletion regions. During equinox, the electron density depletion region is located at 1-2 UT during high solar activity and low geomagnetic activity, while an enhancement in the ion temperature occur at 1 UT. In figure 3b there is a depletion region from 3-5 UT when the solar activity is high, while there is an enhancement in the ion temperature in figure 4b from approximately 3-6 UT. During summer, an electron density depletion region was observed from about 1-7 UT for high solar activity and moderate geomagnetic activity in figure 3e. For the same conditions, there is an enhancement in the ion temperature from approximately 4-7 UT. During winter, high solar activity and moderate geomagnetic activity (figure 3**h**), electron density depletion was observed from 2-3 UT. There is an ion temperature enhancement in the morning during these conditions as well, but this enhancement last for a much longer time from about 3 to 11 UT. The electron density depletion and ion temperature enhancement

occurring at the same time, suggest that frictional heating is important for the formation of the observed depletion regions.

Furthermore, figure 4 shows that the IRI model is not able to reproduce the diurnal variations in the ion temperature, including the observed enhancement in the early morning. When the solar activity is high, the IRI model underestimates the ion temperature during most of the day for moderate and high geomagnetic activity. At low geomagnetic activity the IRI ion temperature is closer to the ESR ion temperature during equinox and summer (figures 4a and 4d), but overestimates the ion temperature during winter (figure 4g). When the solar activity and geomagnetic activity is low the IRI model overestimates the ion temperature for all season. For moderate geomagnetic activity the IRI and ESR ion temperature is closer, but the IRI model still clearly overestimates the ion temperature in the afternoon. During high geomagnetic activity (figure 4c), the IRI model underestimates the electron density before noon.

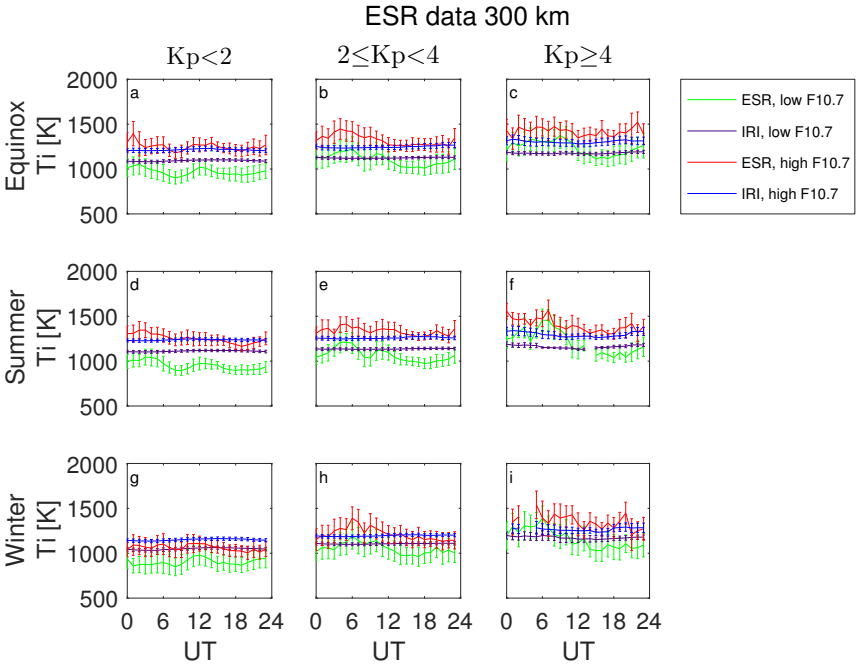

Figure 4. ESR ion temperature at 300 km altitude vs time of day for equinox, summer and winter. The columns correspond to different levels of geomagnetic activity, while the rows show different seasons. Each panel shows ESR and IRI ion temperature for both high and low solar activity.

Figures 5 and 6 show ESR northward and eastward convection velocities during equinox. In these figures **a**, **b** and **c** show velocities during low solar activity conditions, and **d**, **e** and **f** show velocities during high solar activity. **a** and **d** correspond to low, **b** and **e** to moderate and **c** and **f** to high geomagnetic activity. The convection velocities (in figures 5 and 6) can be derived from ESR data when the radar is operated in certain scanning modes. Figure 5 shows that when the geomagnetic activity is low or moderate (Kp<4) the velocity is predominantly northward during the time period when the early morning depletion region is observed. Around midnight the velocity is southward, but in the early morning the ESR is entering an area of northward velocities. For high Kp-index and high solar activity, shown in 5**f**, the radar is located in a region where the velocity is southward a few hours longer, and enters the region with northward velocity around 4 UT. Figures 6a and 6d show that during morning hours the velocity is eastward when the geomagnetic activity is low (Kp<2), while 6c and 6f show that the velocity is westward for high geomagnetic activity (Kp≥4). When the geomagnetic activity is low, ESR is entering a region of westward velocities around 7 UT. As the geomagnetic activity increases, the radar is entering this region earlier, and for high geomagnetic activity, the radar is entering this region around midnight. This implies that for high geomagnetic activity the ESR is located within the polar cap in the morning.

UHF electron density and ion temperature during equinox are plotted in figure 7 and figure 8, respectively. Here, the panels correspond to the same categories of solar and geomagnetic activity as in figures 5 and 6. Results from the UHF radar located in the auroral zone are compared with the ESR results from figure 3 and 4. In figure 7, diurnal variations of UHF (blue line) and ESR (red line) electron density at 300 km altitude during equinox are shown. Comparing the UHF and ESR electron density, it is apparent that the depletion region observed early morning in the ESR data is not seen in the UHF data. This depletion region therefore seems to be a polar cap phenomenon. Furthermore, the double peak structure seen in the ESR data, is not visible in the UHF data during low solar activity.

In figure 8, we compare the ESR ion temperature shown in figure 4 with the UHF ion temperature. The clear increase in ESR ion temperature observed early morning, is not present in the UHF data, where no increase, or only a very small increase when the geomagnetic activity is moderate/high, can be seen. However, it is clear that the UHF ion temperature is enhanced post-noon for both high and low solar activity. This enhancement

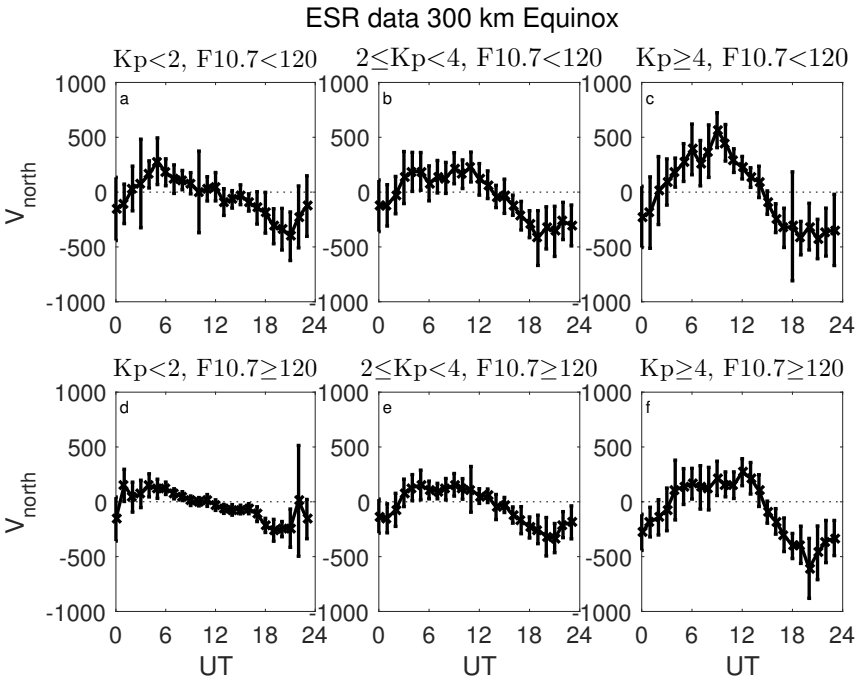

Figure 5. ESR northward velocities at 300 km altitude vs time of day for equinox.

is consistent with a post-noon heating region centered around 70° magnetic latitude observed by *Bjoland et al.* [2015].

It is shown in figure 4 that the IRI model overestimated the ion temperature at 300 km altitude at the ESR locations during low geomagnetic activity and underestimated it during high geomagnetic activity. Other altitudes between 250 and 450 km were also investigated. Figure 9 shows ESR and IRI ion temperature during equinox when the solar and geomagnetic activity is low, plotted for three different altitudes, 250 km, 350 km and 400 km. We notice that the overestimation by the model is stronger at higher altitudes.

4 Discussion

The comparison between the ESR and the UHF electron densities showed that the early morning depletion region could only be observed by the ESR radar. In order to investigate whether this is only a polar cap phenomenon, the convection velocities were plotted in figures 5 and 6. Figures 6c and 6f show that for high geomagnetic activity dur-

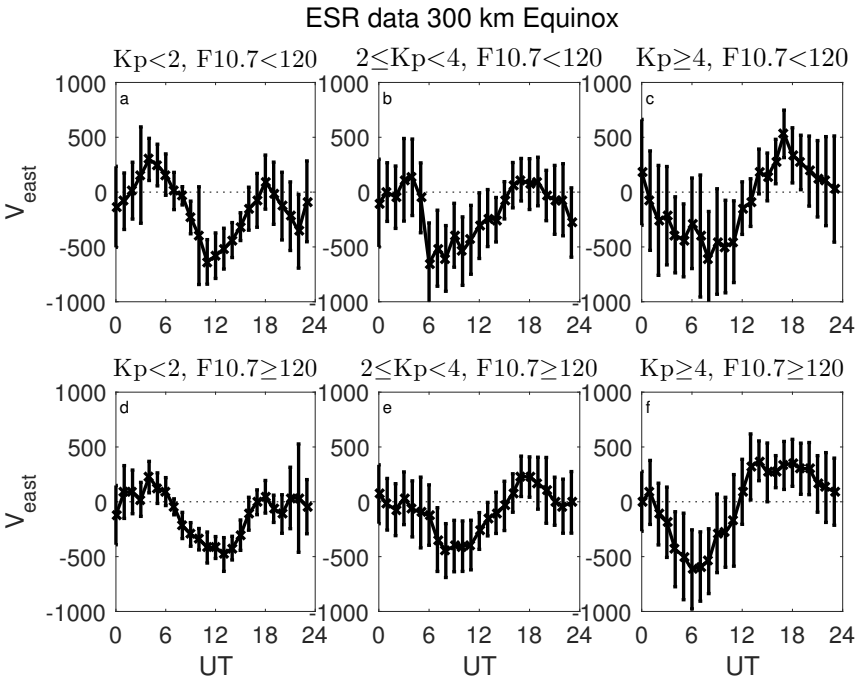

322 **Figure 6.** ESR eastward velocities at 300 km altitude vs time of day for equinox.

358 ing equinox, when the depletion region is observed by ESR for a longer time period, the
359 convection velocity is westward. *Aikio and Selkälä* [2009] used one-month of UHF radar
360 data from vernal equinox to study Joule heating rates, electric fields and conductances. As
361 plasma in the F-region moves according to the $\mathbf{E} \times \mathbf{B}$ drift, the ESR convection velocities
362 can be compared with the UHF northward and eastward electric field components. Figure
363 5 and 6 are mostly consistent with the electric field derived by *Aikio and Selkälä* [2009].
364 Also consistent with our results, they found that the morning maximum in the northward
365 electric field is shifted to a later time when the geomagnetic activity increases. It is there-
366 fore clear, from figures 6c and 6f, that the depletion region is located within the polar cap
367 when the geomagnetic activity is high.

368 In their review paper, *Rodger et al.* [1992] summarizes the locations and mechanisms
369 behind high-latitude troughs and other depletion regions. Two of the depletion regions
370 provided in their overview are located at about the same latitude and time of day as we
371 observe the early morning depletion region in the ESR data. When geophysical conditions

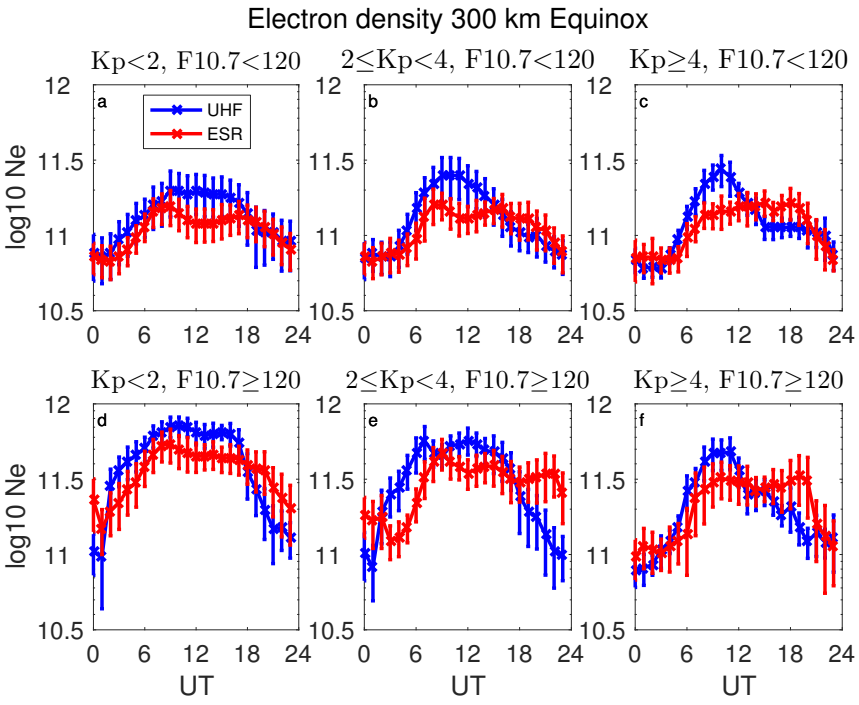

Figure 7. UHF electron density (blue line) and ESR electron density (red line) at 300 km altitude vs time of day for equinox. The panels correspond to different combinations of solar and geomagnetic activity.

are steady, a depletion region referred to as the polar hole can be observed shortly after midnight when the interplanetary magnetic field has a negative B_y component, and shortly before midnight when the B_y component is positive [*Sojka et al.*, 1991]. These polar holes can be caused by recombination when the convection across the dark polar cap is slow [e.g. *Brinton et al.*, 1978; *Crowley et al.*, 1993].

When the geophysical conditions are more active, polar cap patches can be observed drifting across the polar cap [e.g. *Oksavik et al.*, 2006]. Apparent depletion regions can therefore be observed in the morning and daytime between the patches. As shown in figure 4, the post-midnight depletion region observed in the ESR data is colocated with an increase in the ion temperature. This suggests that the observed depletion region is connected to frictional heating. Ion frictional heating is slightly more frequent during high solar activity [*Davies et al.*, 1999], and it is therefore reasonable that we observe the early

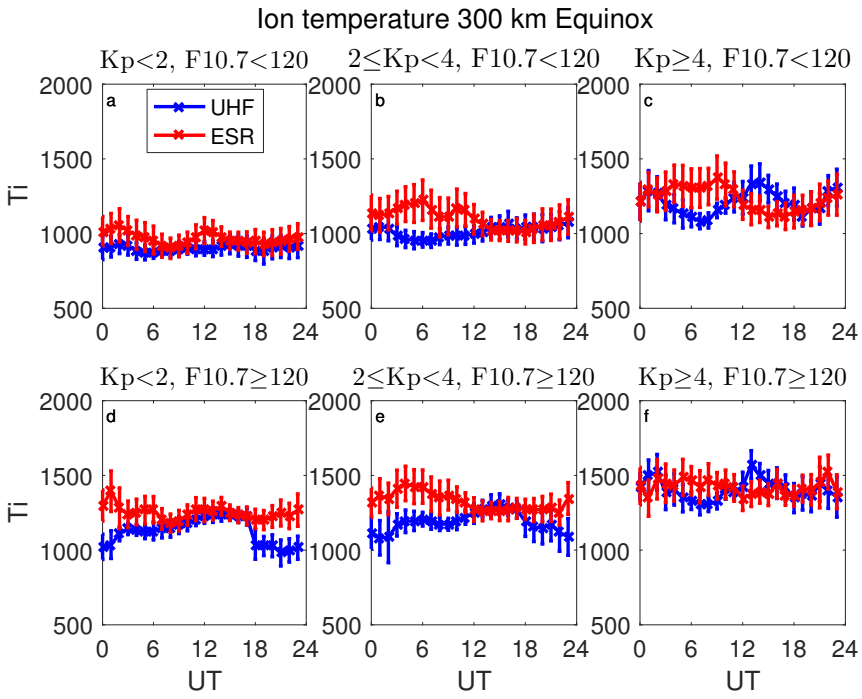

Figure 8. UHF ion temperature (blue line) and ESR ion temperature (red line) at 300 km altitude vs time of day for equinox. The panels correspond to different combinations of solar and geomagnetic activity.

morning depletion region in figure 3 clearest when the solar activity is high. As geomagnetic activity increases, the polar cap expands, and this likely explains why the early morning depletion region can be observed by ESR over a longer time period during high geomagnetic activity.

Comparing our results with the IRI model, we found that the IRI model did not reproduce the early morning depletion region. *Moen et al.* [2008] investigated the diurnal variability of the maximum density and peak height of the F-region using ESR data from February 2001 and October 2002. They also observed an early morning depletion region in the peak density, lasting from about 1-6 UT. Comparing the diurnal variations in the peak density with the IRI2001 model, *Moen et al.* [2008] concluded that cross-polar transport of plasma is not included in the IRI model. From their results, we note that the IRI model is not able to reproduce the early morning depletion region either, consistent with our results.

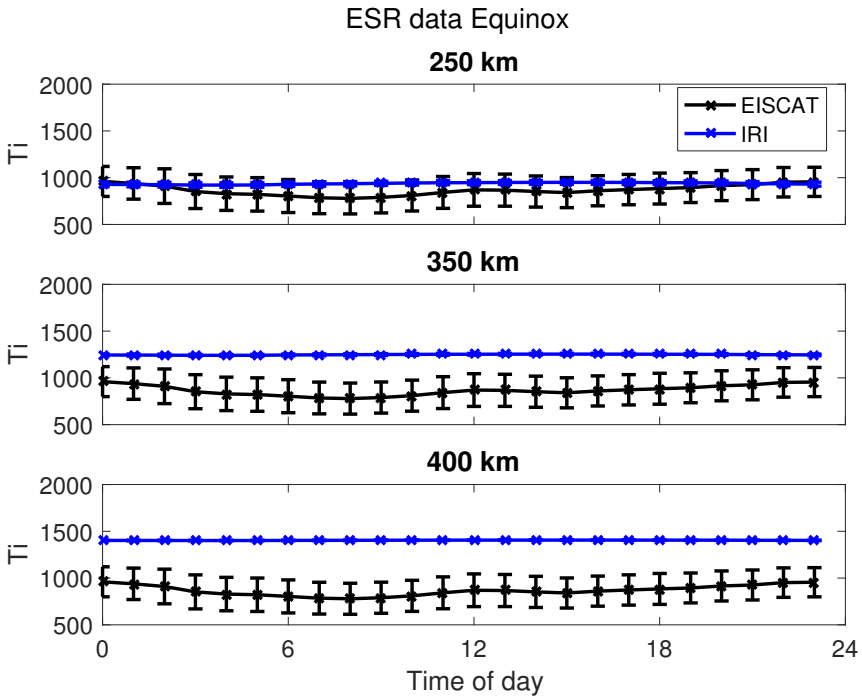

Figure 9. ESR ion temperature at three different altitudes (250 km, 350 km and 400 km) vs time of day. The data in this figure are from equinox, and during low solar and geomagnetic activity. IRI modeled ion temperatures are also shown and indicated by blue lines.

A comparison between the IRI model and ESR electron density was also conducted by *Bjoland et al.* [2016]. They found that the IRI model is underestimating the electron density, in particular at nighttime and during high solar activity. However, at altitudes around the peak height of the F-region electron density (hmF2), they found a fairly good agreement between the IRI model and the ESR data during most parts of the solar cycle. An overestimation of the electron density around the hmF2 was seen for some parts of the solar cycle, in particular during the years 2003-2004 as the solar cycle was approaching solar minimum. In figure 3, ESR electron densities at 300 km, which is usually close to where the hmF2 is located, were compared with the IRI model. In the evening, when the solar activity is high, an underestimation of the electron density is shown in all panels except for 3f. During other times of day, figure 3 shows that the IRI model in general is slightly overestimating the electron density at 300 km altitude. This can in particular be

seen clearly around noon for low solar activity. For the ESR electron density in figure 3, we observe that the IRI model does not seem to take into account the early morning depletion region and is therefore also overestimating the electron density there.

Fujiwara et al. [2012] compared ESR ion temperature measurements at 300 km altitude from solar minimum years 2007 and 2008 with the IRI2007 model. They plotted monthly averaged ESR and IRI ion temperatures, and found that the ESR data showed much larger diurnal and seasonal variations than the IRI model data. In general, they also find that the IRI model is overestimating the ion temperature at the ESR location. These results seems to be consistent with our results from figure 4. The green and purple lines in figure 4a, 4d and 4g show ESR and IRI ion temperature during low solar and geomagnetic conditions. These conditions are similar to the situation during the extended solar minimum in 2007 and 2008. Comparing our results during low solar and geomagnetic conditions with the results of *Fujiwara et al.* [2012], we find they are consistent. The IRI model fits the ESR ion temperature best post-midnight, but overestimates the ion temperature during most of the day.

5 Summary and conclusions

Measurements of electron density and ion temperature from the ESR and UHF radars have been used to study high-latitude depletion regions. The radars have by now been operational in several decades, and the accumulated database is therefore a useful tool to study seasonal, diurnal, geomagnetic and solar activity dependence of high-latitude electron density depletion regions. In this study the main purpose has been to investigate the geomagnetic dependence of high-latitude depletion regions, and to compare the auroral zone and polar cap ionosphere. In addition the results were compared with the latest IRI model. Our results can be summarized as follows:

- An electron density depletion region can be observed early morning in the ESR data. This depletion region is not observed by the UHF radar.
- This depletion region seems to expand when geomagnetic activity increases, most likely due to an expansion of the polar cap.
- Ion temperature measurements suggests that the formation of this observed depletion region is connected to ion frictional heating.

- The processes causing the depletion region observed in the ESR data does not seem to be included in the IRI model. Also, the IRI model have problems reproducing the diurnal variations in ion temperature both in the polar cap and in the auroral zone.

Acknowledgments

Fortran code for the IRI model can be downloaded from irimodel.org. Raw data from the EISCAT radars can be found on eiscat.se. EISCAT is an international association supported by research organisations in China (CRIRP), Finland (SA), Japan (NIPR and STEL), Norway (NFR), Sweden (VR), and the United Kingdom (NERC). This study was performed using database and internship program of National Institute of Polar Research (NIPR).

References

Aikio, A. T., and A. Selkälä (2009), Statistical properties of Joule heating rate, electric field and conductances at high latitudes, *Ann. Geophys.*, *27*(7), 2661–2673, doi:10.5194/angeo-27-2661-2009.

Aikio, A. T., K. Mursula, S. Buchert, F. Forme, O. Amm, G. Marklund, M. Dunlop, D. Fontaine, A. Vaivads, and A. Fazakerley (2004), Temporal evolution of two auroral arcs as measured by the Cluster satellite and coordinated ground-based instruments, *Ann. Geophys.*, *22*(12), 4089–4101, doi:10.5194/angeo-22-4089-2004.

Benson, R. F., and J. M. Grebowsky (2001), Extremely low ionospheric peak altitudes in the polar hole region, *Radio Sci.*, *36*(2), 277–285, doi:10.1029/1999RS002401.

Bilitza, D., and B. W. Reinisch (2008), International reference ionosphere 2007: Improvements and new parameters, *Adv. Space Res.*, *42*, 599–609, doi:10.1016/j.asr.2007.07.048.

Bilitza, D., D. Altadill, V. Truhlik, V. Shubin, I. Galkin, B. Reinisch, and X. Huang (2017), International reference ionosphere 2016: From ionospheric climate to real-time weather predictions, *Space Weather*, *15*(2), 418–429, doi:10.1002/2016SW001593.

Bjoland, L. M., X. Chen, Y. Jin, A. S. Reimer, Å. Skjæveland, M. R. Wessel, J. K. Burchill, L. B. N. Clausen, S. E. Haaland, and K. A. McWilliams (2015), Interplanetary magnetic field and solar cycle dependence of Northern Hemisphere F region joule heating, *J. Geophys. Res. Space Physics*, *120*(2), 1478–1487, doi:10.1002/2014JA020586.

Bjoland, L. M., V. Belyey, U. P. Løvhaug, and C. La Hoz (2016), An evaluation of International Reference Ionosphere electron density in the polar cap and cusp using EISCAT Svalbard radar measurements, *Ann. Geophys.*, *34*(9), 751–758, doi:10.5194/angeo-34-751-2016.

Blelly, P.-L., D. Alcaydé, and A. P. van Eyken (2010), A new analysis method for determining polar ionosphere and upper atmosphere characteristics from ESR data: Illustration with IPY period, *J. Geophys. Res.*, *115*, A09322, doi:10.1029/2009JA014876.

Brinton, H. C., J. M. Grebowsky, and L. H. Brace (1978), The high-latitude winter F region at 300 km: Thermal plasma observations from AE-C, *J. Geophys. Res.*, *83*(A10), 4767–4776, doi:10.1029/JA083iA10p04767.

Buchau, J., B. W. Reinisch, E. J. Weber, and J. G. Moore (1983), Structure and dynamics of the winter polar cap F region, *Radio Sci.*, *18*(6), 995–1010, doi:10.1029/RS018i006p00995.

Carlson, H. C., K. Oksavik, J. Moen, A. P. van Eyken, and P. Guio (2002), ESR mapping of polar-cap patches in the dark cusp, *Geophys. Res. Lett.*, *29*(10), 24–1–24–4, doi:10.1029/2001GL014087.

Cowley, S. W. H. (2000), Magnetosphere-ionosphere interactions: A tutorial review, in *Magnetospheric Current Systems*, edited by S.-I. Ohtani, R. Fujii, M. Hesse, and R. L. Lysak, pp. 91–106, American Geophysical Union, Washington, D. C., doi:10.1029/GM118p0091.

Crowley, G., H. C. Carlson, S. Basu, W. F. Denig, J. Buchau, and B. W. Reinisch (1993), The dynamic ionospheric polar hole, *Radio Sci.*, *28*(3), 401–413, doi:10.1029/92RS02878.

Davies, J. A., M. Lester, and I. W. McCrea (1999), Solar and seasonal dependence of ion frictional heating, *Ann. Geophys.*, *17*(5), 682–691, doi:10.1007/s00585-999-0682-4.

Doe, R. A., M. Mendillo, J. F. Vickrey, L. J. Zanetti, and R. W. Eastes (1993), Observations of nightside auroral cavities, *J. Geophys. Res. Space Physics*, *98*(A1), 293–310, doi:10.1029/92JA02004.

Förster, M., S. E. Haaland, G. Paschmann, J. M. Quinn, R. B. Torbert, H. Vaith, and C. A. Kletzing (2008), High-latitude plasma convection during Northward IMF as derived from in-situ magnetospheric Cluster EDI measurements, *Ann. Geophys.*, *26*(9), 2685–2700, doi:10.5194/angeo-26-2685-2008.

Fujiwara, H., S. Nozawa, S. Maeda, Y. Ogawa, Y. Miyoshi, H. Jin, H. Shinagawa, and K. Terada (2012), Polar cap ionosphere and thermosphere during the solar minimum period: EISCAT Svalbard radar observations and GCM simulations, *Earth Planets Space*, *64*(6), 459–465, doi:10.5047/eps.2011.05.023.

Ishida, T., Y. Ogawa, A. Kadokura, Y. Hiraki, and I. Häggström (2014), Seasonal variation and solar activity dependence of the quiet-time ionospheric trough, *J. Geophys. Res. Space Physics*, *119*(8), 6774–6783, doi:10.1002/2014JA019996.

Knudsen, W. C. (1974), Magnetospheric convection and the high-latitude F2 ionosphere, *J. Geophys. Res.*, *79*(7), 1046–1055, doi:10.1029/JA079i007p01046.

Köhnlein, W., and W. Raitt (1977), Position of the mid-latitude trough in the topside ionosphere as deduced from ESRO 4 observations, *Planet. Space Sci.*, *25*(6), 600 – 602, doi:10.1016/0032-0633(77)90069-1.

Lee, I. T., W. Wang, J. Y. Liu, C. Y. Chen, and C. H. Lin (2011), The ionospheric midlatitude trough observed by FORMOSAT-3/COSMIC during solar minimum, *J. Geophys. Res.*, *116*(A6), doi:10.1029/2010JA015544, A06311.

Lehtinen, M. S., and A. Huuskonen (1996), General incoherent scatter analysis and GUISDAP, *J. Atmos. Terr. Phys.*, *58*(1), 435–452, doi:10.1016/0021-9169(95)00047-X.

Ma, S. Y., P. Liu, and K. Schlegel (2000), EISCAT observation of a high-latitude ionization trough associated with a reversed westward plasma flow, *Geophys. Res. Lett.*, *27*(20), 3269–3272, doi:10.1029/2000GL000073.

Moen, J., X. C. Qiu, H. C. Carlson, R. Fujii, and I. W. McCrea (2008), On the diurnal variability in F2-region plasma density above the EISCAT Svalbard radar, *Ann. Geophys.*, *26*(8), 2427–2433, doi:10.5194/angeo-26-2427-2008.

Moffett, R., and S. Quegan (1983), The mid-latitude trough in the electron concentration of the ionospheric F-layer: a review of observations and modelling, *J. Atmos. Terr. Phys.*, *45*(5), 315 – 343, doi:10.1016/S0021-9169(83)80038-5.

Muldrew, D. B. (1965), F-layer ionization troughs deduced from Alouette data, *J. Geophys. Res.*, *70*(11), 2635–2650, doi:10.1029/JZ070i011p02635.

Nilsson, H., T. I. Sergienko, Y. Ebihara, and M. Yamauchi (2005), Quiet-time mid-latitude trough: influence of convection, field-aligned currents and proton precipitation, *Ann. Geophys.*, *23*(10), 3277–3288, doi:10.5194/angeo-23-3277-2005.

Ogawa, Y., S. C. Buchert, I. Häggström, M. T. Rietveld, R. Fujii, S. Nozawa, and H. Miyaoka (2011), On the statistical relation between ion upflow and naturally en-

hanced ion-acoustic lines observed with the EISCAT Svalbard radar, *J. Geophys. Res. Space Physics*, *116*(A3), n/a–n/a, doi:10.1029/2010JA015827, a03313.

Oksavik, K., J. M. Ruohoniemi, R. A. Greenwald, J. B. H. Baker, J. Moen, H. C. Carlson, T. K. Yeoman, and M. Lester (2006), Observations of isolated polar cap patches by the European Incoherent Scatter (EISCAT) Svalbard and Super Dual Auroral Radar Network (superDARN) Finland radars, *J. Geophys. Res. Space Physics*, *111*(A5), n/a–n/a, doi:10.1029/2005JA011400, a05310.

Pryse, S. E., L. Kersley, M. J. Williams, and I. K. Walker (1998), The spatial structure of the dayside ionospheric trough, *Ann. Geophys.*, *16*(10), 1169–1179, doi:10.1007/s00585-998-1169-4.

Qian, L., A. G. Burns, S. C. Solomon, W. Wang, and Y. Zhang (2016), Solar cycle variations of thermospheric composition at the solstices, *J. Geophys. Res. Space Physics*, *121*(4), 3740–3749, doi:10.1002/2016JA022390, 2016JA022390.

Rishbeth, H. (1998), How the thermospheric circulation affects the ionospheric f2-layer, *J. Atmos. Sol. Terr. Phys.*, *60*(14), 1385 – 1402, doi:10.1016/S1364-6826(98)00062-5.

Rodger, A., R. Moffett, and S. Quegan (1992), The role of ion drift in the formation of ionisation troughs in the mid- and high-latitude ionosphere—a review, *J. Atmos. Terr. Phys.*, *54*(1), 1 – 30, doi:10.1016/0021-9169(92)90082-V.

Schunk, R. W., P. M. Banks, and W. J. Raitt (1976), Effects of electric fields and other processes upon the nighttime high-latitude F layer, *J. Geophys. Res.*, *81*(19), 3271–3282, doi:10.1029/JA081i019p03271.

Sojka, J., R. Schunk, W. Hoegy, and J. Grebowsky (1991), Model and observation comparison of the universal time and imf by dependence of the ionospheric polar hole, *Adv. Space Res.*, *11*(10), 39 – 42, doi:10.1016/0273-1177(91)90318-E.

Sojka, J. J., and R. W. Schunk (1987), Theoretical study of the high-latitude ionosphere's response to multicell convection patterns, *J. Geophys. Res. Space Physics*, *92*(A8), 8733–8744, doi:10.1029/JA092iA08p08733.

Sojka, J. J., W. J. Raitt, and R. W. Schunk (1981), Plasma density features associated with strong convection in the winter high-latitude F region, *J. Geophys. Res. Space Physics*, *86*(A8), 6908–6916, doi:10.1029/JA086iA08p06908.

Spiro, R. W., R. A. Heelis, and W. B. Hanson (1978), Ion convection and the formation of the mid-latitude F region ionization trough, *J. Geophys. Res.*, *83*(A9), 4255–4264, doi:10.1029/JA083iA09p04255.

Vickers, H., M. J. Kosch, E. Sutton, L. Bjoland, Y. Ogawa, and C. La Hoz (2014), A solar cycle of upper thermosphere density observations from the EISCAT Svalbard radar, *J. Geophys. Res. Space Physics*, *119*(8), 6833–6845, doi:10.1002/2014JA019885.

Voiculescu, M., I. Virtanen, and T. Nygrén (2006), The F-region trough: seasonal morphology and relation to interplanetary magnetic field, *Ann. Geophys.*, *24*(1), 173–185, doi:10.5194/angeo-24-173-2006.

Voiculescu, M., T. Nygrén, A. T. Aikio, H. Vanhamäki, and V. Pierrard (2016), Postmidnight ionospheric troughs in summer at high latitudes, *J. Geophys. Res. Space Physics*, *121*(12), 12,171–12,185, doi:10.1002/2016JA023360.

Werner, S., and G. Prölss (1997), The position of the ionospheric trough as a function of local time and magnetic activity, *Adv. Space Res.*, *20*(9), 1717 – 1722, doi:10.1016/S0273-1177(97)00578-4.

Williams, P., and A. Jain (1986), Observations of the high latitude trough using EISCAT, *J. Atmos. Terr. Phys.*, *48*(5), 423 – 434, doi:10.1016/0021-9169(86)90119-4.

Winser, K., G. Jones, and P. Williams (1986), A quantitative study of the high latitude ionospheric trough using EISCAT's common programmes, *J. Atmos. Terr. Phys.*, *48*(9), 893 – 904, doi:10.1016/0021-9169(86)90064-4.

Yamazaki, Y., M. Kosch, Y. Ogawa, and D. Themens (2016), High-latitude ion temperature climatology during the International Polar Year 2007âĂŞ2008, *J. Space Weather Space Clim.*, *6*, A35, doi:10.1051/swsc/2016029.

Zhang, S.-R., J. M. Holt, A. P. van Eyken, M. McCready, C. Amory-Mazaudier, S. Fukao, and M. Sulzer (2005), Ionospheric local model and climatology from long-term databases of multiple incoherent scatter radars, *Geophys. Res. Lett.*, *32*(20), n/a–n/a, doi:10.1029/2005GL023603, l20102.

Zou, S., M. B. Moldwin, M. J. Nicolls, A. J. Ridley, A. J. Coster, E. Yizengaw, L. R. Lyons, and E. F. Donovan (2013), Electrodynamics of the high-latitude trough: Its relationship with convection flows and field-aligned currents, *J. Geophys. Res. Space Physics*, *118*(5), 2565–2572, doi:10.1002/jgra.50120.

Bibliography

Appleton, E. V., The Existence of more than one Ionised Layer in the Upper Atmosphere, *Nature*, *120*, 330, doi:10.1038/120330a0, 1927.

Appleton, E. V., and M. A. F. Barnett, Local Reflection of Wireless Waves from the Upper Atmosphere, *Nature*, *115*, 333–334, doi:10.1038/115333a0, 1925.

Appleton, E. V., R. Naismith, and L. J. Ingram, British radio observations during the Second International Polar Year 1932-33, *Philos. T. Roy. Soc. A*, *236*(764), 191–259, doi:10.1098/rsta.1937.0002, 1937.

Arrhenius, S., On the Influence of Carbonic Acid in the Air upon the Temperature of the Ground, *Philos. Mag. J. Sci.*, *41*, 237–276, 1896.

Baumjohann, W., and R. A. Treumann, *Basic Space Plasma Physics*, Imperial College Press, 1996.

Bilitza, D., and B. Reinisch, Representation of the auroral and polar ionosphere in the International Reference Ionosphere (IRI), *Adv. Space Res.*, *51*(4), 535, doi:10.1016/j.asr.2012.12.006, 2013.

Bilitza, D., and B. W. Reinisch, International reference ionosphere 2007: Improvements and new parameters, *Adv. Space Res.*, *42*, 599–609, doi:10.1016/j.asr.2007.07.048, 2008.

Bilitza, D., L.-A. McKinnell, B. Reinisch, and T. Fuller-Rowell, The international reference ionosphere today and in the future, *J. Geodesy*, *85*(12), 909–920, doi:10.1007/s00190-010-0427-x, 2011.

Bilitza, D., D. Altadill, Y. Zhang, C. Mertens, V. Truhlik, P. Richards, L.-A. McKinnell, and B. Reinisch, The International Reference Ionosphere 2012 – a model of international collaboration, *J. Space Weather Space Clim.*, *4*, A07, doi:10.1051/swsc/2014004, 2014.

Bilitza, D., D. Altadill, V. Truhlik, V. Shubin, I. Galkin, B. Reinisch, and X. Huang, International Reference Ionosphere 2016: From ionospheric climate to real-time weather predictions, *Space Weather*, *15*(2), 418–429, doi:10.1002/2016SW001593, 2017.

Bjoland, L., Y. Ogawa, C. Hall, M. Rietveld, U. Løvhaug, C. L. Hoz, and H. Miyaoka, Long-term variations and trends in the polar E-region, *J. Atmos. Sol. Terr. Phys.*, *163*, 85 – 90, doi:10.1016/j.jastp.2017.02.007, 2017a.

Bjoland, L., Y. Ogawa, and U. Løvhaug, High-latitude depletion regions and their dependence on geomagnetic activity, submitted to *J. Geophys. Res. Space Physics*, 2017b.

Bjoland, L. M., V. Belyey, U. P. Løvhaug, and C. La Hoz, An evaluation of International Reference Ionosphere electron density in the polar cap and cusp using EISCAT Svalbard radar measurements, *Ann. Geophys.*, *34*(9), 751–758, doi:10.5194/angeo-34-751-2016, 2016.

Bjørnå, N., Lecture notes in AGF-304 radar diagnostics of space plasma, 2005.

Bowles, K. L., Observation of Vertical-Incidence Scatter from the Ionosphere at 41 Mc/sec, *Phys. Rev. Lett.*, *1*, 454–455, doi:10.1103/PhysRevLett.1.454, 1958.

Breit, G., and M. A. Tuve, A Radio Method of Estimating the Height of the Conducting Layer, *Nature*, *116*, 357, doi:10.1038/116357a0, 1925.

Brekke, A., *Physics of the Upper Polar Atmosphere*, Springer-Verlag Berlin Heidelberg, 2013.

Bremer, J., Ionospheric trends in mid-latitudes as a possible indicator of the atmospheric greenhouse effect, *J. Atmos. Terr. Phys.*, *54*(11), 1505 – 1511, doi:http://dx.doi.org/10.1016/0021-9169(92)90157-G, 1992.

Bremer, J., Trends in the ionospheric E and F regions over Europe, *Ann. Geophys.*, *16*(8), 986–996, doi:10.1007/s00585-998-0986-9, 1998.

Chapman, S., The absorption and dissociative or ionizing effect of monochromatic radiation in an atmosphere on a rotating earth, *P. Phys. Soc.*, *43*, 26–45, doi:10.1088/0959-5309/43/1/305, 1931.

Cnossen, I., and A. D. Richmond, Modelling the effects of changes in the Earth's magnetic field from 1957 to 1997 on the ionospheric hmF2 and foF2 parameters, *J. Atmos. Sol. Terr. Phys.*, *70*(11), 1512 – 1524, doi:http://dx.doi.org/10.1016/j.jastp.2008.05.003, 2008.

Collis, P., and I. Häggström, Plasma convection and auroral precipitation processes associated with the main ionospheric trough at high latitudes, *J. Atmos. Terr. Phys.*, *50*(4), 389 – 404, doi:http://dx.doi.org/10.1016/0021-9169(88)90024-4, 1988.

Crowley, G., et al., Transformation of high-latitude ionospheric F region patches into blobs during the March 21, 1990, storm, *J. Geophys. Res. Space Physics*, *105*(A3), 5215–5230, doi:10.1029/1999JA900357, 2000.

Donaldson, J. K., T. J. Wellman, and W. L. Oliver, Long-term change in thermospheric temperature above Saint Santin, *J. Geophys. Res. Space Physics*, *115*(A11), doi:10.1029/2010JA015346, a11305, 2010.

Dungey, J. W., Interplanetary Magnetic Field and the Auroral Zones, *Phys. Rev. Lett.*, *6*, 47–48, doi:10.1103/PhysRevLett.6.47, 1961.

Farley, D., and T. Hagfors, Lecture notes.

Foster, J. C., et al., Multiradar observations of the polar tongue of ionization, *J. Geophys. Res. Space Physics*, *110*(A9), A09S31, doi:10.1029/2004JA010928, 2005.

Giraud, A., and M. Petit, *Ionospheric Techniques and Phenomena*, Springer Netherlands, 1978.

Glassmeier, K.-H., and B. T. Tsurutani, Carl Friedrich Gauss - General Theory of Terrestrial Magnetism - a revised translation of the German text, *Hist. of Geo-Space Sci.*, *5*(1), 11–62, doi:10.5194/hgss-5-11-2014, 2014.

Gordon, W., Incoherent Scattering of Radio Waves by Free Electrons with Applications to Space Exploration by Radar, *Proc. IRE*, *46*(11), 1824 – 1829, doi:10.1109/JRPROC.1958.286852, 1958.

Hall, C. M., and P. S. Cannon, Indication of shrinking atmosphere above Tromsø (69°N, 19°E), *Atmos. Sci. Lett.*, *2*(1-4), 18–24, doi:10.1006/asle.2001.0034, 2001.

Hall, C. M., K. Rypdal, and M. Rypdal, The E region at 69°N, 19°E: Trends, significances, and detectability, *J. Geophys. Res. Space Physics*, *116*(A5), doi:10.1029/2011JA016431, A05309, 2011.

Hall, C. M., S. E. Holmen, C. E. Meek, A. H. Manson, and S. Nozawa, Change in turbopause altitude at 52 and 70°N, *Atmos. Chem. Phys.*, *16*(4), 2299–2308, doi:10.5194/acp-16-2299-2016, 2016.

Heelis, R. A., The polar ionosphere, *Rev. Geophys.*, *20*(3), 567–576, doi:10.1029/RG020i003p00567, 1982.

Holmen, S. E., M. E. Dyrland, and F. Sigernes, Long-term trends and the effect of solar cycle variations on mesospheric winter temperatures over Longyearbyen, Svalbard (78°N), *J. Geophys. Res. Atmospheres*, *119*(11), 6596–6608, doi:10.1002/2013JD021195, 2014.

Holmen, S. E., C. M. Hall, and M. Tsutsumi, Neutral atmosphere temperature trends and variability at 90 km, 70°N, 19°E, 2003–2014, *Atmos. Chem. Phys.*, *16*(12), 7853–7866, doi:10.5194/acp-16-7853-2016, 2016.

Horvath, I., and E. Essex, The southern-hemisphere mid-latitude day-time and night-time trough at low-sunspot numbers, *J. Atmos. Sol. Terr. Phys.*, *65*(8), 917 – 940, doi:http://dx.doi.org/10.1016/S1364-6826(03)00113-5, 2003.

Hunsucker, R. D., and J. K. Hargreaves, *The High-Latitude Ionosphere and its Effects on Radio Propagation*, Cambridge University Press, 2002.

Iijima, T., and T. A. Potemra, Large-scale characteristics of field-aligned currents associated with substorms, *J. Geophys. Res. Space Physics*, *83*(A2), 599–615, doi:10.1029/JA083iA02p00599, 1978.

IPCC, *Climate Change 2007: The Physical Science Basis. Contribution of Working Group I to the Fourth Assessment Report of the Intergovernmental Panel on Climate Change (IPCC)*, 996 pp., Cambridge University Press, Cambridge, United Kingdom and New York, NY, USA, 2007.

Ishida, T., Y. Ogawa, A. Kadokura, Y. Hiraki, and I. Häggström, Seasonal variation and solar activity dependence of the quiet-time ionospheric trough, *J. Geophys. Res. Space Physics*, *119*(8), 6774–6783, doi:10.1002/2014JA019996, 2014.

Jarvis, M. J., B. Jenkins, and G. A. Rodgers, Southern hemisphere observations of a long-term decrease in F region altitude and thermospheric wind providing possible evidence for global thermospheric cooling, *J. Geophys. Res. Space Physics*, *103*(A9), 20,775–20,787, doi:10.1029/98JA01629, 1998.

Jin, H., Y. Miyoshi, H. Fujiwara, H. Shinagawa, K. Terada, N. Terada, M. Ishii, Y. Otsuka, and A. Saito, Vertical connection from the tropospheric activities to the ionospheric longitudinal structure simulated by a new Earth's whole atmosphere-ionosphere coupled model, *J. Geophys. Res. Space Physics*, *116*(A1), doi:10.1029/2010JA015925, A01316, 2011.

Keating, G. M., R. H. Tolson, and M. S. Bradford, Evidence of long term global decline in the Earth's thermospheric densities apparently related to anthropogenic effects, *Geophys. Res. Lett.*, *27*(10), 1523–1526, doi:10.1029/2000GL003771, 2000.

Kelley, M. C., *The Earth's Ionosphere Plasma Physics and Electrodynamics*, second ed., Academic Press, 2009.

Knudsen, W. C., Magnetospheric convection and the high-latitude F2 ionosphere, *J. Geophys. Res.*, *79*(7), 1046–1055, doi:10.1029/JA079i007p01046, 1974.

Laštovička, J., On the role of solar and geomagnetic activity in long-term trends in the atmosphere–ionosphere system, *J. Atmos. Sol. Terr. Phys.*, *67*(1), 83 – 92, doi:10.1016/j.jastp.2004.07.019, Solar Activity Forcing of the Middle Atmosphere, 2005.

Laštovička, J., R. A. Akmaev, G. Beig, J. Bremer, and J. T. Emmert, Global change in the upper atmosphere, *Science*, *314*(5803), 1253–1254, doi:10.1126/science.1135134, 2006.

Laštovička, J., S. C. Solomon, and L. Qian, Trends in the neutral and ionized upper atmosphere, *Space Sci. Rev.*, *168*(1), 113–145, doi:10.1007/s11214-011-9799-3, 2012.

Lee, I. T., W. Wang, J. Y. Liu, C. Y. Chen, and C. H. Lin, The ionospheric midlatitude trough observed by FORMOSAT-3/COSMIC during solar minimum, *J. Geophys. Res.*, *116*(A6), doi:10.1029/2010JA015544, A06311, 2011.

Lehtinen, M. S., and A. Huuskonen, General incoherent scatter analysis and GUISDAP, *J. Atmos. Terr. Phys.*, *58*(1-4), 435–452, doi:10.1016/0021-9169(95)00047-X, 1996.

Liu, J., T. Nakamura, L. Liu, W. Wang, N. Balan, T. Nishiyama, M. R. Hairston, and E. G. Thomas, Formation of polar ionospheric tongue of ionization during minor geomagnetic disturbed conditions, *J. Geophys. Res. Space Physics*, *120*(8), 6860–6873, doi:10.1002/2015JA021393, 2015JA021393, 2015.

Lockwood, M., and H. C. Carlson, Production of polar cap electron density patches by transient magnetopause reconnection, *Geophys. Res. Lett.*, *19*(17), 1731–1734, doi:10.1029/92GL01993, 1992.

Maltseva, O., N. Mozhaeva, and T. Nikitenko, Comparison of model and experimental ionospheric parameters at high latitudes, *Adv. Space Res.*, *51*(4), 599 – 609, doi:http://dx.doi.org/10.1016/j.asr.2012.04.009, 2013.

Manabe, S., and R. T. Wetherald, Thermal Equilibrium of the Atmosphere with a Given Distribution of Relative Humidity, *J. Atmos. Sci.*, *24*(3), 241–259, doi:10.1175/1520-0469(1967)024<0241:TEOTAW>2.0.CO;2, 1967.

Manabe, S., and R. T. Wetherald, The Effects of Doubling the CO2 Concentration on the climate of a General Circulation Model, *J. Atmos. Sci.*, *32*(1), 3–15, doi:10.1175/1520-0469(1975)032<0003:TEODTC>2.0.CO;2, 1975.

McKinnell, L., and M. Friedrich, Results from a new auroral lower ionosphere model, *Adv. Space Res.*, *37*(5), 1045 – 1050, doi:http://dx.doi.org/10.1016/j.asr.2004.11.008, 2006.

McKinnell, L.-A., and M. Friedrich, A neural network-based ionospheric model for the auroral zone, *J. Atmos. Sol. Terr. Phys.*, *69*(12), 1459 – 1470, doi:http://dx.doi.org/10.1016/j.jastp.2007.05.00, 2007.

Mertens, C. J., X. Xu, D. Bilitza, M. G. Mlynczak, and J. M. Russell, Empirical STORM-E model: I. Theoretical and observational basis, *Adv. Space Res.*, *51*(4), 554 – 574, doi:http://dx.doi.org/10.1016/j.asr.2012.09.009, 2013a.

Mertens, C. J., X. Xu, D. Bilitza, M. G. Mlynczak, and J. M. Russell, Empirical STORM-E model: II. Geomagnetic corrections to nighttime ionospheric E-region electron densities, *Adv. Space Res.*, *51*(4), 575 – 598, doi:http://dx.doi.org/10.1016/j.asr.2012.09.014, 2013b.

Moffett, R., and S. Quegan, The mid-latitude trough in the electron concentration of the ionospheric F-layer: a review of observations and modelling, *J. Atmos. Terr. Phys.*, *45*(5), 315 – 343, doi:10.1016/S0021-9169(83)80038-5, 1983.

Muldrew, D. B., F-layer ionization troughs deduced from Alouette data, *J. Geophys. Res.*, *70*(11), 2635–2650, doi:10.1029/JZ070i011p02635, 1965.

Nygrén, T., *Introduction to Incoherent Scatter Measurements*, Invers Oy, 1996.

Ogawa, Y., T. Motoba, S. C. Buchert, I. Häggström, and S. Nozawa, Upper atmosphere cooling over the past 33 years, *Geophys. Res. Lett.*, *41*(15), 5629–5635, doi:10.1002/2014GL060591, 2014.

Oksavik, K., J. M. Ruohoniemi, R. A. Greenwald, J. B. H. Baker, J. Moen, H. C. Carlson, T. K. Yeoman, and M. Lester, Observations of isolated polar cap patches by the European Incoherent Scatter (EISCAT) Svalbard and Super Dual Auroral Radar Network (SuperDARN) Finland radars, *J. Geophys. Res. Space Physics*, *111*(A5), A05310, doi:10.1029/2005JA011400, 2006.

Oliver, W. L., S.-R. Zhang, and L. P. Goncharenko, Is thermospheric global cooling caused by gravity waves?, *J. Geophys. Res. Space Physics*, *118*(6), 3898–3908, doi:10.1002/jgra.50370, 2013.

Oyeyemi, E., A. Adewale, A. Adeloye, and A. Akala, Comparison between IRI-2001 predictions and observed measurements of hmF2 over three high latitude stations during different solar activity periods, *J. Atmos. Terr. Phys.*, *72*(9–10), 676–684, doi:http://dx.doi.org/10.1016/j.jastp.2010.03.009, 2010.

Plass, G. N., The Carbon Dioxide Theory of Climatic Change, *Tellus*, *8*(2), 140–154, doi:10.1111/j.2153-3490.1956.tb01206.x, 1956.

Prölss, G. W., *Physics of the Earth's Space Environment: An Introduction*, Springer Berlin Heidelberg, 2004.

Qian, L., S. C. Solomon, and T. J. Kane, Seasonal variation of thermospheric density and composition, *J. Geophys. Res. Space Physics*, *114*(A1), doi:10.1029/2008JA013643, A01312, 2009.

Reiff, P. H., and J. L. Burch, IMF By-dependent plasma flow and Birkeland currents in the dayside magnetosphere: 2. A global model for northward and southward IMF, *J. Geophys. Res. Space Physics*, *90*(A2), 1595–1609, doi:10.1029/JA090iA02p01595, 1985.

Richmond, A. D., The ionosphere, in *The Solar Wind and the Earth*, edited by A.-I. Akasofu and Y. Kamide, pp. 123–140, Terra Scientific Publishing Company, 1987.

Rishbeth, H., A greenhouse effect in the ionosphere?, *Planet. Space Sci.*, *38*(7), 945 – 948, doi:http://dx.doi.org/10.1016/0032-0633(90)90061-T, 1990.

Rishbeth, H., and R. Roble, Cooling of the upper atmosphere by enhanced greenhouse gases — modelling of thermospheric and ionospheric effects, *Planet. Space Sci.*, *40*(7), 1011 – 1026, doi:10.1016/0032-0633(92)90141-A, 1992.

Roble, R., and R. Dickinson, How will changes in carbon dioxide and methane modify the mean structure of the mesosphere and thermosphere?, *Geophys. Res. Lett.*, *16*(12), 1441–1444, doi:10.1029/GL016i012p01441, 1989.

Rodger, A., R. Moffett, and S. Quegan, The role of ion drift in the formation of ionisation troughs in the mid- and high-latitude ionosphere—a review, *J. Atmos. Terr. Phys.*, *54*(1), 1 – 30, doi:10.1016/0021-9169(92)90082-V, 1992.

Roininen, L., M. Laine, and T. Ulich, Time-varying ionosonde trend: Case study of Sodankylä hmF2 data 1957–2014, *J. Geophys. Res. Space Physics*, *120*(8), 6851–6859, doi:10.1002/2015JA021176, 2015.

Sojka, J. J., M. D. Bowline, R. W. Schunk, D. T. Decker, C. E. Valladares, R. Sheehan, D. N. Anderson, and R. A. Heelis, Modeling polar cap F-region patches using time varying convection, *Geophys. Res. Lett.*, *20*(17), 1783–1786, doi:10.1029/93GL01347, 1993.

Spiro, R. W., R. A. Heelis, and W. B. Hanson, Ion convection and the formation of the mid-latitude F region ionization trough, *J. Geophys. Res.*, *83*(A9), 4255–4264, doi:10.1029/JA083iA09p04255, 1978.

Themens, D. R., and P. Jayachandran, Solar activity variability in the IRI at high latitudes: Comparisons with GPS total electron content, *J. Geophys. Res. Space Physics*, pp. 3793–3807, doi:10.1002/2016JA022664, 2016.

Tsunoda, R. T., High-latitude F region irregularities: A review and synthesis, *Rev. Geophys.*, *26*(4), 719–760, doi:10.1029/RG026i004p00719, 1988.

Turunen, E., P. T. Verronen, A. Seppälä, C. J. Rodger, M. A. Clilverd, J. Tamminen, C.-F. Enell, and T. Ulich, Impact of different energies of precipitating particles on NOx generation in the middle and upper atmosphere during geomagnetic storms, *J. Atmos. Sol. Terr. Phys.*, *71*(10), 1176 – 1189, doi:10.1016/j.jastp.2008.07.005, High Speed Solar Wind Streams and Geospace Interactions, 2009.

Ulich, T., and E. Turunen, Evidence for long-term cooling of the upper atmosphere in ionosonde data, *Geophys. Res. Lett.*, *24*(9), 1103–1106, doi: 10.1029/97GL50896, 1997.

Ulich, T., E. Turunen, A. Karinen, R. Kivi, and E. Kyrö, Atmospheric Trends Above Finland: I Mesosphere and Thermosphere, *Geophysica*, *35*, 59–69, 1999.

Upadhyay, H. O., and K. K. Mahajan, Atmospheric greenhouse effect and ionospheric trends, *Geophys. Res. Lett.*, *25*(17), 3375–3378, doi:10.1029/98GL02503, 1998.

Vickers, H., M. J. Kosch, E. Sutton, L. Bjoland, Y. Ogawa, and C. La Hoz, A solar cycle of upper thermosphere density observations from the EISCAT Svalbard Radar, *J. Geophys. Res. Space Physics*, *119*(8), 6833–6845, doi: 10.1002/2014JA019885, 2014.

Voiculescu, M., I. Virtanen, and T. Nygrén, The F-region trough: seasonal morphology and relation to interplanetary magnetic field, *Ann. Geophys.*, *24*(1), 173–185, doi:10.5194/angeo-24-173-2006, 2006.

Voiculescu, M., T. Nygrén, A. T. Aikio, H. Vanhamäki, and V. Pierrard, Postmidnight ionospheric troughs in summer at high latitudes, *J. Geophys. Res. Space Physics*, *121*(12), 12,171–12,185, doi:10.1002/2016JA023360, 2016.

Walker, I. K., J. Moen, L. Kersley, and D. A. Lorentzen, On the possible role of cusp/cleft precipitation in the formation of polar-cap patches, *Ann. Geophys.*, *17*(10), 1298–1305, doi:10.1007/s00585-999-1298-4, 1999.

Werner, S., and G. Prölss, The position of the ionospheric trough as a function of local time and magnetic activity, *Adv. Space Res.*, *20*(9), 1717 – 1722, doi:10.1016/S0273-1177(97)00578-4, 1997.

Winser, K., G. Jones, and P. Williams, A quantitative study of the high latitude ionospheric trough using EISCAT's common programmes, *J. Atmos. Terr. Phys.*, *48*(9), 893 – 904, doi:10.1016/0021-9169(86)90064-4, 1986.

Zhang, S.-R., and J. M. Holt, Long-term ionospheric cooling: Dependency on local time, season, solar activity, and geomagnetic activity, *J. Geophys. Res. Space Physics*, *118*(6), 3719–3730, doi:10.1002/jgra.50306, 2013.

Zhang, S.-R., J. M. Holt, and J. Kurdzo, Millstone Hill ISR observations of upper atmospheric long-term changes: Height dependency, *J. Geophys. Res. Space Physics*, *116*(A2), doi:10.1029/2010JA016414, A00H05, 2011.

Zhang, S.-R., J. M. Holt, P. J. Erickson, L. P. Goncharenko, M. J. Nicolls, M. McCready, and J. Kelly, Ionospheric ion temperature climate and upper atmospheric long-term cooling, *J. Geophys. Res. Space Physics*, *121*(9), 8951–8968, doi:10.1002/2016JA022971, 2016.

Zhang, Y., and L. Paxton, An empirical Kp-dependent global auroral model based on TIMED/GUVI FUV data, *J. Atmos. Sol. Terr. Phys.*, *70*(8), 1231 – 1242, doi:http://dx.doi.org/10.1016/j.jastp.2008.03.008, 2008.

Zou, S., M. B. Moldwin, M. J. Nicolls, A. J. Ridley, A. J. Coster, E. Yizengaw, L. R. Lyons, and E. F. Donovan, Electrodynamics of the high-latitude trough: Its relationship with convection flows and field-aligned currents, *J. Geophys. Res. Space Physics*, *118*(5), 2565–2572, doi:10.1002/jgra.50120, 2013.